Novel optical micromanipulation techniques and applications of violet diode lasers

Antonia E. Carruthers

Thesis for the degree of
Doctor of Philosophy

School of Physics and Astronomy,
University of St Andrews,
St Andrews, Fife
Scotland

June 2005

Abstract

In this thesis, optical micro-manipulation experiments are described using laser sources spanning the wavelength region 1064 nm to 410 nm. Optical guiding is studied at near-infrared wavelengths (780 nm) for comparison of a Gaussian and Bessel beam. The Bessel beam offers good transverse confinement. Extended guiding distances with the Bessel beam are shown with an enhancement factor of 3 over the Gaussian beam. Optical binding is observed in counter-propagating Gaussian beams using infrared light (at 780 nm and 1064 nm). In this geometry, the light-matter interaction induces particles to arrange themselves within a one-dimensional, regularly spaced particle array. A theoretical model is discussed to provide insight into the experimental data. Optical tweezing is performed using newly available short (violet) wavelength laser sources. The optical tweezers' trapping efficiencies were compared with a more traditional infrared source for tweezing. In addition, the violet lasers were used for biological spectroscopy, performing excitation of dyed chromosomes, and green fluorescent protein within cells. Finally, a violet microlensed diode laser at 413 nm is used with a microlensed diode at 662 nm for generating ultraviolet light in a non-linear sum frequency arrangement. This allows spectroscopy of atomic mercury at 254 nm to be performed.

Publications

1. A. E. Carruthers, S. A. Tatarkova, V. Garcés-Chávez, K. Dholakia, K. Volke-Sepulveda and S. Chaves-Cerda, "Optical guiding along Gaussian and Bessel light beams", Laser Processing of Advanced Materials and Laser Microtechnology, SPIE Proceedings **5121** 68 (2002)

2. S. A. Tatarkova, A. E. Carruthers, and K. Dholakia, "One dimensional optically bound arrays of microscopic particles", Phys. Rev. Lett. **89** 283901 (2002)

3. T. K. Lake, A. E. Carruthers, M. Taylor, L. Paterson, F. Gunn-Moore, J. W. Allen, W. Sibbett, and K. Dholakia, "Optical trapping and fluorescence excitation with violet diode lasers and extended cavity surface emitting lasers", Opt. Express **12** 670 (2004)

4. D. McGloin, A. E. Carruthers, K. Dholakia and E. M. Wright, "Optically bound microscopic particles in one dimension", Phys. Rev. E **69** 021403 (2004) Also featured in the Virtual Journal of Biological research

5. A. E. Carruthers, T. K. Lake, A. Shah, J. W. Allen, W. Sibbett, and K. Dholakia, "Microlensed red and violet diode lasers in an extended cavity geometry", Rev. Sci. Inst. **75** 3360 (2004)

6. L. Patterson, B. Agate, M. Comrie, R. Ferguson, T. K. Lake, J. E. Morris, A. E. Carruthers, C. T. A. Brown, W. Sibbett, P. E. Byrant, F. Gunn-Moore, A. C. Riches and K. Dholakia, "Photoporation and cell transfection using a violet diode laser", Opt. Express **13** 595 (2005)

7. A. E. Carruthers, T. K. Lake, A. Shah, J. W. Allen, W. Sibbett and K. Dholakia, "Single-scan spectroscopy of mercury at 253.7 nm by sum frequency mixing of violet and red microlensed diode lasers", Opt. Comm. *In press* (2005)

Declarations

I, Antonia E. Carruthers, hereby certify that this thesis, which is approximately 40 000 words in length, has been written by me, that it is the record of work carried out by me and that it has not been submitted in any previous application for a higher degree.

Date..18/10/05... Signature of candidate...

I was admitted as a research student in October 2001 and as a candidate for the degree of Ph.D. in October 2001; the higher study for which this is a record was carried out in the University of St Andrews between 2001 and 2005.

Date..18/10/05..... Signature of candidate.

I hereby certify that the candidate has fulfilled the conditions of the resolution and regulations appropriate for the degree of Ph. D. in the University of St Andrews and that the candidate is qualified to submit this thesis in application for that degree.

Date..18/10/05.... Signature of supervisor....

In submitting this thesis to the University of St Andrews I understand that I am giving permission for it to be made available for use in accordance with the regulations of the University Library for the time being in force, subject to any copyright vested in the work not being affected thereby. I also understand that the title and abstract will be published, and that a copy of the work may be made and supplied to any *bona fide* library or research worker.

Date..18/10/05..... Signature of candidate....

Acknowledgements

First and foremost, I would like to thank my supervisor, Professor Kishan Dholakia. His optimism, enthusiasm and support has been a great encouragement throughout my time working with him. Despite an often-demanding schedule, I very much appreciate him always making time for me. Thank you to past and present members of the group, collaborators and my office mates, who have helped me with areas of my work, and who have made working here both interesting and enjoyable. In particular, I would like to thank Tat, David, Daniel, Vene, Gabe, and Sveta for their advice and patience. To the many academics, postdocs and technicians in the department, who have helped me with aspects of my work, I would also like to extend my sincere thanks.

Thank you to my friends, in various parts of the world, including the members of the St Andrews Aikido club, for a welcome distraction to my thesis. I would especially like to thank Sensei Paul Hepple, Henry and Iain for their "settling" influence and unique outlook on life, despite the bulls tail being caught on the fence. Finally, I would like to thank my family for their help and support throughout.

Contents

Chapter 1

Introduction

Over the past three decades, since the conception of optical trapping in 1970, an abundance of novel optical manipulation techniques have emerged. These methods utilise the forces associated with momentum exchange between light and particles to manipulate matter. Optical tweezers use a highly focussed beam to induce an intensity gradient. This can localise a particle within a laser beam confining it in three dimensions. Through careful adjustment to the laser beam and optics used, the interplay of light forces on a particle can be altered. The first key area presented in this thesis explores this interplay of forces to create novel optical trapping techniques.

In the first experiment, scattered light is used to guide particles by "pushing" them along a beam of light. Earlier experiments in St Andrews have shown that the use of a Bessel beam can offer a "non-diffracting" core of light in which to efficiently guide particles. In this study, an optical guiding comparison is presented using a Gaussian beam and a Bessel beam. The use of a zeroth-order Bessel beam offers on-axis intensity, serving as a suitable comparison with the Gaussian beam. Particle velocities and guiding distances were investigated along the respective beams. A model is implemented to provide insight into beam propagation and particle localisation radially within the respective beams.

In the second study I consider the use of counter-propagating beams to confine particles. Two gently focussed Gaussian beams are horizontally co-aligned, such that their beam waists are separated along the propagation axis. Particles were observed to reside within the beam waists, forming a stable array where the individual particles lay spaced from one another. Introducing instability to the system caused a complete particle chain response leading to the particle arrays being considered optically bound. Modes of excitation were investigated in this arrangement and particle chains were examined by changing beam and particle parameters. A theoretical model is introduced to describe the particle arrays for a comparative study with experimental results.

The third project explores optical tweezing utilising newly-available violet laser sources. The use of shorter wavelengths allows a smaller focussed spot size to be obtained to allow the confinement of smaller particles. The trapping efficiencies of the violet laser sources were investigated. Comparison was made with infrared lasers, a common wavelength source for this optical technique. The violet lasers exhibited high trapping efficiencies to those presented elsewhere providing effective sub-micron optical trapping of particles. The use of violet diodes in this optical tweezing configuration allowed for their application to biological spectroscopy. As an excitation source, the violet lasers allowed observation of an inter-cellular protein transfected with green fluorescent protein. Optical tweezing was achieved and excitation of chromosomes was observed through the use of a fluorescent biological dye.

The second key area of this work is to perform spectroscopy on the atomic mercury 254 nm absorption line. The use of newly available violet and red microlensed diode lasers allows access to the ultraviolet region through non-linear sum frequency generation.

Initially, two microlensed diode lasers at 413 nm and 662 nm were characterised in a free running geometry. A microlens placed a few microns away from the diode output facet provides a circularised output beam. The weak feedback obtained from the microlens can be sufficient enough to allow the diode to operate in a single longitudinal mode. Additionally, a large continuous tuning range can be obtained through current tuning of the diode. In a separate experiment, the diodes were placed in an extended cavity. Several

diffraction gratings were alternately placed with the diodes in the Littrow configuration, to exploit the devices sensitivity to optical feedback. A narrowed laser linewidth was produced providing wavelength selectivity.

In the second study, diode lasers were combined in a non-linear crystal to generate ultraviolet light using a sum frequency mixing arrangement. Initially, light at 269 nm was generated using two diode laser sources in the violet and near-infrared. Violet and red microlensed diode lasers, were subsequently used to sum frequency generate light at 254 nm. The violet diode laser was coupled to an extended cavity for wavelength selectivity to access the required wavelength. Additionally, the red diode laser was used in a free-running geometry to exploit the long continuous tuning range. This allowed tuning over the wavelength region of interest. The generated ultraviolet light was maximised through the manipulation of beam parameters. A comparison was made between matching beam confocal parameters and beam waists inside the non-linear crystal.

The final experiment utilised the sum frequency generated ultraviolet light, at 254 nm, for spectroscopy on atomic mercury. A vapour cell at atmospheric pressure was initially used, allowing a broadened absorption peak to be obtained. In similar experiments conducted elsewhere, due to the width of the mercury line, several scans have been required to observe the entire feature. However, in this case, due to the long current tuning range of the red diode laser, the entire mercury absorption line was obtained in a single scan. In addition, a second vapour cell was used to observe the hyperfine structure of the absorption peak.

Chapter 2

Optical guiding using Gaussian and Bessel light beams

2.1 Introduction

A focused Gaussian beam propagating horizontally can move a particle, by "pushing" it along using radiation pressure. This is optical guiding [1]. Refraction of light through a particle can act to draw the particle to the most intense region of the beam. This radially confines the particle in two dimensions within the beam. The particle is then guided along the beam propagation direction, due to the remaining light force. Optical guiding controls the movement of particles, typically using a single beam, over a distance dictated by the beam properties. The crucial difference for optical guiding, compared with optical tweezing, is how tightly a beam is focussed. In optical tweezing, a high numerical aperture lens allows a tightly focussed beam to completely confine particles in three dimensions. Typically, a well-chosen optic determines whether a single beam will be used to guide or trap a particle.

The spatial profile of a light beam for the manipulation of particles plays an important role. If good lateral confinement is desired, in an optical guide of this kind, the high divergence obtained from tightly focussed Gaussian beams can limit their use. Therefore, interest has grown in the use of other possible light beams, to guide and trap particles

over extended distances. Bessel beams, display the unusual and important characteristic of being pseudo "non-diffracting". A Bessel beam propagates without beam divergence in the transverse intensity distribution. This beam attribute suggests that in optical guiding a Bessel beam rather than a Gaussian beam is a more appropriate choice [2]. This makes them excellent candidates for guiding applications. The guiding distance is potentially large compared with the Rayleigh range of a Gaussian beam, the range over which the beam cross-sectional area approximately doubles. Furthermore, the propagation-invariant nature of the Bessel beam could also permit other applications, such as laser range finding and atom guiding [3].

In this chapter particle guiding is studied in detail. Gaussian beam transportation of micron-sized objects is described as well as achieving extended guiding distances using a Bessel beam [2,3,4]. A theoretical and experimental study of optical guiding is presented, by establishing a detailed comparison between Gaussian and Bessel beams. In particular, a comparison is made between a zeroth-order Bessel beam and a fundamental Gaussian beam. Both guides are introduced in a horizontal beam geometry.

2.2 Optical tweezing

Ashkin's curiosity about the ability of light to transfer momentum to objects allowed the realisation of the optical manipulation of microscopic particles. In 1970, a horizontal optical guide was demonstrated using a Gaussian light beam [1]. This early experiment exploited the radiation pressure of light to accelerate particles along the optical guide. In this study, Ashkin established that a particle of higher refractive index than its surrounding medium would be confined to the high intensity region. Particles of lower refractive index were shown to be repelled from the beam centre, preferentially remaining in a region of low intensity.

In Ashkin's initial study [1], the horizontal optical guide was further developed through the use of two horizontal optical guides, co-linearly aligned. The beam waists of the guides were displaced along the propagation axis. The effect of such a counter-

propagating beam geometry was that particles could also be stably trapped between the two focussed beam waists. A subsequent experiment [5] showed a modified optical guide aligned in the vertical direction. In this orientation, the radiation pressure pushed the sphere upwards in stable balance with gravity. This geometry resulted in a particle being held in air within a single light beam. Ashkin's studies also led to the use of a single tightly focussed beam used to optically trap particles in three dimensions [6]. The term "optical tweezing" has been adopted exclusively for the use of light to trap objects in this latter geometry.

Optical tweezers are now extensively used and have become a valuable inter-disciplinary tool. The ability to three-dimensionally trap objects on the microscopic scale has had an enormous impact in physics, biology and chemistry. Huge progress has been made in many studies, for example aiding investigations into the unravelling of DNA [7], measuring mechanical forces of molecular systems [8,9,10] and allowing insight into cell properties [11]. The abilities to isolate and observe component cell parts, as well as the opportunity to measure their interactions, are essential to the understanding of biological and physical systems. For this reason, Ashkin's initial work has been continually adapted, spawning a wealth of optical techniques designed to guide, trap, rotate, stack and sort matter. Such optical techniques will be discussed later.

2.3 Radiation pressure of light

In 1917, Einstein introduced expressions for light travelling through a vacuum. According to this form, light has an associated energy ($h\nu$) and momentum ($h\nu/c$) [12]. This fundamental idea prompted Ashkin, in 1969, to consider the relationship as light interacted with a mirror [13]. Normally incident light on hitting the mirror, changes direction and is reflected directly back.

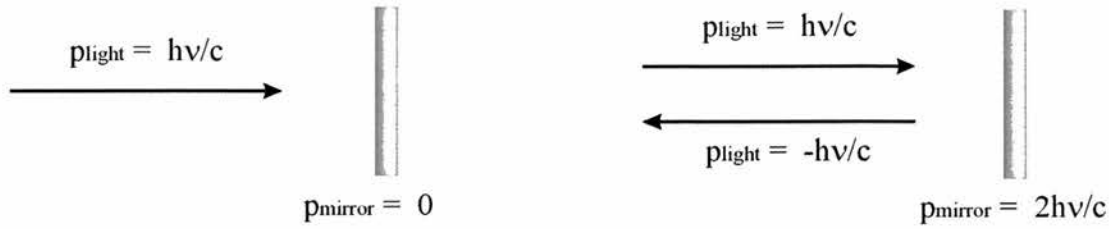

Figure 2.1. Light is shown incident on a mirror. Before the interaction, light has momentum (hν/c) and the mirror is at rest. After the collision, the light has changed direction and has transferred momentum to the mirror.

Momentum is transferred between the light and mirror as they interact. The change in momentum of the light, in this case, is twice that of the incident ray's momentum, as shown in figure 2.1. Due to conservation of momentum, this change in light momentum has necessarily been transferred to the mirror. Thus an optical radiation pressure arises.

In a similar manner, the radiation pressure of light can be used to influence the motion of small particles. The presence of particles within a light field can influence the direction of light and thus change its momentum. The rate of change in momentum, p, can be described by a force (equation 2.1);

$$F = \frac{dp}{dt} = \frac{mdv}{dt} \qquad [2.1]$$

where dv/dt is the rate of change of velocity, m the fixed particle mass, and v the particle velocity. This interaction between light and an object can be exploited to transfer momentum and influence an object's motion. This is the basis of optical tweezers.

2.4 Optical trapping

2.4.1 Mie, Rayleigh and intermediate regimes

The details of the forces involved in optical tweezing can be considered in terms which depend upon the particle radius size a, with respect to the wavelength λ. These can be categorised into three optical regimes. The case where the particle size is considerably greater than the wavelength, in the region of $a > 10\lambda$, is shown in figure 2.2(a). Such a

particle is said to exist in the Mie regime where the particle motion can be described in terms of geometrical ray optics [14].

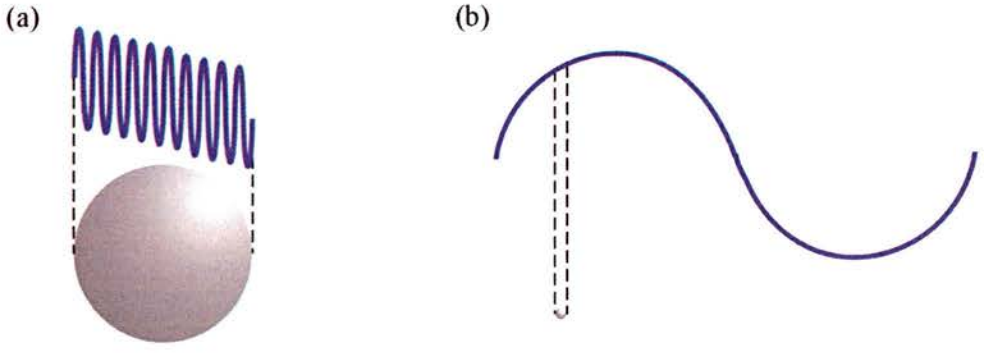

Figure 2.2. The (a) Mie regime where the particle is large compared to the wavelength and (b) Rayleigh regime where the particle is small compared to the wavelength, is shown.

Particles considerably smaller than the wavelength ($a < \lambda/20$) are considered to exist within the Rayleigh regime. Such a particle is shown in figure 2.2(b). Here, a Rayleigh approximation is not fully appropriate, as the electric field is not uniform over the particle. For particles of a size comparable to the wavelength of light, an intermediate regime exists. Optical trapping will now be discussed for each size regime.

2.4.2 Mie Regime ($a >> \lambda$)

The interaction of light with a transparent particle, in the Mie regime, can be discussed in terms of geometric ray optics, as in figure 2.3. Incident light is both refracted and reflected. Light refracting through the particle induces the so-called gradient force whilst reflected light from the particle surface creates what is commonly referred to as the scattering force.

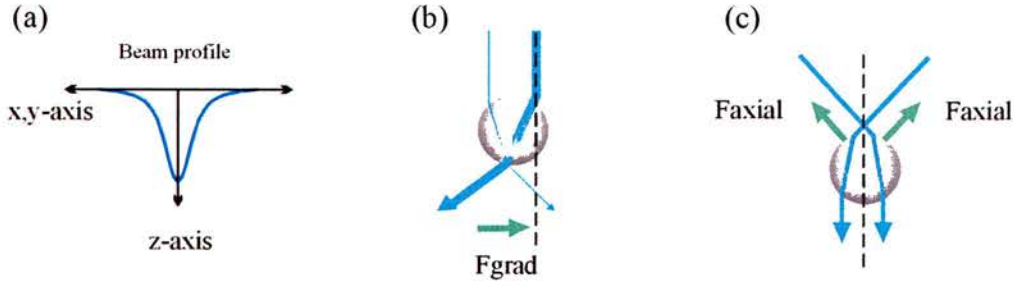

Figure 2.3. A tightly focussed Gaussian beam (a), is refracted through a sphere. The transverse gradient force (F_{grad}) (b), and axial gradient force (F_{axial}) (c), are shown confining the particle central to the region of maximum intensity. Light rays are shown in blue and force components in green.

Incident light is partially refracted through a particle causing a change in the direction and momentum of light. This interaction creates a transfer of momentum, resulting in an associated force. The force associated with a particular light ray acts to "push" the particle in the direction opposing the change in that ray's propagation. Higher intensity light rays refracted by the sphere yield a higher associated force than those possessing a lower intensity. This imbalance of forces over the sphere's surface, results in the particle moving in the direction of the net force, figure 2.3(b). An equilibrium of forces exists once the particle moves to a position central to the on-axis beam intensity, localising the sphere.

In addition, an axial gradient force arises in a tightly focussed beam. This acts to confine the particle to the z-axis focal region of the beam, figure 2.3(c). Off-axis rays interact with the sphere at an angle and are refracted. As in the case for a radially confined particle, transfer of momentum occurs on interaction between light and matter. In this case, a net force is created in the – z-direction. The particle moves in the direction of this unbalanced force towards a position of equilibrium. Forces balance when the axial gradient force forms equilibrium with the scattering force from the sphere, figure 2.4. The combined action of the transverse and axial gradient forces, confine the sphere in three dimensions. This creates optical tweezers.

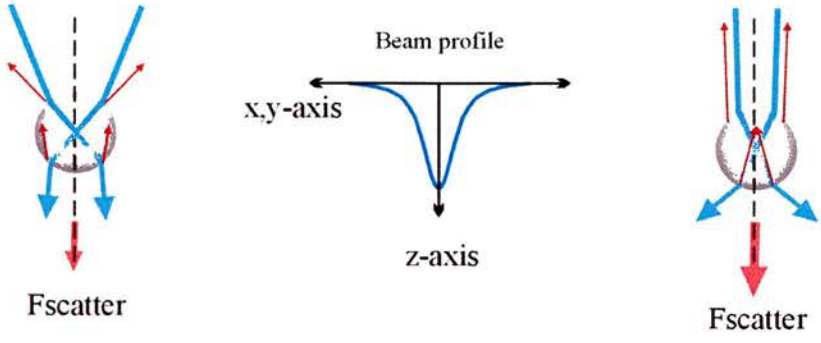

Figure 2.4. A particle, central to the tightly focussed (left) and gently focussed (right) Gaussian beam, experiences a scattering force in the z-direction. This force arises due to partial reflections from the incident light as it interacts with the surface of the sphere.

However, the use of a less tightly focussed beam can cause a change in the dominant force. As with a tightly focussed beam, the gradient force localises a particle radially to the region of highest intensity. Here, a less tightly focussed beam can be deemed parallel to the propagation axis in the focal region. Therefore, the large angles of incident light, contributing to the optical tweezer, are not present. The rays creating confinement in the z-direction are not as strong, inducing a much weaker gradient force. In this case, the scattering force dominates and the particle is "pushed" along the beam (figure 2.4). An equilibrium position in the z-direction between scattering and dipole forces cannot be found. This is optical guiding.

2.4.3 Gradient and scattering forces in the Mie regime

Light incident on the sphere produces a gradient force and a scattering force. In the Mie regime, for a tightly focussed beam, the gradient force dominates to create a three dimensional trap. For a gently focussed beam, the gradient force is reduced allowing the scattering force to prevail.

The axial (F_z) and radial (F_r) trapping forces incident on a particle are proportional to the power of the laser beam [14]. The energy contained within the incident laser beam can be written as $E = pc$, where the momentum of light is denoted p, and the speed of light in a vacuum c. In an ideal case, light interacting with a particle is entirely "absorbed" over an

interaction time interval of Δt. The magnitude of the momentum change can therefore, be written as $\Delta p = \Delta U/c$ where ΔU is the change in kinetic energy. The associated radiation pressure force, due to Newton's second law of motion, can also be written in terms of the change of momentum, as in equation 2.2.

$$F = \frac{\Delta p}{\Delta t} = \frac{\Delta U}{c}\frac{1}{\Delta t} = \frac{P}{c} \qquad [2.2]$$

Here P is the power of the incident beam. This equation reflects the case where the incident light is completely absorbed by the particle and the momentum transfer of the laser beam to the particle is successfully converted into a gradient force. However, as light experiences both refraction and reflection, on interaction with a transparent particle, this expression shown in equation 2.2 must be adapted. Therefore, the force a particle experiences from an incident laser beam can be described as equation 2.3 [15].

$$F_{(r,z)} = \frac{nQ_{(r,z)}P}{c} \qquad [2.3]$$

In this equation, n is the refractive index of the surrounding medium that the particles reside in. A trapping efficiency Q_i, a dimensionless parameter, is introduced to reflect the efficiency of the momentum transfer, in a given experimental configuration, from the laser beam to the gradient force. The ability of light to push a particle along the beam propagation axis can be described by the scattering force. A similar treatment to equation 2.3 can be used to describe the scattering force, by taking into account the total power scattered by the particle.

2.4.4 Rayleigh Regime ($a << \lambda$)

The Rayleigh regime encompasses particle sizes which are considered to be much smaller than the incident wavelength. For these particles, it can be helpful to consider them as polarisable dipoles residing in an oscillating electric field. Due to the small region of interaction, Rayleigh particles only "see" a limited region of the beam. Therefore, it can be assumed that the incident electric field is uniform over the scale of the particle. For this reason, Rayleigh particles cannot be dealt with in term of ray optics. In the Rayleigh

regime, the area over which light interacts with the dipole is considered, and not the electric field as a whole [16].

A dipole moment can be induced within a particle with an overall charge of zero, where no permanent dipole exists. The linearly polarised electric field E, can induce the dipole moment $\rho = \alpha E$, over the particle. Where, a polarisable particle has relative polarisability α, and a high particle refractive index relative to the surroundings is denoted a *positive* relative polarisability.

For a small oscillating dipole, its motion can be considered with respect to this incident oscillating field in which it resides. The induced dipole causes the particle to experience a net force dependent entirely upon the gradient in E, shown in equation 2.4 [16].

$$F = -\nabla U = (\rho \cdot \nabla)E = \alpha E \cdot \nabla E = \alpha \nabla E^2 \qquad [2.4]$$

This force can attract or repel the dipole from the region of highest intensity. In the case where the dipole oscillates at a higher frequency than that of the incident field, the particle will move towards the field. In the same manner, a dipole oscillating at a comparatively lower frequency will attract to regions of a lower intensity.

The force causing the particle to be confined is therefore dependent on the gradient force of the incident electric field, also known interchangeably as the dipole force inferred from equation 2.4. The particle is confined within the beam when the dipole force and scattering force reach equilibrium. The dipole force acts to draw the particle to the most central on-axis maximum and towards the beam waist. However, this force is weak for Rayleigh particles, and the scattering force plays a significant role in the interaction. The scattering force arises from the incident light on the sphere creating a "push" in the direction of beam propagation.

2.4.5 Dipole and scattering forces in the Rayleigh regime

In the Rayleigh regime, the dipole and scattering force find equilibrium to optically trap a particle. However, unlike the Mie regime where the gradient force dominates to confine

the particle, in the Rayleigh regime the scattering force dominates. Expressions for these forces can be found in the paraxial approximation using a focussed Gaussian beam [17]. This approximation considers light rays to be approximately parallel to the propagation axis where $\lambda << w_o$. However, these results remain valid approximations for a tightly focussed beam, due to the Rayleigh particle size with respect to the beam waist size.

The dipole force F_{dipole}, can be described by equation 2.5 [14,17].

$$F_{dipole}(r) = 2\pi n_h^2 \varepsilon_0 a^3 \left(\frac{m^2 - 1}{m^2 + 2} \right) \nabla \left| E^2(r) \right| \qquad [2.5]$$

Here, m, is the ratio between the refractive index of the particle n_p, and host medium n_h, and is denoted $m = n_p / n_h$. The permittivity of free space, also known as the dielectric constant, is indicated by ε_0, and the electric field component by $\vec{E}(\vec{r})$, a is the particle radius.

The scattering force originates from momentum changes of the light due to scattered light from the particle. The scattering force F_{scatt}, can be described by equation 2.6 [14,17].

$$F_{scatt}(r) = \hat{z} \frac{n_h}{c} \frac{128\pi^5 a^6}{3\lambda^4} \left(\frac{m^2 - 1}{m^2 + 2} \right)^2 I(\vec{r}) \qquad [2.6]$$

$I(r)$ is the intensity of the incident light, determined by the number of incident photons per time and area [14,17]. $\hat{z}$ is the unit vector along the z-axis. For optical tweezing in this regime, the scattering force must be considered. Due to equations 2.5 and 2.6 the dipole and scattering forces in relation to the particle size are shown as $F_{scatt} \propto a^6$ and $F_{dipole} \propto a^3$. Therefore, the significance of the scattering force is dependent on the size of the particle. For stable optical trapping to occur, the ratio of the dipole force with respect to the scattering force must exceed unity. Equations 2.5 and 2.6 are presented here for illustration of the force's dependency on particle size and wavelength. They are not used in this nor subsequent chapters for modelling or calculation.

2.4.6 Intermediate Regime ($a \approx \lambda$)

Particles of similar dimensions to the incident wavelength can be considered to reside in an intermediate regime. The calculations for this regime are, however, nontrivial. Due to the increase in particle size the Rayleigh approximation fails and an extension of the Mie approach is required [14]. Here, force is described by *F(r)*, equation 2.7.

$$F(r)=\frac{n_h}{c} I_0 \left[\vec{x} C_{pr,x}(r)+\vec{y} C_{pr,y}(r)+\vec{z} C_{pr,z}(r)\right] \qquad [2.7]$$

In this equation, the cross-sectional areas $C_{pr,i}$ are expressions to describe the incident light impinging on a spherical particle [18,19].The intensity is given by $I_0 = 2P/\pi w_0^2$ at a beam waist w_0, where the factor of 2 assumes reflection of light along the same path as the incident light.

So far, only the dipole and scattering forces have been considered. However, due to the wavelength region (near infrared and infrared) used here for optical guiding, other forces must be taken into consideration that can usually be ignored. In optical tweezing, the gradient force must dominate over all other forces to confine the particle. However, in optical guiding, the strong scattering force need not always dominate. In this case, the absorption of the laser light through the trapping medium can induce a strong heating force. This effect will now be discussed.

2.4.7 Drag, convection and diffusion

In optical tweezing and guiding, convective heating effects arise, created from the absorption of laser light in a medium. The gradient force in optical tweezing is usually large enough to dominate over this heating effect. However, in optical guiding the comparatively weak scattering force can conflict with convective forces. A toroidal roll can be produced, which if the dominant force, can prevent optical trapping. However, a convective force can also be useful, creating a continuous flow of particles in their suspending medium. The heating effects cause particles to rise, which subsequently fall under gravity to interact with the guiding beam. For some laser wavelengths, a significant

heating force on the medium can be induced, causing particles to be carried with the upward convection current. This is dependent on the absorption properties of the medium at the wavelength used, but is prevalent, even at modest power levels, for 1064 nm light passing through water.

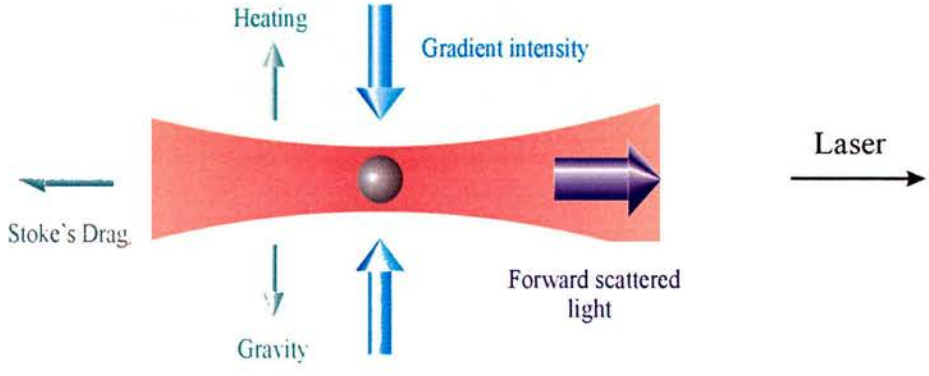

Figure 2.5. Forces acting on an optically guided sphere are shown. The gradient intensity confines the particle transverse to the beam and guiding occurs due to a scattering force.

Additionally, particles within a guiding beam can diffuse, due to Brownian motion. Molecules in the surrounding medium continuously collide, occasionally displacing the larger particles. This effect allows particles to diffuse within the beam, becoming much more pronounced for small particles. This motion can assist particles lying far from the beam focus to escape the guiding beam. Figure 2.5 illustrates the competing forces acting on a guided sphere. The Stoke's drag is a resistance to motion through the suspension medium. This will be discussed in chapter 4 in greater detail.

Both optical tweezers and optical guiding are examined in this work. However, initially, optical guiding is considered in this chapter. This will be done through the use of Gaussian and Bessel light beams, which will now be discussed.

2.5 Gaussian beam propagation

The Gaussian beam discussed so far consists of a single maximum, centred along the beam propagation direction, diverging at an angle (equation 2.8) away from beam waist w_0. The divergence angle θ can be described by;

$$\theta = \frac{\lambda}{\pi w_0} \qquad [2.8]$$

where λ is the wavelength of the laser. The Rayleigh range, z_R, of a Gaussian beam (equation 2.9) is a standard length by which beam divergence is measured. This is the distance wherein the cross-sectional area at beam waist doubles.

$$z_R = \frac{\pi w_0^2}{\lambda} \qquad [2.9]$$

This can be a very useful parameter for comparison with other beams. For a wavelength of 780 nm and a beam waist of 3.5 μm, the Rayleigh range of a Gaussian beam is 49 μm. This is a relatively short distance. However, through the use of other types of beams this can be improved upon. A Bessel beam can provide extended propagation distances. This beam will now be discussed.

2.6 Bessel light beams

2.6.1 The diffraction of light and the wave equation

The theory of diffraction describes a wavefront propagating in a given direction, which may change in amplitude, phase or polarisation, on hitting an obstruction. Light regions, not obstructed, bend around the obstacle and interfere together. This creates a diffraction pattern. Such a pattern can be observed in a Bessel light beam.

The Helmholtz scalar wave equation has fundamental solutions, such as the Gaussian and Bessel beam modes discussed in this chapter. Bessel beams arise as exact solutions of the Helmholtz equation, described by equation 2.10 [20].

$$\nabla^2 \underline{E} + k_0 n^2 \underline{E} = 0 \qquad [2.10]$$

Here the transverse electric field vector is $\underline{E} = \underline{E}_0 \exp[i\omega t - kr]$ and k_o is the wavevector in free space with refractive index n. In principle, Bessel beams appear "non-diffracting" in the same sense as a plane wave [4], although both obey the theory of diffraction. In practice, only approximations to an ideal Bessel beam can be achieved.

2.6.2 "Non-diffracting" beam profiles

Durnin, in 1987, illustrated a "non-diffracting" theoretical solution. A bright central maximum was shown, surrounded by an infinite number of rings. This propagation-invariant solution can be described by a zeroth-order Bessel function. The beam's electric field amplitude is shown in equation 2.11 [3].

$$E_z(r,\theta) = AJ_v(kr)\exp(jv\theta) \qquad [2.11]$$

Here J_v denotes the order of Bessel function equivalent to the beam used and r the beam radius. A is an arbitrary amplitude of the field of the beam. The resulting Bessel beam may be considered an interference pattern, shown in figures 2.6. The beam undergoes a phase shift, noticeable from the bright peak and dark trough regions, representing a beam phase change of π, across the beams intensity profile [21].

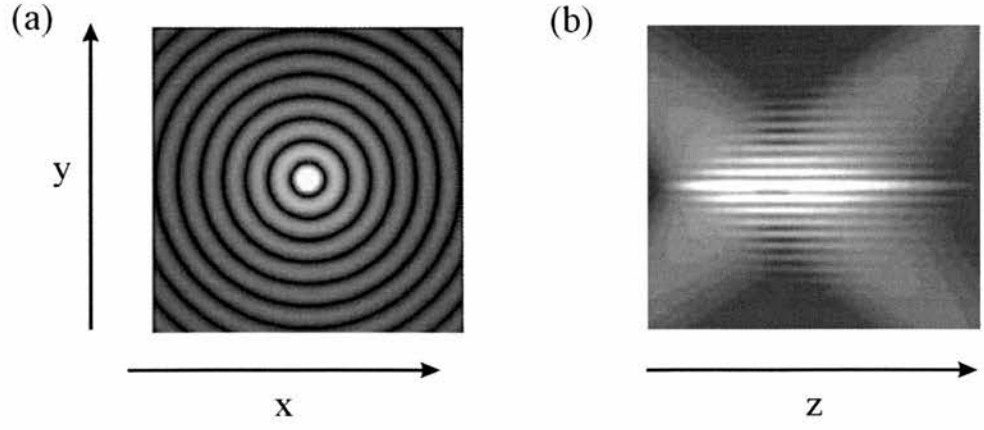

Figure 2.6. Simulated Bessel beam (a) profile transverse to beam propagation and (b) longitudinal profile, from an axicon on the left, along the beam propagation.

The theoretical "non-diffracting" central core has an infinite ring distribution surrounding it; each ring contains approximately the same total power, figure 2.6(a). For this reason, a

Bessel beam such as shown here, stores most of its total beam power in the outer rings. Ideally, this transverse cross-section beam intensity along the propagation axis z is identical in any plane. The complication of this theoretical model of a Bessel beam is that it can, of course, not be realised experimentally. An infinite number of rings, each with equal power, require an infinite power source to produce power for an infinite number of rings. The beam radius would also demand infinitely large optic apertures that would, in turn, result in a rather large laboratory. Therefore, an approximation to a Bessel beam is the best that can be realised in an optical system.

An approximation to a Bessel beam may be created experimentally by passing a beam through a conical lens (axicon). The resulting intensity distribution, shown in figure 2.6(b), is also relatively constant along the z-axis. The intensity in the central maximum is supplied by light coming in at an angle, passing through the outer rings and thus will act to help reform the central intensity profile. Similarly, a poor ring quality will therefore generally yield a poor central maximum. As an experimental rule of thumb, the more rings present in the entire beam, the longer the propagation length can be maintained.

The central maximum is rod-like and does not expand as the beam propagates. A Bessel beam thus appears "non-diffracting", whilst still obeying diffraction theory. A Gaussian whose power is solely contained within a central beam can be a useful comparison to this diffractionless central spot.

The superposition of waves refracted by a conical lens creates a diffraction pattern whose wave vectors, naturally, lie on a cone shape, centred along the propagation axis. Bessel beams are therefore created by a superposition of travelling conical wavefronts, whose radial components point in different directions. The magnitude of these radial components of the beam can be described as $k_r = |k| \sin\theta$, where θ denotes the angle at which the conical wavefronts expand, forming a ring in the far-field. This ring is the spatial Fourier transform of a Bessel beam, in which all wavevectors lie.
The construction of a Bessel beam's interference pattern requires the phase front of the overall beam to remain constant throughout the propagation length. Therefore, Bessel

beams can be described as a transverse standing wave, travelling longitudinally [2]. For this reason, experimental Bessel beams are not true propagating beams in the usual sense. The interference pattern formation of an approximate Bessel beam allows it to possess self-reconstruction properties. Different sections of the beam act to form different regions of the interfering light [22]. Again, it is the outer rings of a Bessel beam that, on hitting an obstacle, permit the central beam to be reconstructed.

2.7 Generation of Bessel beams

There are several methods by which a Bessel beam can be constructed. Initially, the Bessel beam formation shown by Durnin [4] produced a non-diffracting beam created through illuminating an annular slit in the back focal plane of a lens (figure 2.7). This annular slit allows a ring of light to be produced, which subsequently Fourier transforms into a Bessel beam using the lens. This method is very lossy, due to the fact that most of the light incident upon the mask is rendered obsolete. This experiment has since been adapted and, although the basic principles remain unchanged, more efficient methods of constructing such beams have been realised.

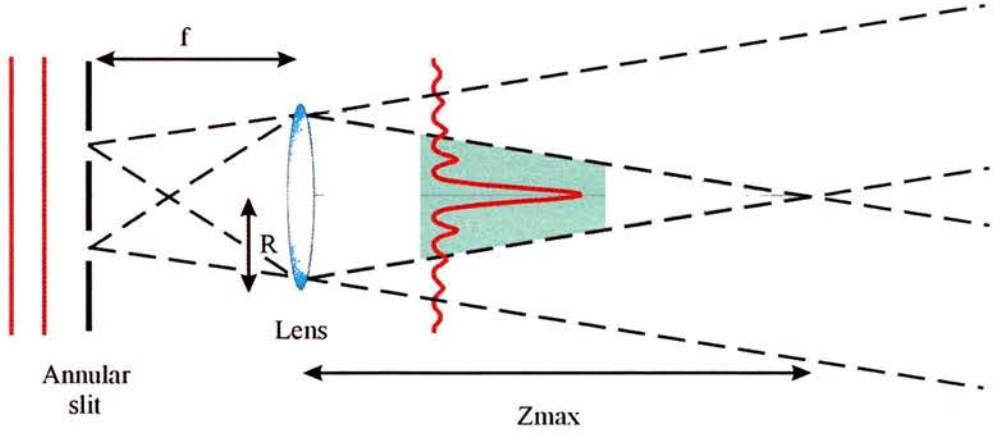

Figure 2.7. Durnin's original design for the construction of a Bessel beam by illuminating a ring with a plane wave. The lens is placed a focal length *f*, away from the annular slit, imaged through a lens of radius *R*.

An axicon is a non-diffractive optical element, also known as a conical lens (figure 2.8). A beam incident on the axicon refracts through, causing all regions to be bent in towards

the propagation z-axis, due to the lens's conical shape. This creates a superposition of waves, interfering to form a "non-diffracting" region of light [21,23]. The region over which this beam interference occurs (equation 2.12) can be described by propagation length [3];

$$z_{\max} = \frac{k}{k_r} w_0 \qquad [2.12]$$

$$k_r = k(n-1)\gamma = \frac{2.405}{r_o} \qquad [2.13]$$

where an incident Gaussian beam of waist, w_0, on the axicon has a wavevector, k. The conical wavefronts formed through the axicon follow the cone vector k_r [3] described in equation 2.13. The opening angle of the axicon (of refractive index n) indicated by γ, controls the refraction angle of the beam, and dictates the size of the central beam maximum r_o. γ can be related simply using Snell's law to the conical angle of the Bessel beam by $\theta \approx (n-1)\gamma$ [24].

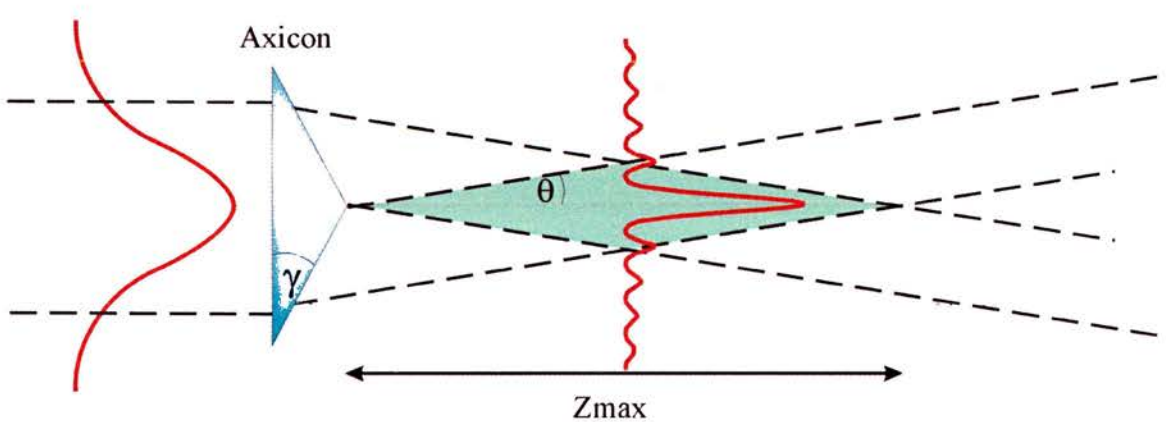

Figure 2.8. A Gaussian beam is used incident upon the axicon to generate a Bessel beam of propagation distance Z_{max}.

Due to the axicon's method of utilising the whole incident light beam, transmission is high, losing a negligible amount of light on lens reflection. This makes the axicon a highly effective choice when efficiency is of paramount importance. Other Bessel beam generation approaches can include a Fabry-Perot resonator [25] or hologram [26]. The axicon, unlike a hologram, can only produce a zeroth-order Bessel beam from a Gaussian

mode. To induce higher order Bessel beams, a hologram or a Laguerre-Gaussian beam can be used as the input to an axicon.

Telescopes, used before and after the axicon, can manipulate the resultant Bessel beam parameters to specific experimental needs. Used before the axicon, a telescope can magnify the beam to fill the back of the axicon. A larger incident beam waist creates a larger region of beam overlap, on refraction through the axicon. In addition, this provides a longer propagation distance. A lens relay after the axicon allows telescoping to resize the central core diameter.

The intensity distribution for an axicon-generated Bessel beam can be approximated, by applying the method of stationary phase to the Fresnel integral, leading to equation 2.14 [3];

$$I_B(r,z) = 2\pi(k_t w_0)\left(\frac{P}{\pi w_0^2/2}\right)\left[\frac{z}{z_{\max}}\right]J_0^2(k_r r)\times\exp\left\{-2z^2/z_{\max}^2\right\} \quad [2.14]$$

where P is the incident power, $k_t = k\sin\theta$ is the transverse component of the wave-vector k in the propagating medium, J_0 is the zeroth order Bessel function of the first kind (equivalent to the order of beam), w_0 is the waist spot size of the Gaussian beam incident upon the axicon and $z_{\max} = w_0/\sin\theta$ is the maximum propagating distance of the Bessel beam (see figure 2.6).

The Bessel beam discussed here, with beam core $r_o = 3.5$ μm, has a propagation distance of 9 mm. This is a considerable improvement over the Rayleigh range of a Gaussian beam (49 μm) with similar dimensions. However, the power contained within a Gaussian beam is considerably larger than the core of a Bessel beam of similar power. Most of the Bessel beam power resides in the outer rings. This significantly reduces the available power held within the propagation invariant central maximum.

2.8 Theoretical modelling of optical guiding

Several geometric optical guiding models can be found elsewhere in the literature, developed for a fundamental Gaussian beam [27,28,29,30,31]. In contrast, Bessel beams have received little attention in the theoretical study of light's interaction with microparticles [2]. In a collaboration with Karen Sepulveda, the observed light-particle interaction was modelled using the ray optics model developed by Gussgard and co-workers [29]. Karen's model shows the localisation of particles within the guide beam as observed experimentally. In addition, the intensity distribution of the respective beams is shown as they propagate, giving insight into the experimentally observed particle guiding behaviour discussed later.

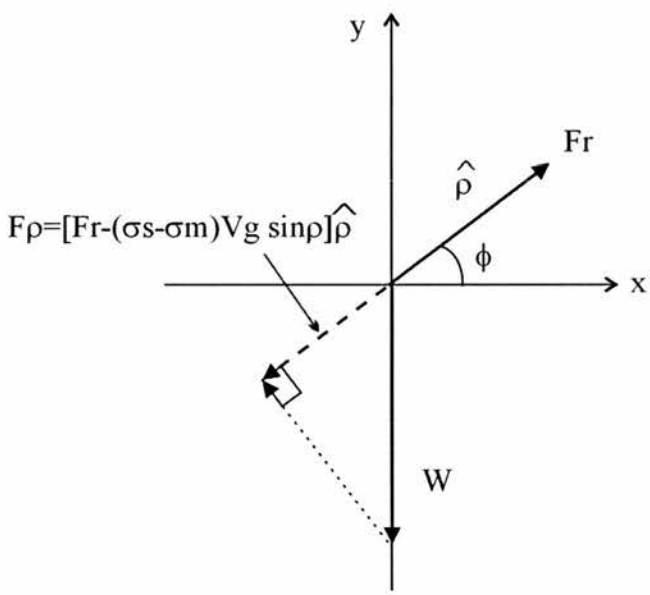

Figure 2.9. The radius of the particle a, is taken as a vector out from the origin at an angle ϕ. The weight of the particle W acts directly downwards. The total in plane force is then the radial transverse force minus the particle weight (of density σ_s, in a surrounding medium of density σ_m).

The model was implemented in the limit when the incident light beam is not strongly focused (such as in optical guides), and has been applied to both Gaussian beam and Bessel beam guiding [32]. The direction of the incident rays is considered to be parallel

to the propagating axis. Incident light creates a force exerted on a transparent sphere. This total force is broken into transverse (equation 2.15) and axial (equation 2.16) components, shown in figure 2.9, where the axial component is directed out of the page.

The transverse force localising the particle on-axis is;

$$F_r = \frac{n_m a^2}{2c} \int_0^{\pi/2} \int_0^{2\pi} I(r,z) \left[R \sin 2\theta - T^2 \frac{\sin(2\theta - 2\theta_t) + R \sin 2\theta}{1 + R^2 + 2R \cos 2\theta_t} \right] \sin 2\theta \cos\phi \, d\phi \, d\theta \qquad [2.15]$$

and the axial guiding force is;

$$F_z = \frac{n_m a^2}{2c} \int_0^{\pi/2} \int_0^{2\pi} I(r,z) \left[1 + R \cos 2\theta - T^2 \frac{\cos(2\theta - 2\theta_t) + R \cos 2\theta}{1 + R^2 + 2R \cos 2\theta_t} \right] \sin 2\theta \, d\phi \, d\theta \qquad [2.16]$$

where n_m/c is the light velocity in the medium surrounding the particle, a is the radius of the particle. The polar and azimuthal angles are denoted θ and ϕ respectively, for a spherical coordinate system whose origin is located at the centre of the particle. The integration limits correspond to the region of the sphere's surface, interacting with the incident field. In this case, the angle of integration θ corresponds to the transmission angle θ_t, given by Snell's law, for individual rays. R and T are the reflection and transmission coefficients derived from the Fresnel equations, in accordance with Roosen [27]. The coefficients were taken as an average over the two transverse polarisation directions and are appropriate for an unpolarised beam. As indicated by figure 2.9, the beam radius is taken as a positive distance in any outward direction away from the respective beam centre positions.

I(r,z) is the intensity distribution of the incident field, either a Bessel beam whose intensity is given in equation 2.17, or a fundamental Gaussian beam (equation 2.17) [6] such that;

$$I_G(r,z) = \left[\frac{P}{\pi w(z)^2} \right] \exp\left\{ -2r^2 / w(z)^2 \right\} \qquad [2.17]$$

where $w(z) = w_0 \sqrt{1 + (z/z_R)^2}$ is the beam spot size and z_R is the Rayleigh range (equation 2.11). The r and z coordinates are given by equations 2.18 and 2.19 below:

$$r = \sqrt{r_0^2 + \rho^2 \sin^2\theta + 2r_0\rho\sin\theta\cos\phi} \qquad [2.18]$$

$$z = z_0 - \rho\cos\theta \qquad [2.19]$$

where r_0 is the distance between the centre of the particle and the propagation axis and z_0 is the distance from the centre of the particle to a reference plane taken as $z = 0$. In the case of a Bessel beam, the reference plane is the axicon vertex, and the Gaussian beam reference plane is taken at the beam waist. To establish a fair comparison for guiding, the beam waist plane of the Gaussian beam was shifted to the position $z = z_{max}/2$. This position corresponds to the peak on-axis intensity of the zeroth-order Bessel beam along its maximum propagation distance.

The transverse force can be modelled as a function of the radial distance to illustrate the localisation of the particle within the beam. The presented model considers a 3 μm diameter silica sphere, immersed in water, with a laser wavelength of 1064 nm in vacuum. The Gaussian beam was given a waist radius of 3.5 μm and the Bessel beam central maximum a radius of 3.25 μm, with a maximum propagation length of 9 mm. The total Bessel beam power (equation 2.14) was 5 times greater than that of the total Gaussian beam power of 100 mW. This originates from the power distribution held within the Bessel beam rings, in comparison to the single spot obtained from a Gaussian beam.

The ideal cases for particle localisation are shown in figure 2.10 within respective light beams, and do not take into account the particle's weight. Figure 2.10(a) shows the total radial force for a Gaussian beam, showing an equilibrium and hence localisation of a particle occurring within the maximum intensity. In the case of a Bessel beam, figure 2.10(b), many equilibrium positions occur. However, for a horizontal beam geometry, the weight of the particles play an important role and should also be taken into consideration when modelling the radial forces.

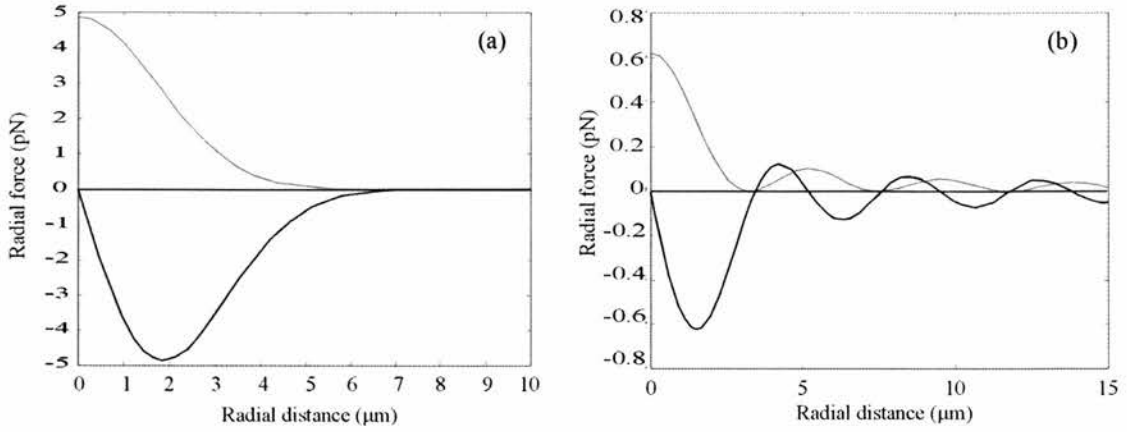

Figure 2.10. Comparison between the radial optical force exerted by (a) Gaussian and (b) Bessel beams as a function of the lateral displacement of the sphere's centre with respect to the propagation axis (black curves). The beam intensity profiles were also plotted as a reference frame (gray curves). Model simulations done by Karen Volke-Sepulveda [32].

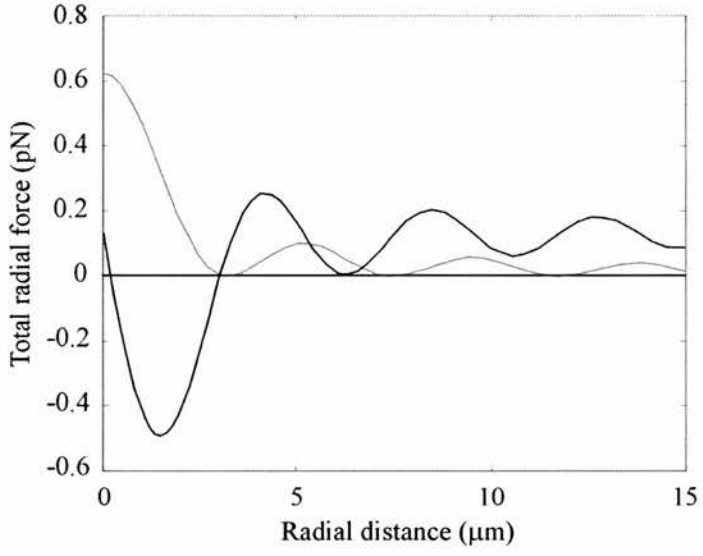

Figure 2.11. Net radial force exerted by a Bessel beam for the case of horizontal guiding, compensating for particle weight, (black curves) and intensity profile (gray curve). Model simulations done by Karen Volke-Sepulveda [32].

Figure 2.11 shows the radial force for a Bessel beam, compensated for particle weight. The particle weight is taken along the vertical downwards direction as a positive force, according to the specified sign convention. The particle weight reduces the available equilibrium position to the beam central maximum. A resultant downward shift is

produced for these parameters from beam centre (the ideal case shown in figure 2.10(b)). In this case, no equilibrium position exists in the beam's bright outer rings, this is seen graphically through no stable zero positions appearing, as observed for the ideal case. The central equilibrium position shifts 0.2 microns in figure 2.11. Similar behaviour can be modelled for the Gaussian beam allowing a central equilibrium position of the particle within the beam. Therefore, experimentally we expect to observe the radial confinement of particles within the bright central core of both Gaussian and Bessel beams.

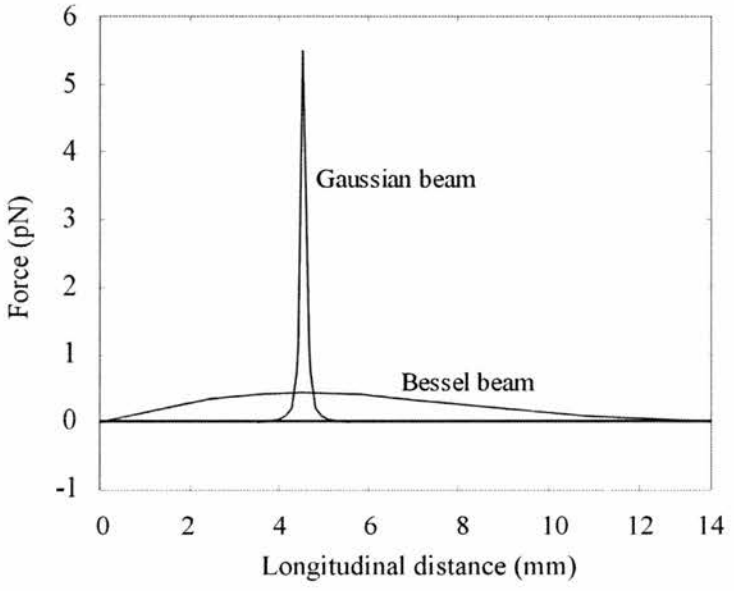

Figure 2.12. Comparison between the axial optical force exerted by Gaussian and Bessel beams. The force is taken as a function of the position of a 3 μm diameter sphere, immersed in water, along the beam propagation distance. Model simulations done by Karen Volke-Sepulveda [32].

The axial optical forces for both Gaussian and Bessel light beams were also modelled with the same particle and beam parameters used above, shown in figure 2.12. This figure clearly shows the Gaussian beam's short Rayleigh range, creating a short region in which guiding is possible. The Bessel beam, in comparison, produces a long propagation length that potentially allows guiding to occur over several millimetres. These findings are in accordance with experimental observations discussed in the next section.

2.9 Experimental design

A continuous wave Millennia pumped Ti-Sapphire laser (Spectra Physics, 3900S), operating at 780 nm, was used to provide the guiding laser light with powers of up to 1 W, figure 2.13. The beam emergent from the laser was expanded to 20 mm and collimated to fill the optic apertures. The respective beams were focussed and a rectangular quartz sample cell, known as a cuvette, placed at the beam focal region. The cuvette (Helma, 101.015-QS) had inner dimensions of 3x3x20 mm. A microscope objective (Newport, x20 magnification, NA = 0.4), placed orthogonally to the laser beam propagation direction, projected scattered light images onto a charge coupled device (CCD).

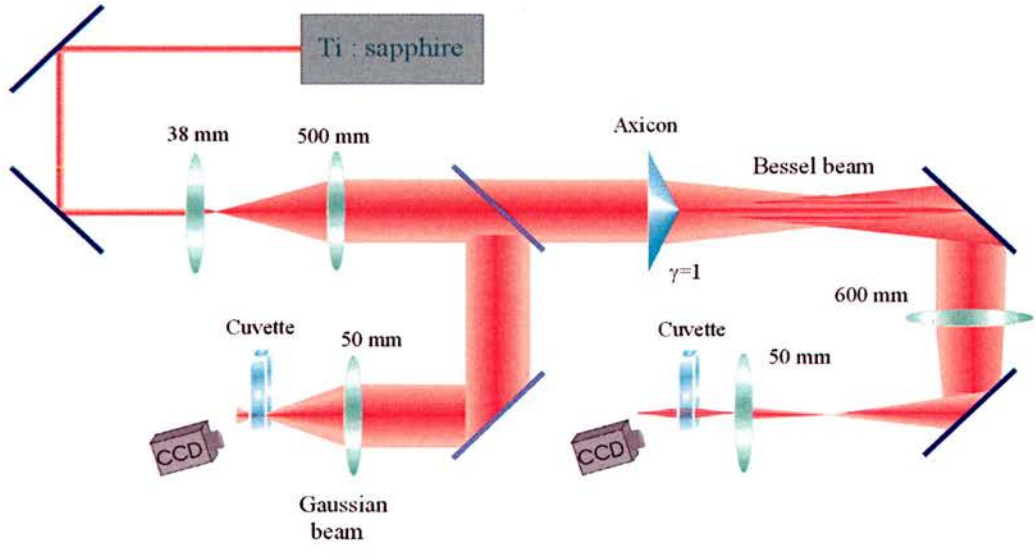

Figure 2.13. Experimental set-up of both Gaussian and Bessel beams. The Gaussian is extracted immediately before the axicon and focussed through the cell using a 50 mm focal length lens.

The cell was filled with uniform silica monodisperse colloidal microspheres (Bangs Laboratories) in either ordinary water (H_2O) or a heavy water mixture (D_2O + H_2O). The presence of D_2O was used to control the heating within the cuvette, due to its lower absorption than H_2O at the laser wavelengths used. The silica spheres ranged in diameter

from 1 μm to 5 μm allowing to a reasonable approximation operation in the Mie regime, where wavelength is smaller than particle size. Particles were suspended with a small amount of detergent, to aid mobility and act as an anti-coagulant.

At the operating wavelength, very little OH^- absorption in water occurs, greatly reducing heating in the cuvette compared to that seen using a laser at 1064 nm. The little convection present aided particles to be loaded into the optical guide beam, occasionally allowing particles to escape. A horizontal single beam geometry was constructed for guiding using both a Gaussian and zeroth-order Bessel beam. The experimental design shown in figure 2.13 provides a simple way of converting between Gaussian and Bessel beam set-ups.

For Gaussian beam guiding studies, the beam was extracted immediately before the axicon, and directed towards the sample cell. This beam was then focused through the cuvette and positioned at a height of a few millimetres above the cuvette floor, ensuring the focal region was central to the cell. A beam waist of 3.25 μm was obtained by focussing a Gaussian beam through an f = 50 mm lens. The beams were imaged using a CCD camera, viewing perpendicular to the beam propagation direction.

To allow guiding with a Bessel beam, the expanded Gaussian beam (w_o = 9.5 mm) was allowed to propagate through an axicon ($\gamma = 1^o$). This experimentally provided a central core diameter of 128 μm propagating over a distance of approximately 1 m. For the optics used here, a Bessel beam was predicted with a diameter of 68.4 μm (equation 2.13) and a 1.09 m propagation distance (equation 2.12). A second telescope was utilised to reduce the beam to a comparable diameter with the Gaussian beam. This allowed the Bessel beam to be reformed to a central maximum radius of 3.50 μm with a 9 mm propagation distance. This is considerably greater than the 43 μm Rayleigh range of the Gaussian beam. The beam created through the axicon was compared with a Mathcad model and deemed a suitable approximation to a Bessel beam.

2.10 Particle guiding velocities

Initially, the results for optical guiding using a Gaussian light beam will be presented. For each sample, the average time taken for a sphere to cross the beam's focal region was observed at different power levels and the average maximum velocity recorded. Results were taken over a distance of 320 μm using a x20 microscope objective and imaged onto a CCD. These are shown in figure 2.14. As expected, there is a linear variation in maximum guiding velocity with increase in power. The power levels were measured at the cuvette. Figure 2.14(d) shows that particles closer in diameter to that of the beam display faster guiding velocities, due to a greater radiation pressure on the sphere (equation 2.7). Particle velocities depend on sphere size, laser power and the chosen beam. For example, at the highest power levels, approximately 455 mW in the entire beam, Gaussian guiding took approximately 4 seconds and Bessel beam guiding 8 seconds for a 3 μm sphere to travel 320 μm. At the lower power level of approximately 270 mW for 3 μm spheres, guiding times can increase to approximately 15 seconds using the Gaussian beam and 100 seconds with the Bessel beam.

The guiding velocities shown are estimated over a region where particles are accelerated through the beam focal region. Particle velocity is therefore not constant. An instantaneous velocity taken at the focal plane would yield a higher result than those shown here. For this reason the guiding velocities presented serve as a crude comparison only.

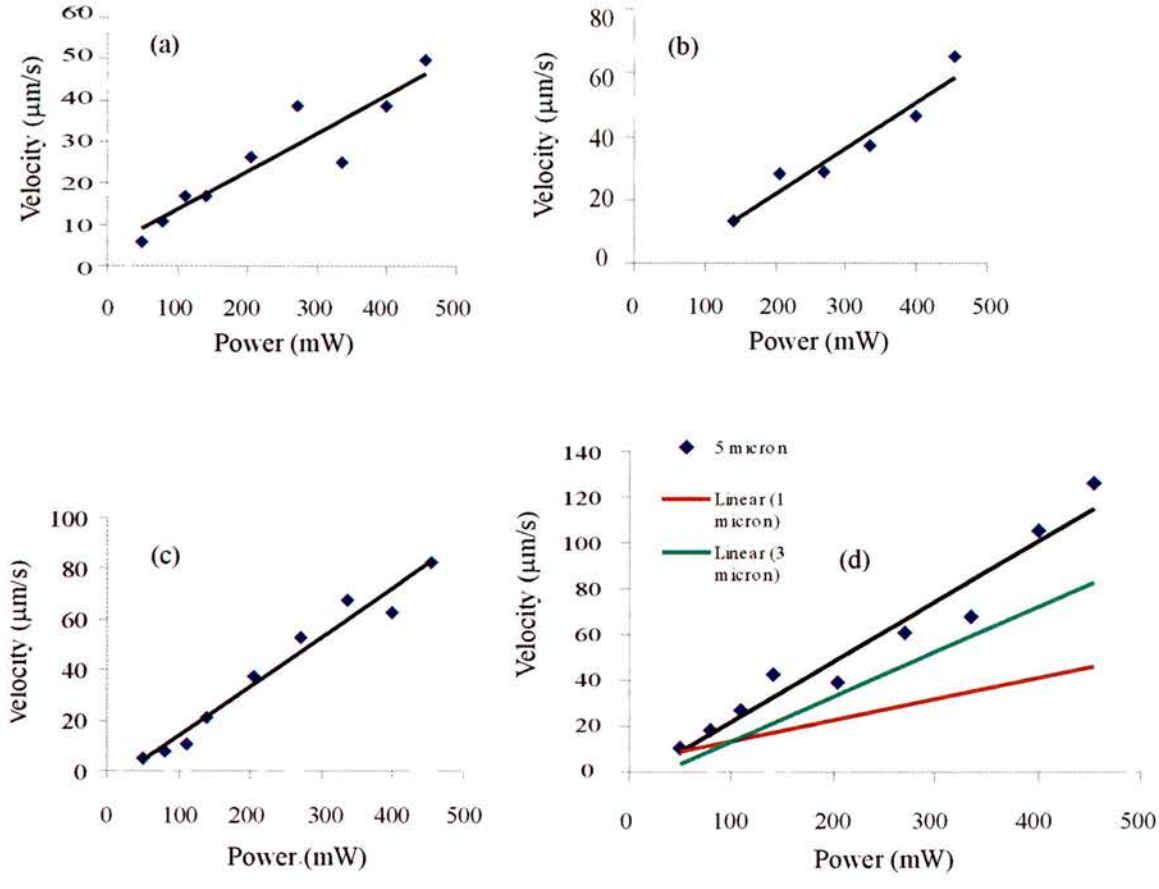

Figure 2.14. Gaussian beam guiding velocities were observed with silica spheres of diameters (a) 1 μm, (b) 2.3 μm, (c) 3 μm and (d) 5 μm, across a distance of 320 μm. The linear trend lines for 1 μm and 3 μm spheres are plotted with the 5 μm particle graph to show the systematic variation.

Guiding velocities in a Bessel beam (figure 2.15) were then considered for comparison. The Bessel beam guiding velocities are comparatively slower due to the low power contained within the central maximum. However, consistent guiding is shown along the beam propagation distance, due to the beam's non-diffracting properties. This will be discussed later in this chapter.

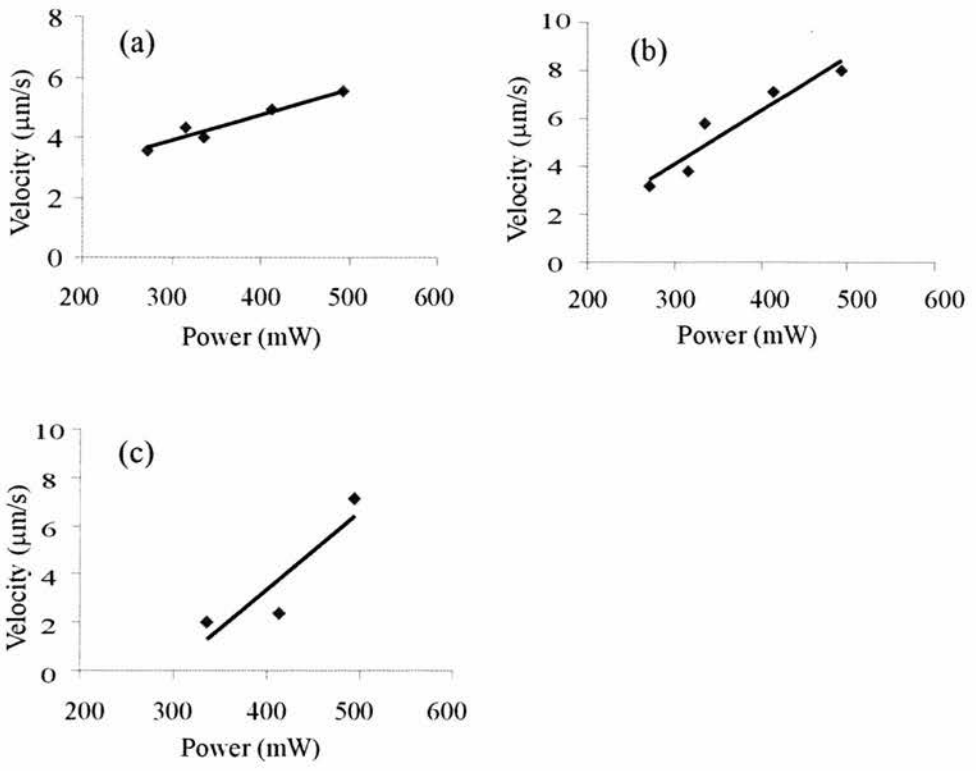

Figure 2.15. The guiding velocities of different sphere diameters (a) 1 μm, (b) 3 μm and (c) 5 μm, are observed using a Bessel beam.

In this instance, the axicon-generated Bessel beam was set up to allow the central maximum intensity of the propagating beam to coincide with the centre of the cell. The sphere velocity in the Bessel beam central maximum was observed for 1 μm, 3 μm and 5 μm spheres, figure 2.15. The power levels shown indicate the power over the entire Bessel beam. For this reason a high power levels are required to obtain sufficient guiding powers within the central maximum. For this reason graphs 2.15 do not appear to go through the origin. Data for 5 μm spheres therefore only exist at higher powers, due to the large particle mass with respect to available power in the Bessel beam central maximum.

The particle velocities obtained using the Bessel beam are realistic values due to the relatively constant velocity of the particle over the observed region. Sphere velocity was observed with a constant power and sphere size at several positions through the sample

cell. The respective velocities were found to be very similar. This was as expected, due to the Bessel beam's constant intensity distribution over its propagation length, compared to the Gaussian beam. As with the Gaussian beam, sphere diameters closer to the core diameter travel with a greater velocity.

Graphs 2.14 and 2.15 crudely show the greater power and therefore force used in the Gaussian beam to guide particles compared with the Bessel beam. This is simply due to the central maximum guiding region of the Bessel beam containing only a small fraction of the power available to the entire beam (~20 mW).

Using a sphere size of 1 μm and maintaining the power level at approximately 420 mW for both Gaussian and Bessel beam guiding situations, the velocities of the spheres were observed at three different positions through the cell. This showed an increase in velocity in the cell centre and a slight decrease in sphere velocity towards the cell walls. As expected, this follows the Bessel beam intensity profile seen in figure 2.6. The guiding of asymmetrical particles in the Bessel beam were also briefly observed. Blue filter glass was finely crushed and added to the cuvette, with water. These particles had the dramatic effect of significantly increasing particle velocity.

2.11 Particle guiding distances

The distance any single sphere travelled was also observed for both Gaussian and Bessel beams. In a Gaussian beam, spheres central to the beam propagation axis tended to accelerate through the focal region. Due to the divergent nature of the Gaussian beam, spheres easily diffuse out of the beam after passing the beam focus. The maximum guiding distance was 960 μm for a Gaussian beam of waist size 3.25 μm. For a Bessel beam of beam waist 3.5 μm this distance was considerably longer. Guiding is observed continuously across the 3 mm cuvette. Figure 2.16 shows guiding distances of 1 μm spheres in an ordinary water (H_2O) suspension medium, and figure 2.17 in a equal (50:50) mixture of ordinary and heavy water (D_2O).

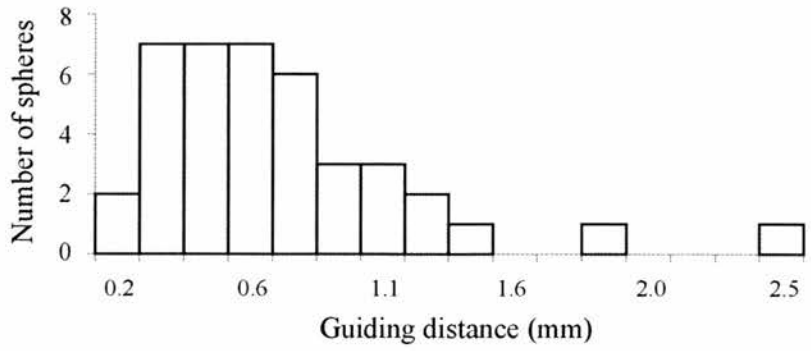

Figure 2.16. Histogram showing guiding distances for 1 μm diameter spheres immersed in H_2O using a total Bessel beam power of 452 mW.

Spheres that do not guide the whole length of the cell are believed to leave the optical guide due to convective effects, figure 2.16. This is shown in that relatively few spheres guide furthers than 1.5 mm. The addition of D_2O as a suspension medium acts to significantly reduce the heating effect. However, particles immersed in pure D_2O reduce the heating such that particles took as much as 30 minutes to appear in the field of view. The cell was therefore filled with an equal (50:50) mixture of D_2O and H_2O to reduce the heating effects present. This, as shown by the extended guiding distance in figure 2.17, allows longer guiding distances. The partial mixture of D_2O permits longer guiding distances whilst allowing convection within the cell to occur.

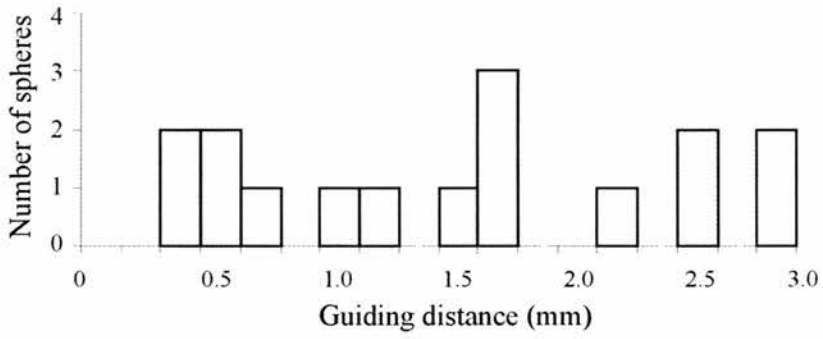

Figure 2.17. Histogram showing guiding distances for 1 μm diameter spheres immersed in an equal mixture of D_2O and H_2O, using a total Bessel beam power of 417 mW.

The extended guiding distances of the Bessel beam are shown here in comparison to the Gaussian beam. In the Gaussian beam, spheres guide a short distance due to the beam's divergent nature. Particles are localized within the beam over the Rayleigh range. In comparison, Bessel beams give extended particle guiding distances due to the beams propagation invariance. This property allows the particle to be transversely localized within a Bessel beam central maximum over a much longer distance, throughout its propagation length.

This histogram records the guiding distances of numerous 1 μm spheres at a constant total Bessel beam power of 450 mW. The distribution of guiding distances shows that spheres are as likely to travel 300 μm as to travel the length of the cell. In this experiment, the limitation on guiding distance using the Bessel beam is the size of the cell, which is only approximately one-third the propagation distance of the beam. Partial obstruction to the Bessel beam rings can also result in poor guiding distances. (An obstruction or distortion could occur on clipping cuvette edges on entering the cell.). Such distortion can effectively act to shorten the particle guiding distance.

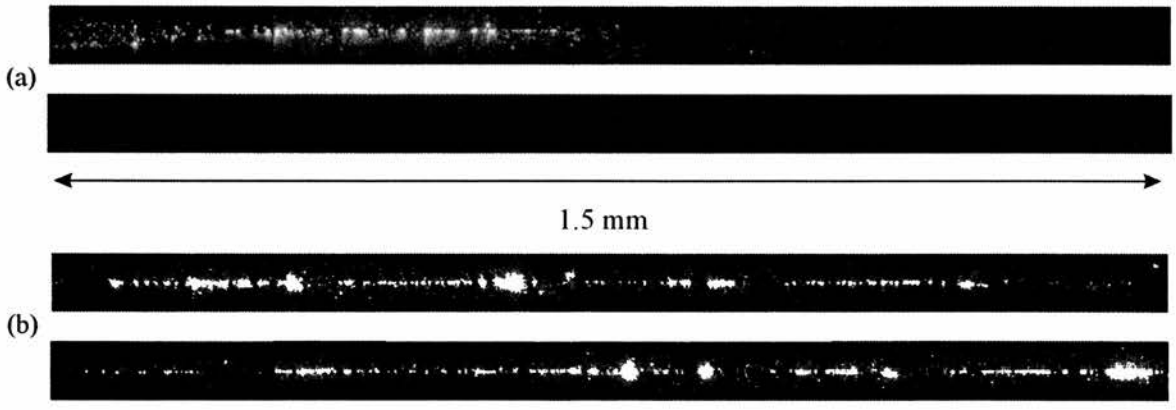

Figure 2.18. Viewed guided particles orthogonal to the light propagation using (a) Gaussian beam and (b) Bessel beam. For each guiding beam a series of images through the cell were taken. Here the full width of the cuvette 3 mm is shown over two lines. In both guiding cases 3 μm silica spheres were used.

Figure 2.18 shows a visual comparison of optical guiding across the sample cell using both Bessel and Gaussian beams. The field of view covers 3 mm, compiled by capturing adjacent frames through the full width of the cuvette. The initial few frames of the Gaussian beam guiding, shown in figure 2.18(a), shows the focal region of the beam as particles are drawn in and accelerated through the beam waist. From figure 2.18(b) the extended nature of guiding using a Bessel beam can clearly be seen and a comparatively steadier velocity is shown. Sphere velocities are dramatically lower than that seen with the Gaussian beam due to the Bessel beams non-divergent nature.

2.12 Gaussian beam versus Bessel beam guiding

Optical guiding of transparent microscopic particles along a Gaussian beam and a zeroth-order Bessel beam, has been discussed in a horizontal geometry. Gaussian beam guiding distances are short, up to 960 μm. However, beam characteristics allow fast delivery, accelerating particles through the focal plane. A Bessel beam with dimensions comparable to the Gaussian beam shows extended guiding distances of up to 3 mm, limited in this experiment by the size of the cuvette. A theoretical model constructed by K. Sepulveda, based on a ray optics approach, was used to describe the radial and transverse forces associated with both beams.

The Bessel beam guiding velocities were significantly reduced due to the power available in the beam's central maximum. The sphere velocities show a linear dependency with power for all sphere diameters for both Gaussian and Bessel beams. An important application for both beams is the guiding of cells and chromosome fragments for biomedical and lab-on-a-chip applications. Transporting particles in this way can also have applications in tissue and bio-engineering. In such applications, the Bessel beam offers substantially longer guiding distances. The work discussed here has been published in SPIE proceedings [34].

2.13 References

[1] A. Ashkin, "Acceleration and trapping of particles by radiation pressure", Phys Rev Lett. **24** 156 (1970)

[2] J. Arlt et al., "Optical micromanipulation using a Bessel light beam", Opt. Comm. **197** 239 (2001)

[3] J. Arlt et al., "Optical dipole traps and atomic waveguides based on Bessel light beams", Phys. Rev. A **63** 63 (2001)

[4] J. Durnin, J. J. Miceli, and J. H. Eberly, "Diffraction-free beams", Phys. Rev. Lett. **58** 1499 (1987)

[5] A. Ashkin and J. M. Dziedzic, "Optical levitation by radiation pressure", Appl. Phys. Lett. **19** 283 (1971)

[6] A. Ashkin et al.,"Observation of a single-beam gradient force optical trap for dielectric particles", Opt. Lett. **11** 288 (1986)

[7] S. J. Koch and M. D. Wang, "Dynamic force spectroscopy of protein-DNA interactions by unzipping DNA", Phys. Rev. Lett. **91** 028103 (2003)

[8] R. R. Huruta et al., "Mechanical properties of stored red blood cells using optical tweezers", Blood **92** 2975 (1998)

[9] M. J. Lang, P. M. Fordyce and S. M. Block, "Combined optical trapping and single-molecule fluorescence", J. Bio. **2** Vol. 1 (2003)

[10] J. Guck et al., "Stretching biological cells with light", J. Phys. Cond. Matter **14** 4843 (2002)

[11] T. K. Lake et al., "Optical trapping and fluorescence excitation with violet diode lasers and extended cavity surface emitting lasers", Opt. Express **12** 670 (2004)

[12] A. Einstein, "On the quantum theory of radiation", Phys. Zeitschrift **18** 121 (1917)

[13] A. Ashkin, "History of optical trapping and manipulation of small-neutral particle, atoms, and molecules", IEEE J. Q. Electron. **6** 841 (2000)

[14] N. Malagnino et al., "Measurements of trapping efficiency and stiffness in optical tweezers", Opt. Comm. **214** 15 (2004)

[15] M. Felgner, O. Muller and M. Schliwa, "Calibration of light forces in optical tweezers", Appl. Opt. **34** 977 (1995)

[16] K. T. McDonald, "Laser tweezers", Am. J. Phys. **68** 486 (2000)

[17] Y. Harada and T. Asakura, "Radiation forces on a dielectric sphere in the Rayleigh scattering regime", Opt. Comm. **124** 529 (1996)

[18] K. F. Ren, G. Gréhan and G. Gouesbet, "Prediction of reverse radiation pressure by generalised Lorentz-Mie theory", Appl. Opt. **35** 2702 (1996)

[19] G. Gouesbet, B. Maheu and G. Gréhan, "Light scattering form a sphere arbitrarily located in a Gaussian beam, using a Bromwich formulation", J. Opt. Soc. Am. A **5** 1427 (1988)

[20] E. Hecht and A. Zajac, "Optics", Addison-Wesley publishing company (1974)

[21] Y. Lin et al., "Experimental investigation of Bessel beam characteristics", Appl. Opt. **31** 2708 (1992)

[22] Z. Bouchal, J. Wagner and M. Chlup, "Self-reconstruction of a distorted nondiffracting beam", Optics Comm. **151** 207 (1998)

[23] R. M. Herman and T. A. Wiggins, "Production and uses of diffractionless beams", J. Opt. Soc. Am. A **8** 932 (1991)

[24] J. Rogel-Salazar, G. H. C. New and S. Chavez-Cerda, "Bessel-Gaus beam optical resonator", Opt. Comm. **190** 117 (2001)

[25] A. J. Cox and D. C. Dibble, "Nondiffracting beam from a spatially filtered Fabry-Perot resonator", J. Opt. Soc. Am. A **9** 282 (1992)

[26] A. Vasara, J. Turunen and A. T. Friberg, "Realization of general nondiffracting beams with computer-generated holograms", J. Opt. Soc. Am. A **6**, 1748 (1989)

[27] G. Roosen and C. Imbert, "Optical levitation by means of two horizontal laser beams: A theoretical and experimental study", Phys. Lett. A **59** 6 (1976)

[28] G. Roosen, "A theoretical and experimental study of the stable equilibrium positions of spheres levitated by two horizontal laser beams", Opt. Comm. **21** 189 (1977)

[29] R. Gussgard, T. Lindmo, I. Brevik, "Calculation of the trapping force in a strongly focussed laser beam", J. Opt. Soc. Am. B **9** 1922 (1992)

[30] A. Ashkin, "Forces of a single-beam gradient laser trap on a dielectric sphere in the ray optics regime", Biophys. J. **61** 569 (1992)

[31] S. Nemoto and H. Togo, "Axial force acting on a dielectric sphere in a focussed laser beam", Appl. Opt. **37** 6386 (1998)

[32] K. P. Volke Sepúlveda Ph.D. thesis, "Light beams with angular momentum and applications in optical tweezers", INAOE Puebla México, February 2003

[33] A. E. Seigman, "Lasers", University science books (1986)

[34] A. E. Carruthers, S. A. Tatarkova, V. Garcés-Chávez, K. Dholakia, K. Volke-Sepulveda and S. Chavez-Cerda, "Optical guiding along Gaussian and Bessel light beams", SPIE Proceedings **5121** 68 (2002)

Chapter 3

Optically bound matter in a counter-propagating beam geometry

3.1 Introduction

In 1970, Ashkin showed the potential for light forces to manipulate colloidal matter at the microscopic level [1]. A horizontal counter-propagating beam geometry was demonstrated to confine a single particle between two beam waists. The optical guides demonstrated by Ashkin [1], and in the previous chapter, can be exploited to create a confinement region for particles. Co-linear aligned optical guides, propagating in opposing directions, can interact to create a trapping region. Trapping occurs due to the radiation pressure from the optical guides coupled with the scattering of light on interaction with the particles. Used in this way optical forces can achieve regularly spaced particles, such as shown by Buican et al. [2]. Therefore, a high degree of order can be brought to an optical force system. In contrast to the single beam trap (optical tweezing), this method requires a balancing of forces using two propagating beams. However, unlike conventional optical tweezers, particle confinement in this instance can occur well away from cell walls, a macroscopic distance away.

The use of counter-propagating beams for particle trapping, shown for single particles by Ashkin [1], can be further developed to form an optically trapped array of multiple

particles [3]. This can be deemed a form of optically bound matter. A very different form of optical binding was first realised by Golovchenko and co-workers [4,5]. The effect of light on particles was observed through the use of cylindrical lenses to produce an elongated line of light in the focal plane. Particles were confined within the beam residing in an ordered fashion, appearing coupled within the confinement beam. The mechanism for "Golovchenko" binding was described as the interaction of the coherently induced dipole moments of microscopic spheres in an optical field creating bound matter. Such studies of ordered matter allows insight into the interaction between light and particles. This is of particular interest in the construction of two and three dimensional structures. The ability to manipulate patterns and structures can assist the assembling and sorting of matter in biomedical and materials research.

Recent interest in using light forces for the manipulation of particles has resulted in alternative techniques to create ordered confinement in two and three dimensions, by producing pre-designated light trap potentials. Such optical traps can be implemented in a number of different ways to allow the confinement of colloidal or biological particles. Examples include holographic methods [6], the phase contrast technique [7], the use of non-zero order light modes [8] and spatial light modulator technology [9]. The production of customized optical potential landscapes through these devices can create and model thermodynamic systems which give insight into mechanisms at the atomic level, or be extended to condensed matter systems [10].

In this chapter, the organisation and manipulation of one-dimensional bound arrays of microscopic colloidal particles is discussed. Thus, the ability to trap a single particle demonstrated in Ashkin's dual beam trap [1] is extended. The observation of multiple particle arrays, formed through two free-space counter-propagating Gaussian light beams, is shown. Thus, an important discovery made in this work is the specific point that the light forces confining the particles also dictate the inter-particle spacing. This type of particle manipulation may therefore be deemed a totally new form of optical binding. Though light forces determine the array separation, this system shows analogous behaviour to linear chains of atomic ions, strong candidates for quantum computing,

where electrostatic forces dominate [11]. Thus, the optically bound matter discussed here can potentially allow insight into chain dynamics that can affect de-coherence in other thermodynamic systems. Particle's dynamics, stability and chain formation behaviour are observed in detail in this experiment.

3.2 Light force optical traps

Ashkin's pioneering counter-propagating light beam trap allowed the confinement of a single particle. Subsequent studies supporting this free space beam trap observation [12] have progressed to involve the use of counter-propagating fibre optics [13] to confine single particles. The results demonstrated in this chapter show significant improvement on these light force traps, allowing multiple particle confinement. It is thought that this ability to trap larger particle chains has never been seen before due to issues of alignment, as this is critical to the array stability. Subsequent to the initial measurements conducted here, recent studies have shown the creation of multi-particle arrays utilising counter-propagating optical fibres [14]. The regular particle spacing observed within such a dual-fibre array displays parallel behaviour to the data observed here, using free-space beams. In addition, the use of two beams with similar polarisations, have been exploited to cause an interference effect, thus creating a standing wave. In a counter-propagating beam geometry, the standing wave can be used to create multiple optical trapping sites. Zemánek [15] and Schrader [16] discuss such a standing wave trap. By controlling the counter-propagating beam polarisations with respect to each other, a dual beam optical trap can be simply transformed with certainty into a possible standing wave trap [15]. The experiment discussed here, makes use of two orthogonally polarised beams to create a "self-assembled" trap, determined by the coupled scatters held by the light forces.

3.3 Experimental design

A continuous wave Ti-Sapphire laser operating at 780 nm and a 1064 nm Nd:YAG laser was independently utilised as the trapping light source. The light was expanded and split into two equal beam components using a polarisation beam splitter (figure 3.1).

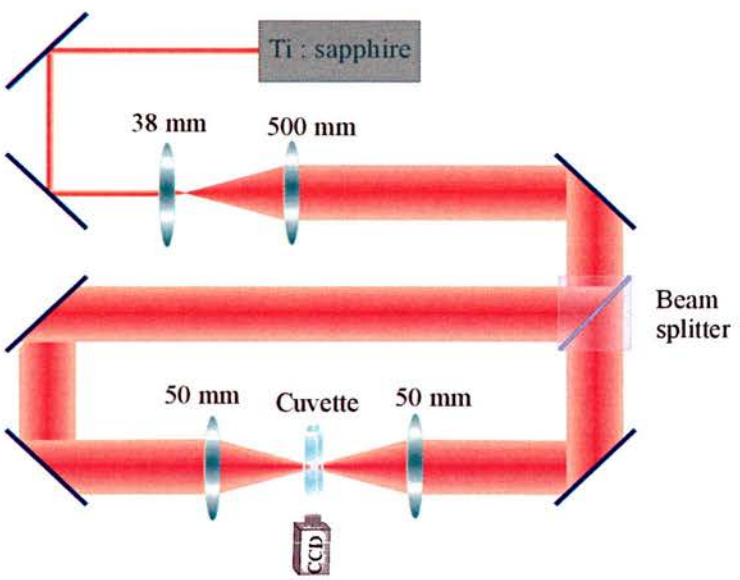

Figure 3.1. The experimental set-up of a counter-propagating beam optical trap is shown using a 780 nm Ti:Sapphire laser. The beam is expanded to fill the optics, split into two equal power beams and focussed through two f = 50 mm lenses to beam waists of 3.5 μm inside a cuvette.

Each arm was directed into a counter-propagating geometry and focussed through lenses with a focal length of f = 50 mm creating a beam waist of 3.5 μm. The beams were aligned through pinholes, one beam being kept stationary and the other aligned to it using the final mirror mount adjustors. The final focussing lenses were mounted on z-axis translation mounts such that both focal regions were aligned in close proximity with a degree of flexibility as to the chosen beam separation. A microscope objective (x20, NA 0.4, Newport), placed orthogonal (side view) to the laser beam propagation direction, projected scattered light from the spheres onto a charge coupled device. This allowed finer co-alignment of the two respective beams.

A cuvette with inner dimensions 3x3x20 mm was positioned to coincide with this beam focal region and filled with water containing silica spheres of diameter 0.4 μm. The high density of particles helps map out the intensity distribution of the two beams and hence make an estimate as to the waist separation. The two beams were positioned such that they were aligned transverse to the beam propagation with a displacement between beam waists. Respective beam waists were moved to lie approximately 150 μm apart along the common axis central to the cuvette position. Beam waists were focussed to approximately 3.5 μm in radius. The effects of this beam geometry on silica spheres of 1.28 μm, 2.3 μm, 3 μm, 5.17 μm and 10 μm was observed.

3.4 Creating a counter-propagating beam trap

The cuvette was filled with uniform silica mono-disperse colloidal microspheres (Bangs Laboratory) in a water suspension. The host medium used was either ordinary water (H_2O) or a heavy water mixture (H_2O + D_2O). As previously discussed in chapter 2, the D_2O content of the sample was used as a means to control heating within the suspension medium. In addition, a small amount of detergent was added to the samples to prevent sphere coagulation.

Initially using the 780 nm Ti:Sapphire source, two counter propagating Gaussian beams were positioned such that their beam waists lay apart by an adjustable distance of approximately 150 μm. The beams were focussed to allow easy loading of the trap, using the acceleration mechanism observed with a single Gaussian guide beam. The beam waist separation was taken as a displacement along the z-axis on divergence of the respective beam foci (figure 3.2).

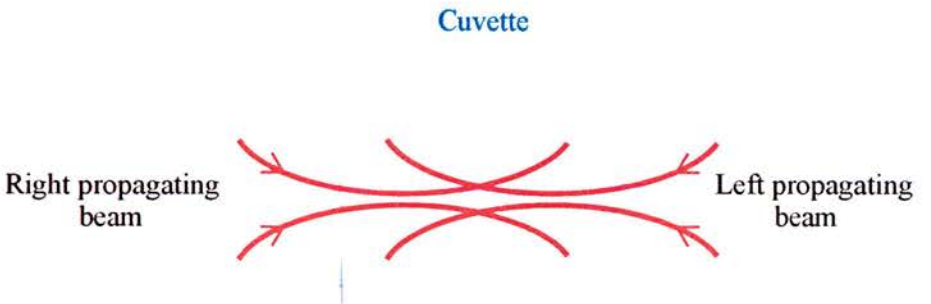

Figure 3.2. Two counter-propagating beams are focussed into the cuvette and focussed such that they are aligned transverse to each other and displaced along the propagation direction. This allows the confinement of spheres within beam waists.

The sample was prepared for the particle guiding experiment by filling the cuvette with water, and adding the particles to the top. This allowed particles to fall into the trapping beam through gravity. Particles were also able to re-enter the beam due to the presence of convection effects, as previously discussed, within the cell. The heating effects within the cuvette were dependent on the H_2O and D_2O constituent of the sample.

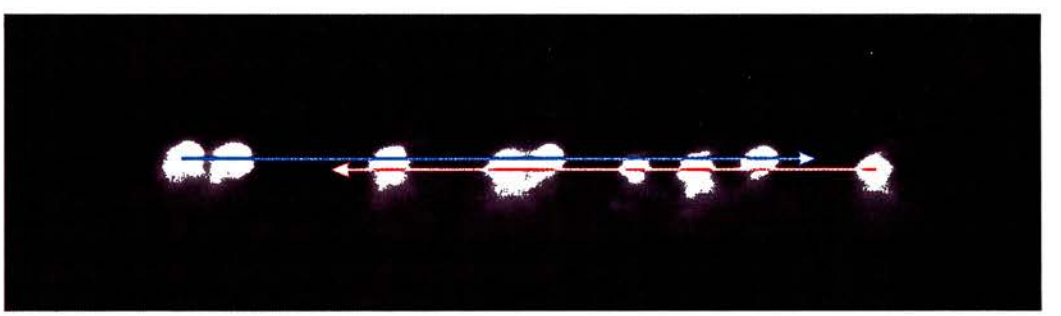

Figure 3.3. The beams are misaligned vertically, creating two opposing guide beams. Arrows are shown to illustrate the respective guiding directions. Guiding is shown with 3 μm spheres. The image has been enlarged to emphasise the closely lying beam paths.

The gradient force of light confined particles transverse to each beam propagation direction. This effectively created two oppositely facing optical guides, with the particle motion being caused by scattered light from light radiation pressure. Improvement to

beam overlap can be achieved by observing that particles move in a cyclic guiding motion, figure 3.3, which finally collapses into a line as alignment improves.

Particles are guided by the focus of the most locally intense forward propagating beam, travelling through and away from the high intensity region. The beam divergence causes a reduction in the intensity of the beam with distance from the focal region. This effectively reduces the imposed force experienced by the sphere. The further a particle guides, the less the force from this beam becomes. Particles approaching the vicinity of the return beam waist experience a pulling force as it approaches the second beam's high intensity region, and so are eventually sent back in the opposing direction. Thus, particles jump into a second path of high intensity, being guided through the return beam focus. The cyclic motion continues between opposing beam waists. This action assists with alignment of counter-propagating beams transverse to the respective propagation directions. The guiding of particles in each beam acts to help loading, leading them to access the trapping region between beam waists. Particles, initially upon entering the trap region, experience unbalanced forces. They therefore drift to reside in the equilibrium position of lowest energy within the potential well.

3.5 Experimentally creating an optical array

The 780 nm laser light was split into two beams each focussed to a waist of 3.5 μm residing approximately 150 μm apart. Particles of 3 μm in diameter were suspended in a 50:50 mixture of H_2O and D_2O within this counter-propagating geometry. The array initiated through a single particle entering the trapping region and being guided to reside in a central equilibrium position (figure 3.4).

Figure 3.4. A single trapped particle residing in a potential well created by two aligned counter-propagating beams.

A second sphere entering the optical trap causes the first sphere (figure 3.5) to be pushed from its equilibrium point. A new equilibrium position for the residing particles is thus set up between the two beams. The lowest energy stable position observed for one particle is elevated from the bottom of the single particle potential well as more particles join the array. Therefore, as particle chain length increases the configuration possesses a higher associated energy. This will be discussed later in this chapter.

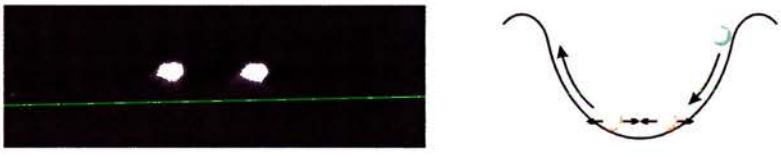

Figure 3.5. An array of two particles is shown confined within a potential well, residing in the lowest energy configuration. The potential well is not modified by the presence of the new particle and the changes introduced are treated as being due to an (optically induced) effective interaction between particles. This concept is used later to extract the particle-particle interaction energies.

The addition of new particles to the array (figure 3.6) causes the equilibrium position to gradually move further up the potential well. For the particular controlled beam parameters specified, the maximum number of particles in a stable trapped array was seven. The overall array length was approximately 150 μm in this instance. Thus, the inter-particle spacing, and the range of the effective particle-particle optical interaction, is much larger than in "Golovchenko" binding. Clearly, the physics associated with the optical binding discovered here, is distinct and new.

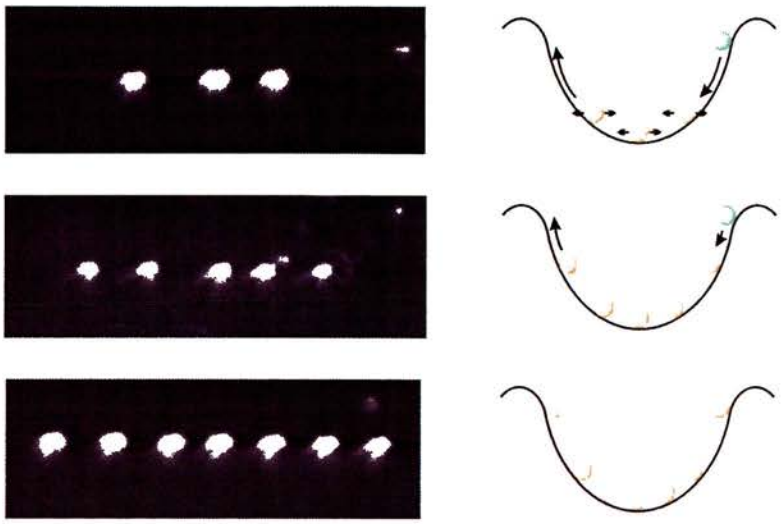

Figure 3.6. Larger particle arrays are constructed within the potential well as spheres enter the trapping region. Particle chains reside at the lowest energy positions in the potential well, for larger chains this is higher in the potential well due to the optically induced interaction between particles.

Meta-stable trapping of eight or even nine spheres in this configuration was also observed, less stable outer spheres within the array leaving over a short time period. Larger particle chains reside close to the top of the potential well showing less stability than particles residing lower in the potential well, defined by the applied intensity profile. It can be seen that particles existing in higher particle chains require less kinetic energy to leave the array. The instability of longer particle chains can be due to thermally activated loss easily overcoming the potential barrier height to escape the potential well.

3.6 Destruction of an array

Individual particles and particle chains were collectively disturbed through convective effects and interference from "drift" particles. The observation of array dynamics is, again, reflective of a system with strong inter-particle optical interactions. Furthermore, such agitations occasionally allowed residing particles to escape from the array. In some cases, massive instability to the entire particle chain was observed. Clearly any interference to the inter-particle chain dynamics causes an imbalance of forces, which can

propagate through the system. At the extreme, the result can be a complete particle chain collapse (figure 3.7). Particle arrays, on becoming unstable, collapse towards each other. This results in a particle clump residing central to the trapping region. This array instability is most likely due to guided particles entering the array too quickly and preventing the array reforming a stable configuration.

Figure 3.7. A fifth 2.3 μm particle guides into an array of four spheres along the right propagating beam. This creates an unbalance to the forces that can cause instability to particles causing the collapse of an array. The series of images shown here demonstrates the array collapsing into a central clump, which remains in the potential well.

A thermistor, accurate to a tenth of a centigrade, was placed at the bottom of the cuvette in the presence of a sphere sample suspended in ordinary water. The heating effects obtained from the two incident 780 nm counter-propagating beams were investigated. The lasers were positioned to propagate through the cell near the bottom. However, over a period of over 60 minutes, no detectable change was measured. The localised heating, obtained from the lasers, dissipates in the suspension medium such that a negligible change in temperature is observed.

3.7 Array mode motion

The experimentally observed optically bound matter forms chains, reminiscent of those obtained from trapped atomic ions in a linear Paul trap [11]. The lowest mode of collective oscillation corresponds to the centre-of-mass motion of the particle chain, causing a particle shift in unison. Optically trapped systems, in solution, are in the heavily overdamped limit; the appearance of such mode motions is therefore significant. Thus, the behaviour was investigated in detail in the experimental arrays. First, a long

particle chain was created within the counter-propagating beam trap (figure 3.8). One of the trapping beams was then blocked, causing the whole chain to guide against the propagation direction of the blocked light beam. Re-introducing the obstructed beam (within a few seconds) caused the chain to restore its initial equilibrium position. The return to equilibrium position on re-introducing the blocked beam occurred over a time scale determined by the differential force at the current array position.

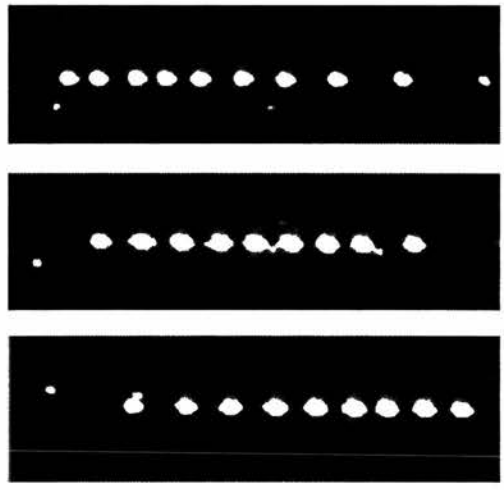

Figure 3.8. Centre-of-mass motion of the particle chain is shown. Particles guide on the attenuation or blocking of a beam, re-introducing the light causes spheres to return to their original equilibrium position.

A breathing mode motion of the trapped particle array was observed by changing the distance between beam waists. One of the lenses mounted on the precision motorised z translation stage was varied to change the focal position of one arm of the trapping beam. A long particle chain of 2.3 μm spheres was created and the corresponding breathing behaviour observed by displacing the lens along the beam propagation z-axis. The increase in beam separation effectively reduced light pressure force on the one side of the potential well. This resulted in an expansion of the inter-particle spacing. The lens returning to its original position causes the chain to restore itself to its original inter-particle spacing. This motion occurs over a long time-scale, due to the viscous suspension medium. Despite the overdamping, the mutually coupled nature of these oscillations

ensures that array excitations can arise. These particle dynamics are similar to centre-of-mass and breathing modes in underdamped chains of linear trapped ions [11].

3.8 Experimental array separation results

3.8.1 Changing particle size

The effects of changing beam wavelength, power, waist separation and waist radius were observed for different particle sizes. Initially light at 780 nm from a Ti:Sapphire laser was used to focus each arm to a beam waist of 3.5 μm. Beam waists were separated by approximately 150 μm along the z-axis with 20 mW of power in each arm. The effects of different sphere sizes in the beam were investigated. This allowed different particle sizes to be used to, effectively, map out the same potential well (figure 3.9).

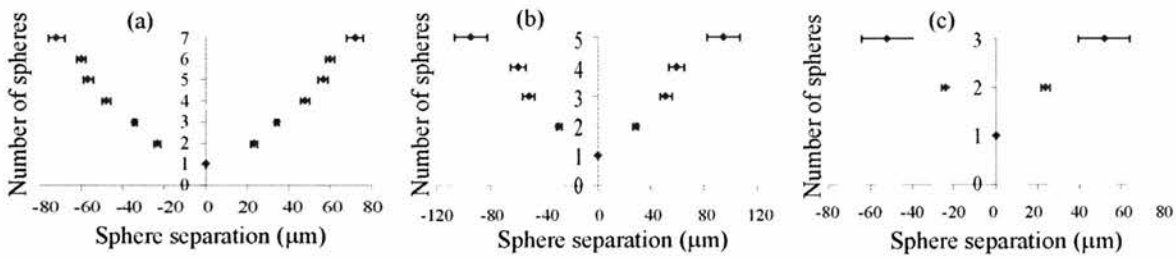

Figures 3.9. Spheres of (a) 2.3 μm, (b) 3 μm and (c) 5 μm in diameter were observed at a wavelength of 780 nm with each beam of waist 3.5 μm and 20 mW. Beam waists were focussed to lie with a separation of 150 μm.

The pseudo potential wells are formed from the result of outer sphere separation, plotted against the number of particles in the potential well. Therefore, they are not intended to give a direct representation of the associated differential force at a particular particle array. An average particle separation in an array is taken. Arrays of 2.3 μm particles were found in chains of up to seven spheres for these beam parameters. For larger particles, the number of particles in a stable array, was reduced. 3 μm spheres showed particle chains of up to five spheres. Particles of 5 μm were found to be unstable for these beam parameters.

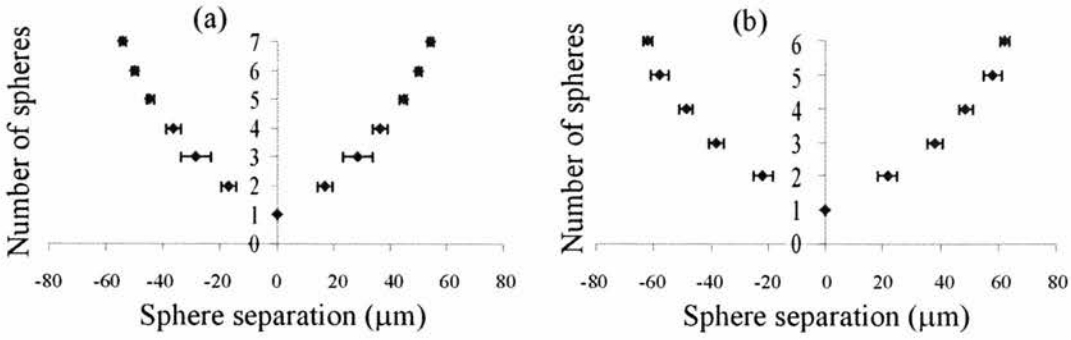

Figure 3.10. Particle sizes of 2.3 μm and 3 μm in power of 200 mW spheres with λ=1064 nm w_o=4.3 μm and beam separation of 80 μm.

The effects of changing particle size with constant parameters were also observed at 1064 nm (figure 3.10) using a Nd:YAG laser. As with the slightly lower wavelength, large particle arrays of 2.3 μm and 3 μm were observed with 200 mW of power in each arm, beam waists were focussed to 3.5 μm and focal planes placed approximately 80 μm apart along the propagation direction.

Sphere diameter (μm)	Particle array separation (μm)			
	780 nm		1064 nm	
	Two	Three	Two	Three
1.28	-	-	32.4	52.6
2.3	46.4	68.8	33.9	57.1
3.0	57.4	102.7	43.6	75.9
5.17	-	-	60.8	104.0

Table 3.1. The average separation distances of two and three sphere arrays are shown for different particle sizes. The 780 nm sphere separations were taken using a beam waist of 3.5 μm, beam waist separation of 150 μm and a power of 20 mW. The 1064 nm separations were taken with a beam waist of 4.3 μm, beam waist separation of 80 μm and a power of 200 mW.

Particles of 5.17 μm in diameter were also manipulated, preferentially occurring in single particle or two particle arrays, although, less stable arrays of up to five spheres were

observed. The average particle separation for two and three particle arrays are shown in table 3.1 for both wavelengths used. This will be used later for comparison with a theoretical model.

Polymer spheres of 10 μm were not supported by the 780 nm light, due to the larger particle mass trapped within a lower power beam. The counter-propagating beams of either wavelength did not support particles of 25 μm in diameter, (where particle size is greater than the diameter of the trapping beam) due to the larger particle mass.

3.8.2 Deviations in particle array lengths

The deviations in length of two and three particle arrays were observed for particles of 1.28, 2.3 and 3 μm in diameter. Light was used at 1064 nm using a beam waist separation of approximately 80 μm, focussed to a waist of 4.3 μm. The deviation of particle separation length in a two and three 1 μm sphere array can be seen in figures 3.11.

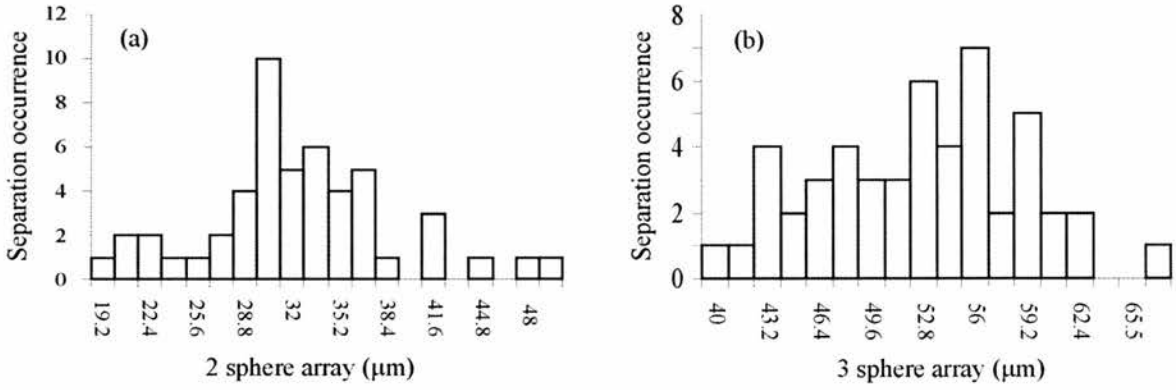

Figure 3.11. Array separation distribution for (a) two and (b) three particles of 1 μm in diameter at λ = 1064 nm with beam waists of 4.3 μm separated by 80 μm.

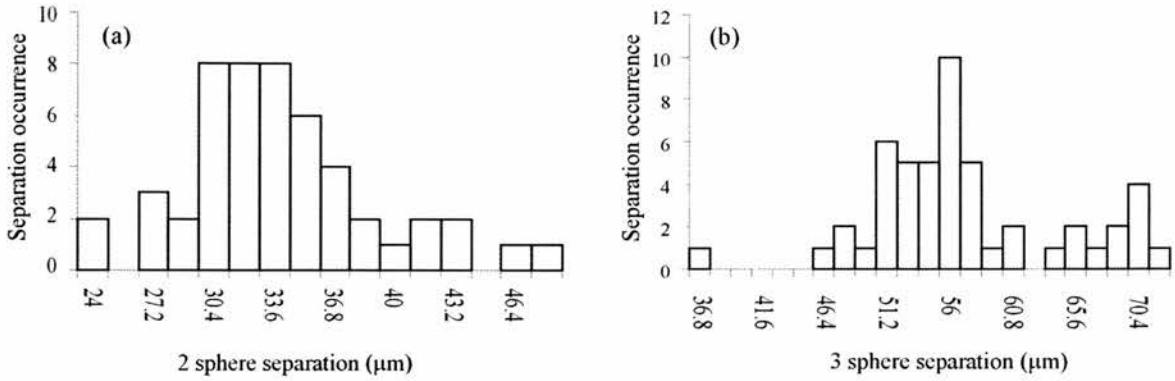

Figure 3.12. The distribution of particle separation of the outer spheres in an array of (a) two and (b) three particles of 2.3 μm in diameter is shown separated by 80 μm to a waist of 4.3 μm using 1064 nm light.

Figures 3.12 and 3.13 compare this to 2.3 μm and 3 μm sized spheres. This generally shows that as particle size increases, the particle separation also increases. A 1 μm two sphere array separated by 32.4 μm increases to 43.9 μm for similar array using 3 μm particles. Results were taken for each sphere size over 50 different sphere arrays, table 3.2. The standard deviation of particles shown, account for a 13 – 20 % deviation in sphere separation.

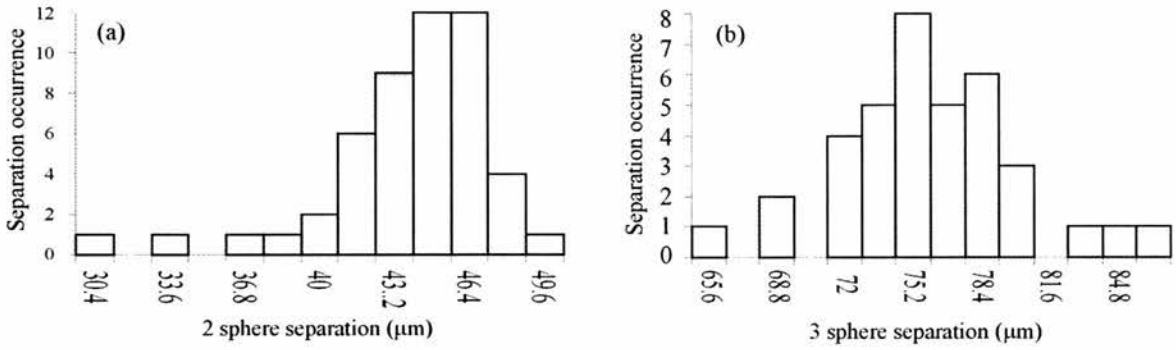

Figure 3.13. The distribution of particle separation of the outer spheres in an array of (a) two and (b) three particles of 3 μm in diameter is show separated by 80 μm to a waist of 4.3 μm.

No. of spheres	Average sphere separation (μm)		
	1 μm	2.3 μm	3 μm
2	32.4 ± 6.4	33.4 ± 5.1	43.9 ± 3.0
3	52.6 ± 6.2	57.1 ± 7.3	56.3 ± 1.9

Table 3.2. The average sphere separation is shown with the standard deviation of particles for 1 μm, 2.3 μm and 3 μm particles in an array of two and three spheres.

3.8.3 Change in beam power

The effect of changing the power in both beams was investigated with 1 μm particles shown in figure 3.14. Light at 1064 nm was used at a beam separation of 80 μm and a waist of 4.3 μm. Altering the laser power equivalently in both beams was not observed to alter the sphere separation positions.

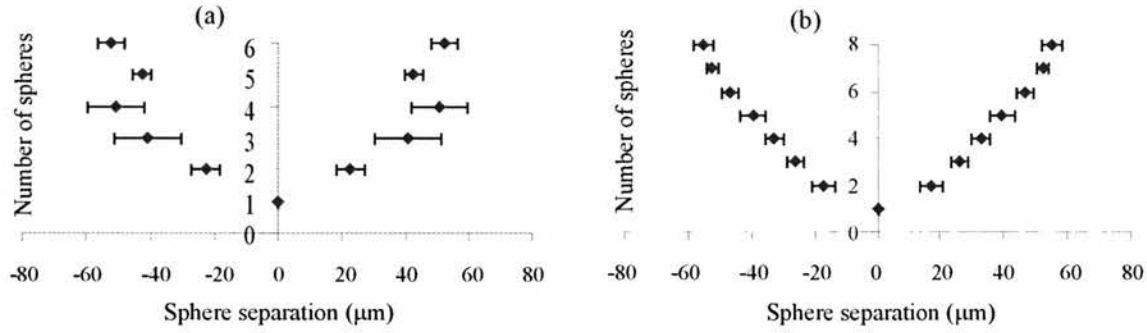

Figure 3.14. 1 μm spheres were observed with $\lambda = 1064$ nm, $w_o = 4.3$ μm and beam separation of 80 μm. Initially a power of 200 mW was used (a), which was compared to a power of 100 mW (b).

These particle separations fell well within array length deviation. The first case for a two-sphere array shows a separation of 45.2 ± 4.5 μm with a power of 200 mW compared to the second case of 34.4 ± 3.8 μm compared to 100 mW. This can be inferred from figure 3.18, where a reduction in power does not affect the differential force. A higher trapping

power did however result in higher light scattering from the spheres, observable using the CCD camera.

3.8.4 Change in beam separation

Figure 3.14 above shows 1 μm spheres forming arrays with a beam separation of 80 μm. With the power kept at 200 mW the beam separation was increased to approximately 100 μm, figure 3.15. This allows arrays of up to seven spheres to be formed compared to six particles bound in an optical configuration.

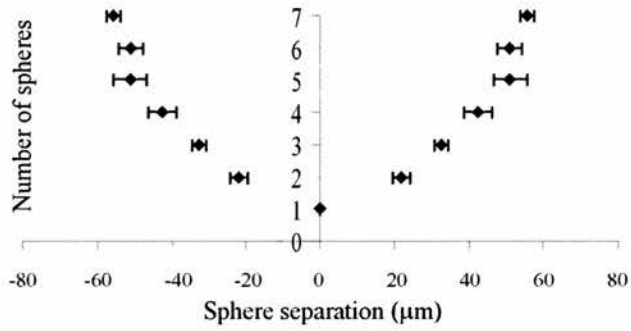

Figure 3.15. Particle arrays of 1 μm spheres with 1064 nm light focussed to 4.3 μm and separated by 100 μm, beam power of 200 mW was used.

3.9 Electrostatic interaction

Consideration was given whether electrostatic interactions could potentially play some role in the array formation. This kind of interaction, between charged spheres in solution, can be described by the Derjaguin, Landau, Verwey and Overbeek theory [17,18]. Here a screening length, due to the presence of atomic and molecular ions in solution, limits the Coulombic interaction. However, the observed array length, and importantly the inter-particle spacing, is completely incompatible with typical nanometer distances over which electrostatic interactions occur in water-based colloidal systems.

For the experimental parameters used here, the screening length could not plausibly be even 100 nm (calculated by S. Tatarkova using [17]), and so any electrostatic interactions would be restricted to a length scale much lower than the observed inter-particle spacing. Furthermore, any role of electrostatics in this system was discounted through dispersing the spheres in 1 Molar NaCl for some experimental runs. Should electrostatics play an important role, particles residing within an array should sit far apart and on addition of NaCl lie closer together. However, no discernable change was observed in the inter-particle spacing for the arrays, thus validating the premise that the array is created solely through light force effects.

3.10 Potential well and array modelling

3.10.1 Ray optics model

The construction mechanism of optically bound arrays can be thought of as arising from light scattering effects, and the subsequent balancing of radiation pressure. This ray optics model forms the basis of the assumption that refocusing of light determines the array inter-particle separation. Any given transparent particle in an array radiates light, acting as a lens (figure 3.16) and thus refracts most of incident light.

Light radiation pressure from the focussed input beams, coupled with this secondary light radiation pressure force, interacts with an adjacent sphere. In this concept model, a combination of light forces is thought to create equilibrium positions in which the array of spheres can reside. Each sphere in the formed array is "optically" coupled to each of the other spheres.

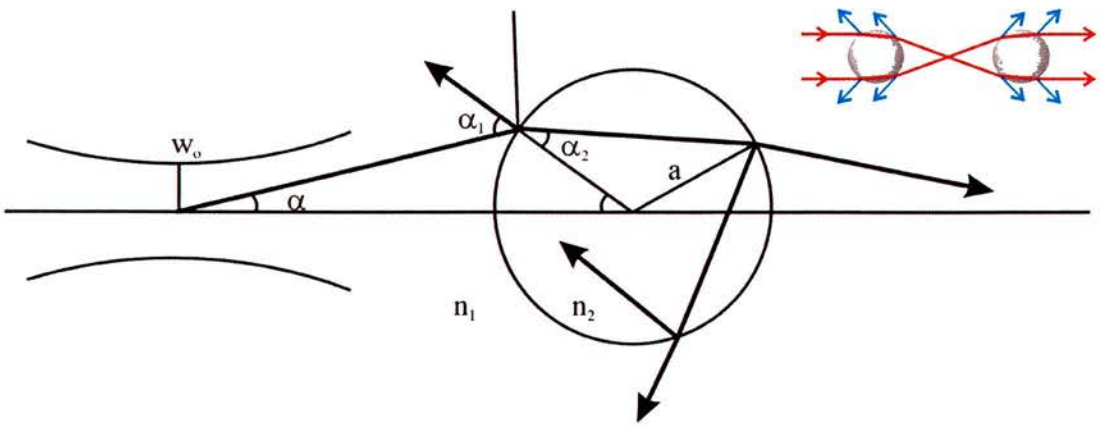

Figure 3.16. The re-focussing effect suggested by the ray optics model indicates a focussing distance that was calculated. Inter-particle spacing should then be comparable to twice the focal distance.

The model is basic, not taking into account incident wavelength, and assuming particle size is always smaller than beam waist. The calculations of the model agree, to within uncertainties, with the experimentally observed spacings. For example, a 3 μm sphere experimental separation is 44 μm, well matched to 50 μm, theoretically.

Sphere size (μm)	Focal distance (μm)	Sphere separation (μm)	
		Theory	Exptl
1	8.3	16.6	32.4
2.3	19.1	38.2	33.9
3	24.9	49.8	43.6
5	41.6	83.2	47.8

Table 3.3. Focal distance gives the theoretical focussing distance of a two sphere array, particle spacings are double this distance. Comparison is made with experimental data obtained using 1064 nm for a beam waist of 4.3 μm and beam separation of 150 μm.

A numerical ray optics model, done by S. Tatarkova using [19], was applied to calculate the predicted equilibrium separation for a two sphere array, table 3.3. The beams are not tightly focussed and therefore input angles were assumed to be small, essentially parallel

to the propagation axis (as previously assumed for modelling a Gaussian guiding beam section 2.8). The optical axial force associated with the spheres, according to the geometric optics model used above (figure 3.16), was calculated for a single beam (equation 3.1) [19,20].

$$Fz = \frac{4P_o}{\upsilon}\int_0^{\theta m}\left(\frac{a^2}{\omega}\right)G(\omega)H(\theta)d\theta \qquad [3.1]$$

where P_o is the total power in one arm, a is the particle radius and v is the speed of light through the particle suspension medium. G(w) (equation 3.2) is the Gaussian beam intensity distribution denoted as;

$$G(w) = P_o \exp\left(-\frac{2r^2}{w^2}\right) \qquad [3.2]$$

where $r - a\sin(\theta)$ and w is the beam radius at the particle centre set away from the waist. $H(\theta)$ (equation 3.3) is a function dependent on the incident and refracted ray angles, where R and T are the respective reflectance and transmittance coefficients.

$$H(\theta) = \cos(\alpha_1)\sin(\theta)\left[\begin{array}{c}\cos(\alpha_1 - \theta) + R\cos(\alpha_1 + \theta) \\ -\dfrac{T^2[\cos(\alpha_1 + \theta - 2\alpha_1) + R\cos(\alpha_1 + \theta)]}{1 + R^2 + 2R\cos(2\alpha_1)}\end{array}\right] \qquad [3.3]$$

This model was adapted for the case of two spheres confined within beam waists separated by 150 μm. This argument describes light focussed by a spherical lens to calculate inter-particle spacing. From this separation distance a force can be inferred, taking into account the fraction of light incident on the sphere (the beam waist is larger than the particle radius). The optical force exerted on the second sphere due to the first for both 2.3 μm and 3 μm diameter spheres is calculated to be 0.180 pN (model using equation 3.1), using a wavelength of 780 nm focussed to beam waists of 3.5 μm. An optical force of 22.13 pN was calculated using 1064 nm light focussed to a 4.3 μm spot size.

In the terms of this model, particles contained within the array each reside in their own local potential well. Taking the above case as an example, consider a two sphere array where light is focussed by each respective particle to a position approximately midway

between the two spheres. In this instance, one potential well containing both spheres exists, consisting of a double well light potential governing where individual particles lie. Using this argument arrays containing a greater number of spheres can be treated in a similar manner. Each sphere acts to create a new potential well within the multi-body system. This yields a net effect of forcing the array of particles farther up the well created in order to balance the forces and reach an equilibrium position. Despite calculated sphere separations being within experimental deviation, a more detailed analysis has shown that this initial model does *not* accurately describe the optical binding mechanism. In this model the effect of scattered light from the particle is not taken into consideration. This is the subject of further discussion in this chapter.

3.10.2 Modelling the potential well

The observation of equilibrium positions for an array of particles can be explained through a single particle potential well model. This well can be mapped out theoretically by considering the axial force associated with each propagating beam.

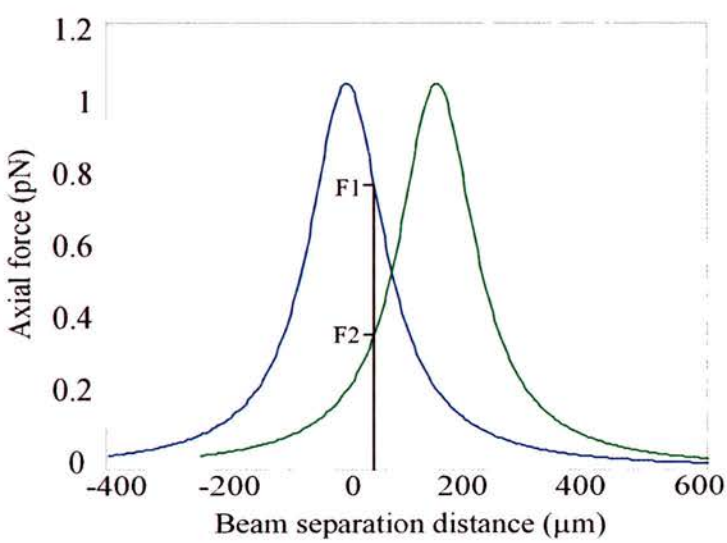

Figure 3.17. The graph shows the associated axial force on a single particle, due to two 780 nm counter-propagating Gaussian beams with 25 mW in each beam. Beam waists of 3.5 μm reside at the points of maximum axial force. *F1* and *F2* are the forces associated with the right and left propagating beams. Modelling done by S. Tatarkova.

The interaction conditions of dielectric spheres of radius a, with a single Gaussian beam of wavelength λ, is considered when the relation $a > \lambda$ is satisfied. Axial force is proportional to beam intensity and calculations follow those presented elsewhere (equation 3.1) [12,19,21]. The difference in the associated force of the opposing beam can be similarly modelled. The variation in axial force along the z- beam propagation axis (figure 3.17) is considered for 780 nm light with 25 mW in each arm. This model shown is for 3 μm particles confined within beam waists of 3.5 μm lying 150 μm apart (experimental parameters previously discussed in section 3.5).

For co-linear beams with a displacement between waists along the propagation axis, a near parabolic optical potential results. Equilibrium positions at the lowest energy configuration for a given number of spheres exist at the intersection of the two curves in figure 3.17. Each sphere in an array experiences the same value of differential force ΔF (figure 3.18), which can be calculated. Particles entering the trap interact with the existing coupled system to form a larger stable particle configuration (figures 3.4, 3.5 and 3.6).

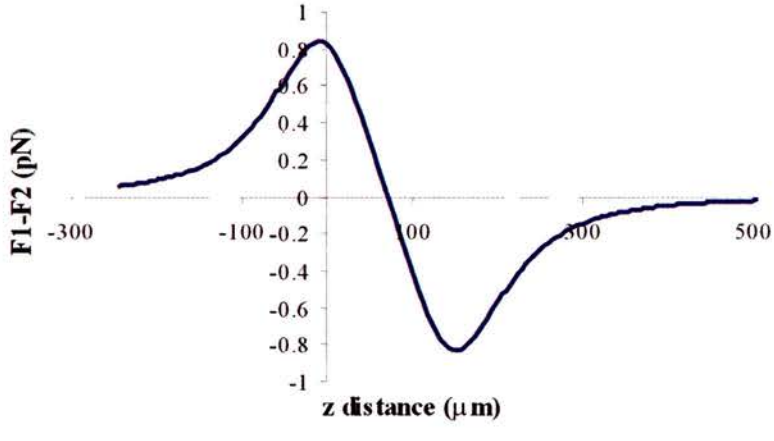

Figure 3.18. The resultant force obtained on a single particle from the differential in axial force from the two opposing light beams (F_1-F_2) shown in figure 3.17. Maximum and minimum values represent beam waist positions, which form a potential well whose gradient is shown. The central linear portion of this plot corresponds to a region of parabolic potential.

The parabolic potential well in which a single particle would reside can be obtained through integration of the linear differential force of the combined beams shown in figure 3.18. Beam waists are positioned at the maximum and minimum positions of the graph. The slope shown corresponds to the trap stiffness, analogous to a spring constant, and will be used later to obtain a trap frequency.

3.10.3 Trap frequency and interaction energy

Quantitative information can be obtained through collating data from the observed array lengths. A trap potential can be mapped, the exact form of which can be obtained and used to calculate the axial trap frequency. The kinetic energy of the trap (equation 3.4) can be described in terms of a frequency ω [22];

$$E_K = \frac{1}{2} m x^2 \omega^2 \qquad [3.4]$$

where particles of mass m, diffuse within the optical trap yielding a particle deviation length x. As previously discussed, arrays can be thought of as a chain of coupled oscillators. The potential energy of the particles (equation 3.5) can therefore be described as;

$$U = \frac{1}{2} k x^2 \qquad [3.5]$$

where k is a constant. Equating these two energy expressions provides an axial trap frequency, equation 3.6.

The potential well can be considered to take the form of the difference in the two counter-propagating beam intensities. The resultant was previously shown in figure 3.18. The gradient of this net force potential, equivalent to the trap stiffness k, is described in equation 3.7.

$$\omega = \sqrt{\frac{k}{m}} \qquad [3.6]$$

$$F = -\frac{dU}{dx} = kx \qquad [3.7]$$

This allowed a natural trap frequency to be found for each sphere size using 780 nm and 1064 nm light with the experimental parameters previously discussed (section 3.8). Namely, for a laser wavelength of 1064 nm two beam waists of 4.3 μm with 200 mW lay 80 μm apart, and for 780 nm each beam contained 20 mW in a beam focussed to 3.5 μm set apart by 150 μm. Therefore, through the observed particle spacings, and thus the trap stiffness, the associated energies of the particle-particle interactions were mapped for a two-particle array. These are shown in table 3.4.

Particles (μm)	Force (pN)	Energy (eV)	Frequency (Hz)
780 nm			
2.3	0.34	0.53	233.3
3.0	0.55	0.86	199.2
5.17	1.25	1.95	132.8
1064 nm			
1.28	0.13	0.20	340.8
2.3	0.38	0.59	254.0
3.0	0.63	0.98	21.3

Table 3.4. Trap frequencies for a 2-particle array and the associated energy for 780 nm and 1064 nm light at a range of sphere sizes. These traps are much softer than those associated with conventional optical tweezers.

The force obtained from the model in section 3.10.2 yields a k value using equation 3.7. Thus the particle-particle interaction energy and the trap frequency can be deduced. The trap frequency obtained is valid for a particular particle size due to its dependence on particle mass (equation 3.6). The 1064 nm interaction energies were mapped for particles of 1.28 μm, 2.3 μm and 3.0 μm in diameter. For incident light at 780 nm, particles of 2.3 μm, 3.0 μm and 5.17 μm were used. These energies reflect the multi-body interaction between particles residing in an array induced by the incident light.

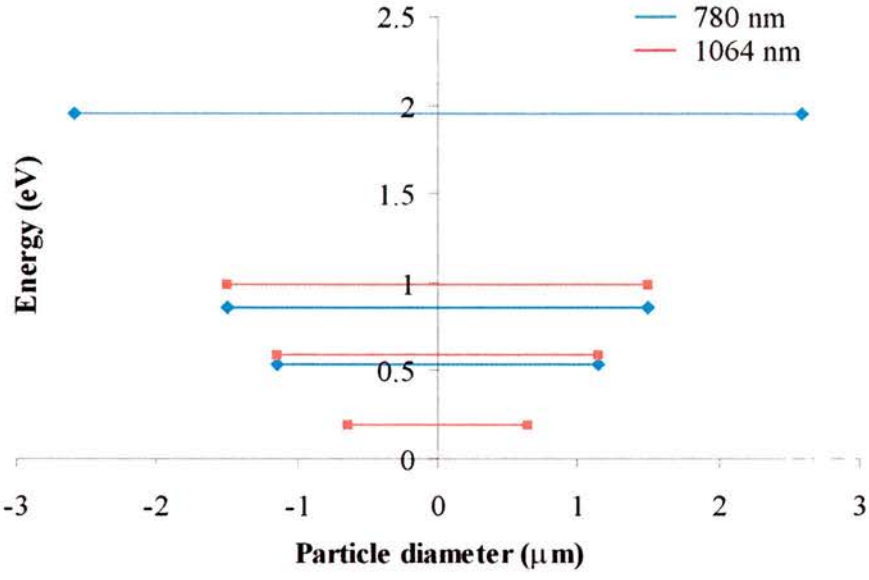

Figure 3.19. The natural trap energies are shown for a single particle (ranging from 1.28 μm to 5.17 μm) held within 780 nm (shown in blue) and 1064 nm (shown in red) light.

Interaction energy between particles for different sphere sizes were determined shown in figure 3.19 for traps formed using 780 nm and 1064 nm light. The particle diameter is demonstrated on the x-axis through horizontal lines. It can be seen that larger particles have higher interaction energies. In addition, the incident wavelength of 1064 nm yields a slightly higher energy than that obtained using 780 nm light for particles of similar size. From these combined data sets, information about the form of the optically-induced interaction between particles may be determined, for example how multi-particle chain lengths fall off, limited by the beam waist separation, figure 3.5.

3.11 Theoretical force model

In collaboration, a theoretical model was designed by Ewan Wright in Matlab [23] to allow a more accurate study of the trapping mechanism in the experiment described. The model is based on paraxial optics; a way to solve the Helmholtz equation for the theory of light propagation using an approximate solution. The approximations used for this model assume a small incident light angle and a large focussed beam waist compared to the light wavelength.

3.11.1 Helmholtz paraxial approximation

The model consists of two counter-propagating laser beams of frequency ω, centred on the z-axis in opposing directions. The beam geometry interacts with a system of N transparent dielectric spheres of mass m, refractive index n_s, and radius R, immersed in a host medium of refractive index n_h. The sphere centres are positioned at $\{\vec{r}_j(t)\}$, where j = 1,2,…,N. The electric field of the counter-propagating beams can be written as equation 3.8;

$$\vec{E}(\vec{r},t)=\frac{\hat{e}}{2}\left[\left(E_+(\vec{r})e^{ikz}+E_-(\vec{r})e^{-ikz}\right)e^{-i\omega t}+c.c.\right] \qquad [3.8]$$

where ê is the unit polarisation vector of the field and $k=n_h\omega/c$ is the wave vector of the field. $E_\pm(\vec{r})$ are the slowly varying electric field amplitudes of the right or forward propagating (+) and left or backward propagating (-) fields. As in the experiment, the incident fields (equation 3.9) are assumed to be collimated Gaussian beams. Beam waists lie at longitudinal coordinates of $z=-L/2$ for the forward field and $z=L/2$ for the backward field. These fields can be described by [23];

$$E_+(x,y,z=-L/2)=E_-(x,y,z=L/2)=\sqrt{\frac{4P_o}{n_h c\varepsilon_o \pi w_o^2}}e^{-r^2/w_o^2} \qquad [3.9]$$

here $r^2=x^2+y^2$ describes the beam shape in the focal plane where w_o is the initial Gaussian spot size; P_o is the input power in each beam. It is assumed that all spheres are contained between the beam waists, lying within length L>>R.

Initially the dielectric spheres are assumed in a fixed configuration where the centres are defined by $\{\vec{r}_j(t)\}$ at time t. The dielectric spheres then provide a spatially inhomogeneous distribution of the refractive index that can be written in the general form (equation 3.10);

$$n^2(\vec{r})=n_h^2+(n_s^2-n_h^2)\sum_{j=1}^{N}\theta(R-|\vec{r}-\vec{r}_j(t)|) \qquad [3.10]$$

where $\theta(R-|\vec{r}-\vec{r}_j(t)|)$ is the Heaviside step function, equal to unity positioned within the sphere centred on $\vec{r}=\vec{r}_j(t)$, and zero outside the sphere. Therefore, refractive index

distribution can be simplified to $n^2(\vec{r}) = n_h^2 + (n_s^2 - n_h^2)$ in the presence of a sphere, and $n^2(\vec{r}) = n_h^2$ elsewhere.

The paraxial approximation is defined by the condition that the double differential of the electric field is negligible compared to the other terms. The counter-propagating fields therefore evolve from the wave equation according to equation 3.11, written following standard approaches [24] as;

$$\pm\frac{\partial E_\pm}{\partial z} = \frac{i}{2k}\nabla_\perp^2 E_\pm + ik_o\frac{\left[n^2(\vec{r}) - n_h^2\right]}{2n_h}E_\pm \qquad [3.11]$$

where $k_o = \omega/c$ and $\nabla_\perp^2 = \partial^2/\partial x^2 + \partial^2/\partial y^2$ is the transverse Laplacian describing beam diffraction. Again spheres are assumed to lie within the beam waists. These equations describe the electric fields $E_\pm(\vec{r})$ of the beams, which change with the sphere configuration within an array. The fields are adiabatically slaved to the instantaneous sphere configuration, despite sphere motion causing a corresponding change to the refractive index distribution.

3.11.2 Equations of motion

The progression of sphere centres $\{\vec{r}_j(t)\}$ in reaction to the incident fields can be described by equations of motion providing an intensity distribution throughout the system. The time-averaged dipole interaction potential relative to that for a homogeneous dielectric host medium, between the counter-propagating fields and the system of spheres is given by [25];

$$\begin{aligned} U(\vec{r}_1,...,\vec{r}_N) &= -\int dV\varepsilon_o\left[n^2(\vec{r}) - n_h^2\right]\left\langle \vec{E}_2 \right\rangle \\ &= -\frac{\varepsilon_o}{4}(n_s^2 - n_h^2)\sum_{j=1}^{N} dV\theta\times(R - \left|\vec{r} - \vec{r}_j(t)\right|)\left[\left|E_+(\vec{r})\right|^2 + \left|E_-(\vec{r})\right|^2\right] \end{aligned} \qquad [3.12]$$

where the angular brackets signify a time average which destroys fast-varying components at 2ω arising from equation 3.8. Importantly, the dipole interaction potential $U(\vec{r}_1,...,\vec{r}_N)$ depends on the spatial configuration of the spheres, due to the counter-

propagating fields depending on the sphere distribution (equation 3.12). In this form, each sphere ($j = 1,2,...,N$) from its interaction with the local intensity contributes to the dipole interaction potential (equation 3.12). The equation of motion describing the sphere centre (equation 3.13) then becomes;

$$\gamma \frac{\partial \vec{r}_j}{\partial t} = \vec{F}_{grad,j} + \vec{F}_{scatt,j} \qquad [3.13]$$

assuming an overdamped sphere motion through the host medium with viscous damping coefficient, γ. Here $\vec{F}_{grad,j} = -\nabla_j U(\vec{r}_1,...,\vec{r}_N)$, ∇_j signifies a gradient with respect to $\vec{r}_j$, and $\vec{F}_{grad,j}$ and $\vec{F}_{scatt,j}$ are the gradient and scattering forces experienced by the jth sphere. An expression for the scattering force is given below in equation 3.15.

Simulations of a three-dimensional system, with modelling of the electromagnetic propagation, are difficult in the presence of many spheres. However, the symmetry of the system can assist to reduce the calculations involved. A combination of the dipole interaction potential, gradient force and scattering force is assumed to provide the transverse confinement potential. Thus cylindrically symmetric Gaussian beams control the sphere motion directed along the z-axis. This means that the sphere centres are positioned along the z-axis, $\vec{r}_j(t) = \hat{z} z_j(t)$, and the gradient and scattering forces are also directed along the z-axis $\vec{F}_j = \hat{z} F_j$. The sphere distribution along the z-axis is assumed to be symmetric around $z = 0$, the beam foci located at $z = \pm L/2$. This means that the centre of one sphere lies at $z = 0$, two spheres lie at $z = \pm D/2$, and three spheres lie at $z = 0, \pm D$ (where D being the sphere separation distance). These symmetric configurations of arrays of up to three spheres are considered here. For an array of more than three spheres the situation becomes more complicated.

These above approximations allow the equations of motion for the sphere centres to be described as seen in equation 3.14.

$$\gamma \frac{\partial z_j}{\partial t} = F_{grad,j} + F_{scatt,j} \qquad [3.14]$$

For simplicity, to illustrate how calculations are performed the case of two spheres ($N=2$) is considered. For a sphere separation of D the counter-propagating fields between $z=[0,L]$ is calculated using the beam propagation method. From the electric fields the dipole interaction energy $U(D)$ can be numerically calculated for a given sphere separation. The resulting axial gradient force in the z-axis direction is then $F_{grad}(D)=-\partial U/\partial D$. Thus, by calculating the counter-propagating fields for a variety of sphere separations, a numerical value for the gradient force can be obtained, acting on the relative coordinate of the two spheres. For this system, an approximate scattering force (equation 3.15) along the positive z-axis for the jth sphere [27] can be taken as;

$$F_{scatt,j} \approx \left(\frac{n_h}{c}\right)\left(\frac{\sigma}{\pi R^2}\right)\int_0^R 2\pi r dr \frac{\varepsilon_o n_h c}{2}\left[\left|E_+(x,y,z_j)\right|^2-\left|E_-(x,y,z_j)\right|^2\right] \qquad [3.15]$$

where σ is the scattering cross-section. This formula results from the generic relation $F_{scatt}=n_h P_{scatt}/c$ [26] for unidirectional propagation, with scattered power $P_{scatt}=\sigma I_o$ where I_o is the incident intensity. The integral describes the difference in power between the two counter-propagating beams integrated over the sphere cross-section. When this is divided by the sphere cross-sectional area, πR^2, the averaged intensity difference over the spheres is obtained.

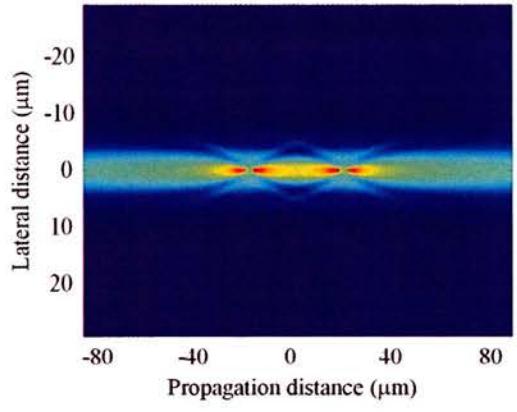

Figure 3.20. The scattering force results in an intensity profile of two spheres integrated over a defined area.

For the case of two spheres, the scattering force $F_{scatt}(D)$ is evaluated at the position of the sphere at $z = D/2$ for a variety of sphere spacings. A similar procedure can be applied to the case of three spheres. This scattering force can be mapped out in an intensity profile shown in figure 3.20, using 780 nm light focussed to a spot 3.5 μm separated by 80 μm.

3.11.3 Model limitations

The theory described using this model has some limitations. An assumption is made that a combination of scattering and/or dipole forces act to trap the spheres transverse to the propagation direction confined to the z-axis. For this to hold true the sphere diameter must be less than the laser beam diameter $2w_o > D$. Furthermore, the assumed paraxial propagation neglects any large angle or backscattering of the laser fields. However, when light is incident on a sphere there is an associated wave vector uncertainty $\Delta KD \cong 2\pi$. Backscattering can occur when $\Delta K \cong 2k$ within the uncertainty that an incident wave, of wave vector k along a given direction, is converted into $-k$. The condition $D > \lambda / 2n_h$ is therefore imposed, to avoid backscattering, allowing the initial paraxial assumptions to be obeyed.

The axial gradient and scattering forces for an array of two and three spheres are compared here with experimental results. However, the scattering cross-section for a sphere, incorporating all sources of scattering, cannot be calculated quantitatively as with the gradient force. This model is therefore used to calculate the equilibrium sphere separations when $F(D) = 0$. This is done separately for the gradient and scattering forces, which does not depend on the cross-sectional area value. Equilibrium positions found for calculated sphere separations for a set of beam parameters can, therefore, be compared with experimental values. Comparing theoretical predictions with experiment for $N = 2,3$ arrays also allows the dominant source of the axial trapping mechanism to be inferred.

3.12 Model results and experimental verification

To compare theory with experimental results a number of parameters must be considered, namely the incident wavelength, beam waist, beam waist separation, spheres size, sphere refractive index and host refractive index. Most of these parameters are known to a high degree of accuracy. For example, the laser wavelength was either a 1064 nm Nd:YAG or a 780 nm Ti:Sapphire laser. The effects of varying one parameter with respect to the others were investigated.

3.12.1 2.3 μm particle model verification

The case of 2.3 μm diameter spheres is considered for both two and three sphere arrays, as previously discussed experimentally in section 3.8. For two spheres an average sphere separation of 34 μm was obtained, for a beam waist of $w_o = 4.3$ μm at a laser wavelength of $\lambda = 1064$ nm. Experimentally, the beam waists were thought to lie 80 μm apart with an estimated error of 100 μm. Experimental distances were estimated using the CCD with a x20 magnification objective. Accurate observation of the beam focal plane proves difficult due to the slowly focussing of the beams over the field of view. To quantify the large error on this parameter, the field of view is approximately a third of the Rayleigh range. The model was used to vary beam separation within the limits of experimental error. A predicted particle separation of 34 μm was found with a beam waist separation of 180 μm, figure 3.21.

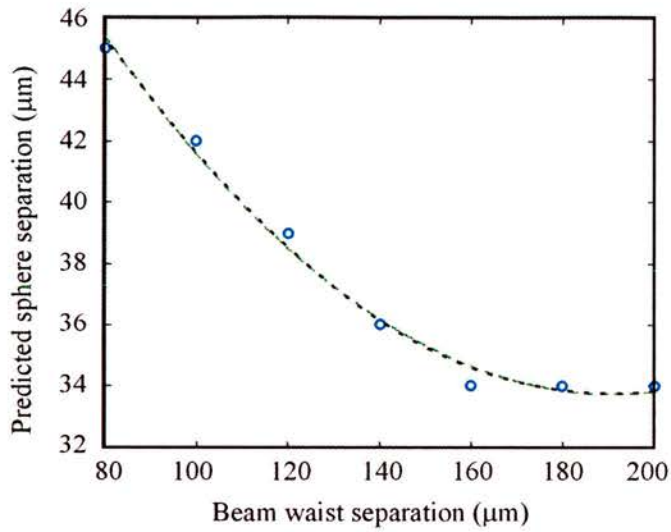

Figure 3.21. The predicted 2.3 μm sphere separations are shown for a range of beam waist separations from 80 – 200 μm.

The distance between beam waists can be modelled to show that the separation becomes less critical as it increases. For small beam waist separations (say $l << 80$ μm), even slight alterations can cause dramatic changes to the sphere separation distance. Due to the crude method of measuring beam separation, the error can easily be realised, making the predicted separation less surprising. Changes to the waist separation distances at these larger distances show a gentler change in sphere separation, giving rise to less uncertainty between theory and experimental data. The intensity distribution in the x-z plane for this configuration was previously shown in figure 3.20. It is predicted that equilibrium positions are predominantly formed through the scattering force, as shown in figure 3.22(a). No such equilibrium appears in the gradient force around the beam separation region of interest, shown in figure 3.22(b).

The same sphere parameters used in the model for the three sphere array case, experimentally discussed in section 3.8, predict a sphere separation of 62 μm, figure 3.23 showing the distance between adjacent particles. The total array length is therefore double this theoretical value.

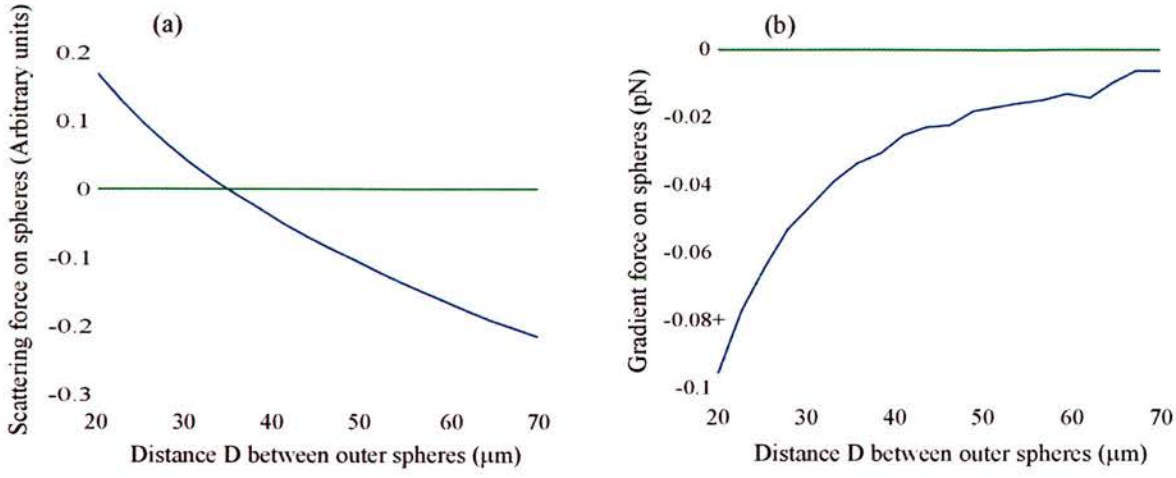

Figure 3.22. (a) Scattering and (b) Gradient forces are shown for two 2.3 μm silica spheres with 4.3 μm beam waists placed 180 μm apart using 1064 nm light. Note that for the gradient force no zero position exists.

Experimentally, a sphere separation of 57 μm was observed falling within the standard deviation of experimental measurements, agreeing well with the model predictions. As with the two sphere case, the scattering force dominates over the gradient force; the gradient force does not reach an equilibrium position in the region of interest.

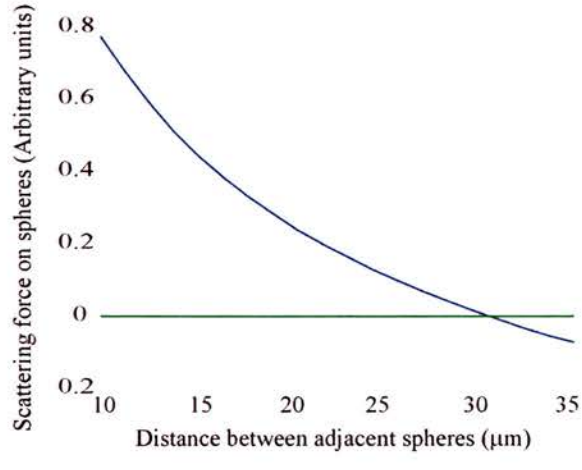

Figure 3.23. Scattering force on three 2.3 μm silica particles with 4.3 μm beam waists placed 180 μm apart using 1064 nm light. The distance between adjacent spheres corresponds to half the total array length.

Light at 780 nm was also used to manipulate 2.3 μm spheres modelling arrays of two and three spheres. Each beam was focussed to a waist of 3.5 μm separated by 180 μm. For this wavelength a two sphere array found equilibrium positions in the scattering force at 39 μm compared to 46 μm, found experimentally. In a three sphere array, the outer spheres were experimentally observed to lie a separation of 68 μm apart, also matching a theoretically positioned scattering force at 69 μm. It is probable that both forces play an important role in the optical binding mechanism; however, the scattering force appears to be the dominant factor in this case.

3.12.2 Model verification for 1064 nm and 780 nm light

Light at 1064 nm was modelled using a range of sphere sizes. As before, the beam waists of 4.3 μm were set 150 μm apart. Theoretically modelled data was compared to experimentally obtained results, previously discussed in section 3.8. Table 3.5 shows results for arrays of two and three spheres. As with the case for 2.3 μm spheres, equilibrium positions were found in the scattering force, and not the gradient force.

Sphere diameter (μm)	2 spheres		3 spheres	
	Theoretical (μm)	Experimental (μm)	Theoretical (μm)	Experimental (μm)
1.28	16	32	28	53
2.3	34	34	62	57
3.0	47	44	74	76
5.17	54	61	-	-

Table 3.5. Theoretical model data compared to experimentally obtained data for 1064 nm light using particles of 1.28 μm, 2.3 μm, 3 μm and 5.17 μm.

Theoretical sphere separations, for particles of 2.3 μm, 3.0 μm and 5.17 μm, show good agreement with experiment as can be seen. A three sphere array of 5.17 μm particles was

not supported experimentally. This also agrees with the model, in that no equilibrium position was found around the region of interest.

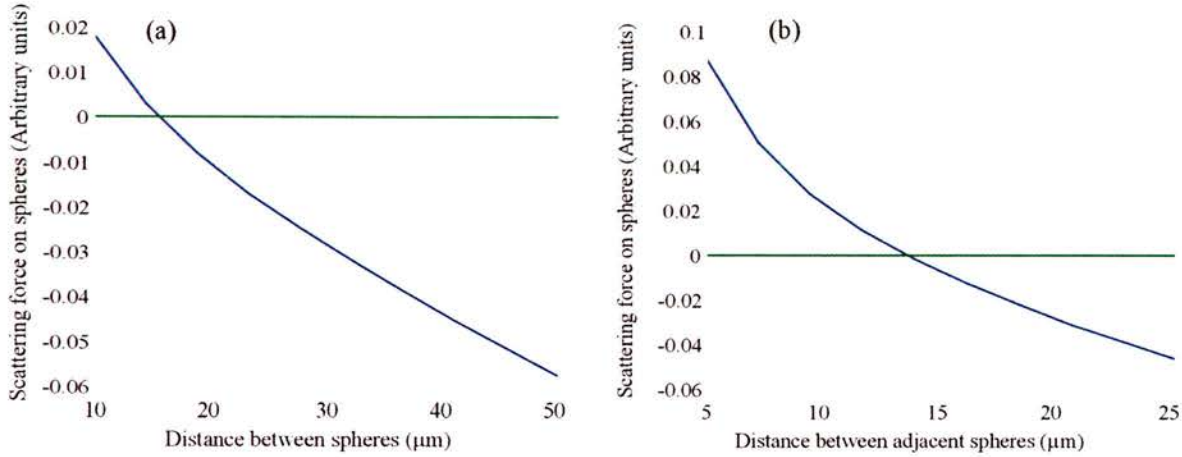

Figure 3.24. Arrays of (a) two and (b) three 1.28 μm spheres modelled with 1064 nm light. In both cases the beam waist is set at 4.3 μm separated by a distance of 180 μm.

It can be seen from table 3.5 that, for 1.28 μm particles, there is a large discrepancy between experimental and theoretical values. This sphere size, although supported experimentally by the light, is in the limit where the model breaks down. Figures 3.24 show equilibrium positions are found at 16 μm and 28 μm theoretically. Approximately half that expected and no correlation with experimental results could be found. As before, 780 nm light was focussed to beam waists of 3.5 μm, lying 150 μm apart. Good agreement is found between experiment and theory, for particles of 2.3 μm and 3 μm in diameter (table 3.6).

Scattering force equilibrium positions were found corresponding to the experimental sphere separations. Also in agreement with experiment, a stable array of 5.17 μm particles could not be found at this wavelength. No equilibrium positions were found for the given parameters (w_0=3.5 μm, separated by 180 μm) for either scattering or gradient forces between the separation of the beam waists.

Sphere diameter (μm)	2 spheres		3 spheres	
	Theoretical (μm)	Experimental (μm)	Theoretical (μm)	Experimental (μm)
2.3	39	46	68	69
3.0	40	57	80	102

Table 3.6. Theoretical model data compared to experimentally obtained data for 780 nm light using particles of 2.3 μm and 3 μm.

3.12.3 Refractive index variation

Predicted sphere separation is influenced by the refractive index difference between the spheres and the surrounding medium. The silica particles used in this experiment ranged in diameter from 1-5 μm with a manufacturers refractive index determined between 1.42 – 1.46 (Bangs Laboratories Inc.). The host medium is also well known to be either H_2O or an equal portion of H_2O and D_2O mixture (refractive indices of H_2O and D_2O are 1.333 and 1.328 respectively).

Using light at 780 nm with 25 mW, beam waists were set at 3.5 μm lying 150 μm apart. The system was modelled varying the refractive index of 2.3 μm spheres between 1.42-1.46, showing a gradient force equilibrium position smoothly changing between 47 μm and 49 μm and scattering force equilibrium position between 27 μm and 26 μm. A change in refractive index due to the host medium also showed no appreciable change in the sphere separation distance between suspensions of H_2O and D_2O.

3.12.4 Beam parameter variation

The 780 nm beam waist size was measured to a high degree of accuracy using an intensity profiler. Whereas the 1064 nm waist, due to the counter-propagating beam method of construction and imposed space constraint, was inferred from a high particle density or milk solution. The model was used to investigate the effects of the beam waist

uncertainty using 780 nm with 2.3 μm particles. A power of 25 mW was used as before with a beam waist separation of 150 μm; the refractive index of the particles was set at 1.43 and the host set at 1.33. The gradient (37 μm to 25 μm) and scattering force (24 μm to 22 μm) equilibrium positions varied for a change in beam waist from 3.0 μm to 1.0 μm. However, using the calculated beam waist size, compared to the inferred value, suggests sphere separation remains within experimental deviation even though an observable change to sphere separation is seen. In addition, variation to the model beam power had no effect on sphere separation, varying between 25 mW to 200 mW. The power in each beam therefore acts as a scaling force factor, rather than displacing the sphere separation equilibrium positions.

A significant error arises in obtaining an accurate beam waist separation value, where errors are indicated to be of the same size as estimated waist separation. As previously discussed, the beams were mapped out using a weak milk solution or a high particle density solution (0.4 μm spheres). This allowed the scattered light from the sample to be used to infer a beam waist separation. The model can therefore be used to help restrict the separation error, fixing the beam waist separation on a single result allowing the behaviour of the model to be examined when varying other parameters. However, the error in the beam waist separation is not as extreme as it first sounds. Modelling the system for a range of beam waist separations from 80 μm to 200 μm results in a predicted range of sphere separations as shown in figure 3.23 for 2.3 μm diameter spheres.

Although initially the beam waist separation difference makes a reasonable difference to the predicted sphere separation, around 180 μm for waist separation at 1064 nm, is relatively flat. Therefore, even if there is not a large error in this value, the predicted result does not vary significantly. This increases confidence that the correct beam waist separation is theoretically obtained with a higher degree of uncertainty than is suggested by experimental measurements. However, for 780 nm where the beam waist separation is thought to be 100 μm, the error increases.

3.13 Multiple array trapping sites

New theory developed in collaboration with Ewan Wright [23], and with subsequent confirmation through a sister experiment here at St Andrews (N. K. Metzger) using a dual-optical-fibre trap, suggests multiple trapping sites in an array configuration may be obtained. Experimental data for the free-space beam trap shows that there is evidence to support this.

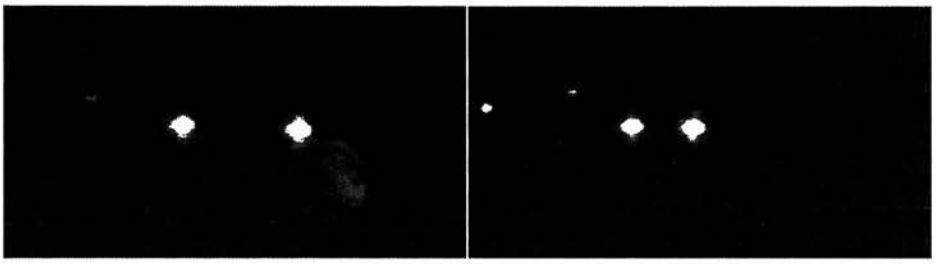

Figure 3.25. Images of an array showing two different stable sphere separations. The second sphere separation arising from a third sphere disturbing the array configuration causing a different separation to be observed.

This behaviour can be seen in figure 3.25. The first frame shows two stable spheres residing in an array. A third sphere joins the array destabilising one of the original spheres, which leaves the trapping region. An array of two spheres remains in the optical trap (seen in the second frame). However, the sphere separation observed is clearly a different distance to the initially observed spacing.

Particle separation for two and three 1 μm sphere arrays were observed, shown in figures 3.26 and 3.27. The most commonly observed particle separation for 1 μm spheres using 1064 nm light (w_o=3.5 μm separated by 150 μm) shows a two sphere separation of 45.2 ± 14.4 μm and a three sphere configuration of 81.9 ± 34.0 μm. These two figures show there is clearly a larger spread of sphere separation distances, considerably larger than the estimated 20 % sphere separation error previously observed.

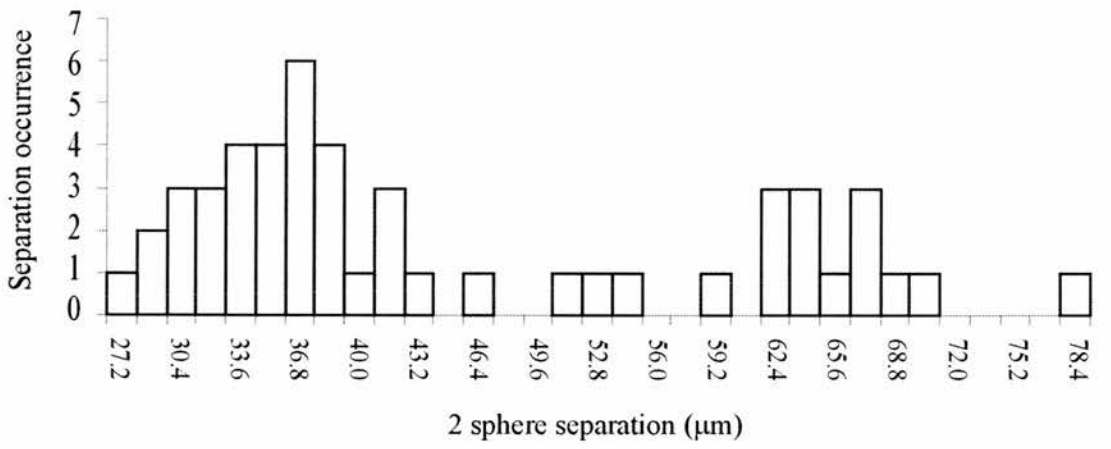

Figure 3.26. Histogram showing distribution of 1 μm particles in a two particle array. This distribution suggests a stable trapping site and a meta-stable site.

Sphere separation, as shown in figure 3.25, can therefore form stable or meta-stable configurations at more than one equilibrium position. Due to the fact that the model breaks down at 1 μm sized spheres, it is difficult to model this behaviour, as this dual position effect was not noticeable using other sphere sizes.

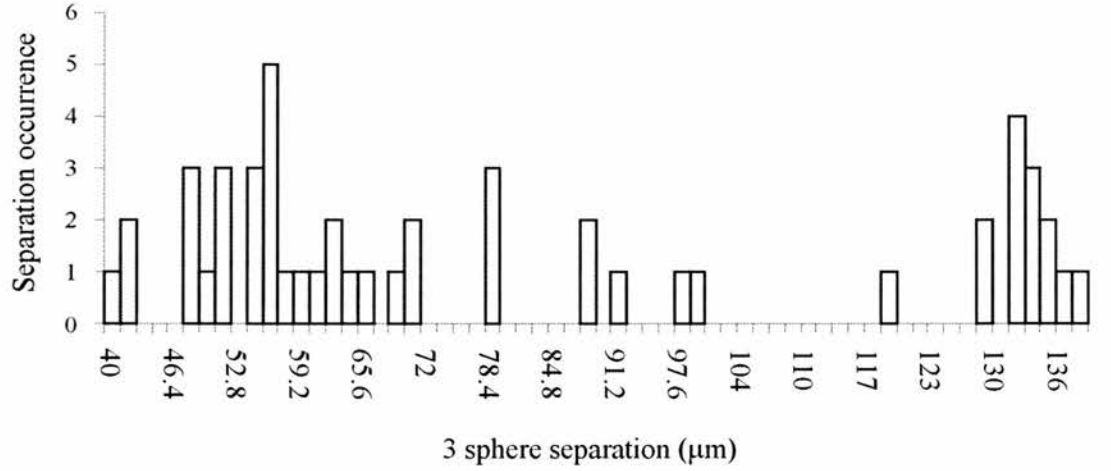

Figure 3.27. Histogram showing distribution of 1 μm particles in a three particle array. This distribution suggests a stable trapping site and a meta-stable site.

Experimental data from the dual-fibre trap suggests that in an array with multiple trapping positions, one site may display more stability than another. It is suggested at

present that due to the small beam powers used in this experiment, using 20 mW in each arm reduces the ability to observe this effect occurring. The observation of a dual-position stability trap will not be dealt with here.

3.14 Conclusion and discussion

In this work, optically bound matter has been experimentally observed using both 1064 nm and 780 nm light. Particles were confined using a horizontal counter-propagating Gaussian beam design. This unique study shows multiple particles optically coupled to each other within the light beams. The effects of changing beam and particle parameters were experimentally investigated in the system. These results were then compared to a theoretical model to gain insight into the optical trapping mechanism. The theoretical model designed by E. Wright [23] showed the scattering force to dominate over the gradient force. The model allowed comparison between the theoretical and experimental results for particle separation distances. Model predictions were deemed in reasonable agreement with experiment, taking into account experimental errors. In addition, using the assumed accuracy of the model, a realistic beam waist separation could be suggested within the observed experimental uncertainty of this quantity.

The ray optics model allows the analysis of the resulting forces on the spheres, to predict the separation of the sphere configuration within an array. To do this the model solves the acting light forces into separate components, serving as a useful evaluation. However, such differentiation between gradient and scattering forces cannot strictly be dealt like this and does not necessarily depict a true presentation of the particle dynamics. Although the gradient force is theoretically known to an accurate degree, the scattering force presented as such appears in an arbitrary form and therefore cannot serve as a quantitative comparison. For example, Roosen and Imbert [12] developed a model allowing an overall quantitative force to be calculated.

Notwithstanding the models infancy, the theory shows good correlation with experimental observation, allowing a good prediction of results. In this chapter, for

simplicity, the case of two and three particle chains have been investigated. However, this model can be readily adapted to incorporate a larger number of spheres. Furthermore, the initial model has since been adapted to allow modelling of a resultant force, allowing light forces to be quantified in a single force measurement. This study is the subject of continued collaborative work by E. Wright and here at St Andrews. This will be of importance in the study of such one- and higher- dimensional arrays of optically bound matter.

In addition, although this model predicts good approximation to the experimental system, difficulties arise with smaller sphere sizes. Such inconsistencies occur due to the initial paraxial approximation basis of the model. In the limit where particle size is comparable to wavelength, the model breaks down. For example, comparison of the model using 1 μm particles showed no agreement with experiment. Therefore, for accurate predictions with the model described in this chapter, particle size is restricted to approximately twice the laser wavelength. In contrast to this model, W. Singer et al. [14] describes a physical model breaking down at larger size regimes, favourably using particles closer in size to the wavelength. It is also interesting to note that this theoretical work found sphere diameter to play a large role in particle separation.

3.15 References

[1] A. Ashkin, "Acceleration and trapping of particles by radiation pressure", Phys Rev Lett. **24** 156 (1970)

[2] T. N. Buican, "Automated single-cell manipulation and sorting by light trapping", Appl. Optics **26** 5311 (1987)

[3] S. Tatarkova, A. E. Carruthers and K. Dholakia , "One-dimensionally optically bound arrays of microscopic particles", Phys. Rev. Lett. **89** 283901 (2002)

[4] M. M. Burns, J. Fournier and J. A. Golovchenko, "Optical binding", Phys. Rev. Lett. **63** 1233 (1989)

[5] M. M. Burns, J. Fournier, J. A. Golovchenko, "Optical matter: Crystallization and binding in intense optical fields", Science **249** 749 (1990)

[6] E. R. Dufresne et al., "Computer-generated holographic optical tweezer arrays", Rev. Sci. Instrum. **72** 1810 (2001)

[7] R. L. Eriksen, P. C. Mogensen and J. Glückstad, "Multi-beam optical tweezers generated by the generalized phase-contrast method", Opt. Lett. **27** 267 (2002)

[8] M. P. MacDonald, et al., "Creation and manipulation of three-dimensional optically trapped structures", Science **296** 1101 (2002)

[9] T. Haist, M. Schloenleber and H. J. Tiziani, "Computer-generated holograms from 3D-objects written on twisted-nematic liquid crystal displays", Opt. Comm. **140** 299 (1997); G. Sinclair et al., "Assembly of 3-dimensional structures using programmable holographic optical tweezers", Opt. Express **12** 5475 (2004)

[10] P. Korda, G. C. Spalding and D. Grier, "Evolution of a colloidal critical state in an optical pinning potential landscape", Phys. Rev. B **66** 024504 (2002)

[11] H. C. Nägerl et al., "Ion strings for quantum gates", Appl. Phys. B. **66** 603 (1998); A. M. Steane, "The ion trap quantum information processor", Appl. Phys. B **64** 623 (1998); D. F. V. James, "Quantum dynamics of cold trapped ions with application to quantum computation", Appl. Phys. B **66** 181 (1998)

[12] G. Roosen and C. Imbert, "Optical levitation by means of two horizontal laser beams: A theoretical and experimental study", Phys. Lett. **59A** 6 (1976)
[13] A. Constable et al., "Demonstration of a fibre-optical light-force trap", Opt. Lett. **18** 1867 (1993)

[14] W. Singer et al., "Self-organized array of regularly spaced microbeads in a fiber-optical trap", J. Opt. Soc. Am. B **20** 1568 (2003)

[15] P. Zemánek et al., "Optical trapping of nanoparticles and microparticles by a Gaussian standing wave", Opt. Lett. **24** 1448 (1999)

[16] D. Schrader et al., "An optical conveyor belt for single neutral atoms", Appl. Phys. B: Lasers and optics, published online 23 Nov (2001)

[17] D. G. Grier, "Optical tweezers in colloid and interface science", Curr. Opin. Colloid Interface Sci. **2** 264 (1997); J. C. Crocker and D. G. Grier, "When like charges attract: The effects of geometrical confinement on long-range colloidal interactions", Phys. Rev. Lett. **77** 1897 (1996)

[18] B. V. Derjaguin and L. Landau, "Theory of the stability of strongly charged lyophobic sols and of the adhesion of strongly charged particles in a solution of electrolytes", Acta Physicochim. URSS **14** 633 (1941); E. J. Verwey and J. Th. G. Overbeek, "Theory of the stability of lyophobic colloids", Elseiver Amsterdam (1940)

[19] R. Gussgard, T. Lindmo, I. Brevik, "Calculation of the trapping force in a strongly focussed laser beam", J. Opt. Soc. Am. B **9** 1922 (1992)

[20] S. Nemoto and H. Togo, "Axial force acting on a dielectric sphere in a focussed laser beam", Appl. Opt. **37** 6386 (1998)

[21] G. Roosen, "A theoretical and experimental study of the stable equilibrium positions of spheres levitated by two horizontal laser beams", Opt. Comm. **21** 189 (1977)

[22] D. J. Berkeland et al., "Minimization of ion micromotion in a Paul trap", J. Appl. Phys. **83** 5025 (1998)

[23] D. McGloin et al., "Optically bound microscopic particles in one dimension", Phys Rev. E **69** 021403 (2004)

[24] M. D. Feit and J. A. Fleck, "Computation of mode properties in optical fiber waveguides by a propagating beam method", Appl. Opt. **19** 1154 (1980)

[25] A. Ashkin et al.,"Observation of a single-beam gradient force optical trap for dielectric particles", Opt. Lett. **11** 288 (1986)

[26] M. Felgner, O. Muller and M. Schliwa, "Calibration of light forces in optical tweezers", Appl. Opt. **34** 977 (1995)

Chapter 4

Optical trapping with violet diode lasers

4.1 Introduction

Optical tweezers provide a powerful, non-contact method of manipulating microscopic particles. An optical tweezers is a tightly focused laser beam used to capture and direct particles [1]. In the Mie regime, where particles are larger than the trapping wavelength, $\sim \lambda/10$, momentum exchange occurs on refraction of the light through the particle. This forms an intensity gradient near the beam focus that gives rise to a gradient force confining the particle in three dimensions. Typically, the technology can readily move objects in the 1-10 micron region, though trapping can occur down to 25 nm [2]. The focussed spot size of a laser can be reduced to a diffraction-limited spot, determined by the wavelength of light used. Due to this constraint, localising particles in a small region can prove difficult. The use of shorter wavelengths of light is an exciting potential route to allow much smaller trap volumes to be realized. Early optical tweezing makes use of Argon ion lasers (514.5 nm) to trap dielectric particles, viruses and bacteria [2]. This potentially allows a smaller trap volume to be obtained allowing a greater localisation of particles, reducing the diffusion region within the volume of the optical trap.

The use of lasers as tools to cut chromosomes [3] or transfect cells [4,5] requires a degree of accuracy, which has previously been accomplished using IR lasers. However, short wavelengths offer small spot sizes, which allow a localised region of damage to the biological tissue to occur. The use of shorter wavelengths can also be of use in particle tracking studies investigating diffusion of matter within an optical trap.

The development of InGaN semiconductor materials has led to the commercial availability of continuous-wave violet laser-diodes with practical lifetimes of > 5000 hours. Recently, frequency doubled vertical external cavity surface emitting lasers (VECSELs) operating at 488 nm have appeared on the market [6], giving a compact blue laser with high beam quality. In May 2003, violet laser diodes, that had been microlensed to achieve a circular output beam, became commercially available [7]. These lasers provide excellent beam quality in a compact and convenient packet. They are discussed further in chapter 5. Such devices are finding use in a range of studies including spectroscopy [8], flow cytometry studies [9], and confocal imaging [10]. However, their use is in its infancy. No reports have been made of their use in optical micromanipulation. These can be placed into extended cavities in order to force them to operate on a single longitudinal mode with a narrow linewidth [11].

Optical techniques provide a powerful means to probe a wide range of biological phenomena. For example, chromosomes allow insight into genetics and protein-protein interactions to investigate intercellular processes. Optical tweezers are emerging as important tools for use in molecular motors. This allows studies into the elastic properties of biological matter, for example red blood cells [e.g.12] and molecular mechanisms [e.g.13]. In addition, research has progressed into bio-spectroscopy using both non-specific and specific biological tags. This technique provides high-resolution studies, allowing observation of genes, enzymes and proteins, for example. Many biologically important stains absorb light in the blue-violet spectral region. This has led to the use of violet diode lasers as an illumination source in flow cytometry [9]. DAPI (4'-6-Diamidino-2-phenylindole) is one such stain, which non-specifically binds to all chromosomes, intercalating with their DNA. Other biological tags, such as green fluorescent protein (GFP) and its derivatives such as cyan fluorescent protein (CFP) [4,5],

allow protein specific identification with enormous flexibility. In general, these fluorescent tags can be engineered, at the gene level, so that they are fused to a particular protein of interest. The resulting DNA construct can be transfected into living cells, where the gene of the protein of interest expresses as a GFP/CFP tagged protein. This gives a non-invasive marker, which can be exploited by new laser technology, to observe and elucidate areas of cell and molecular biology, observing protein-protein interactions, cell lineage tracing, and gene expression.

This chapter describes the use of compact, semiconductor laser systems operating at 410 nm, 413 nm and 488 nm in optical tweezing and for fluorescence excitation in optical micromanipulation systems. New studies for tweezing at these short wavelengths are shown, demonstrating the potential for a multi-functional capability. The flexibility to combine observation of biological samples with particle manipulation in an integrated optical system is shown.

4.2 Trapping efficiency

Optical tweezing uses a tightly focused laser beam to capture and manipulate particles in three dimensions. The particle is drawn into the region of highest local intensity, producing an intensity-gradient or dipole trap near the beam focus, previously shown in figure 2.3. A truly three-dimensional trap (optical tweezers) [1] results when the gradient force exceeds the drag, scattering and gravitational forces acting on the particle as well as its thermal (Brownian) motion. A quantity Q is used to describe the quality of the beams efficiency to optically confine a particle in three-dimensions, known as the trapping efficiency.

In order to explore the optical trap fully, these trapping forces and the trapping efficiency must firstly be quantified using the short wavelength sources discussed here. The efficiency of an optical trap is usually quantified by a dimensionless parameter Q, which corresponds to its lateral trapping efficiency [14,15]. When considering the lateral trapping, Stokes drag must be taken into consideration. Here, the scattering, gravitational and Brownian motion forces are negligible. Brownian motion is a thermal force caused

by collisions from molecules in the surrounding medium impacting the confined larger particle. The thermal force is inversely proportional to the sphere's diameter [16]. Smaller sphere diameters will therefore suffer a larger diffusion force.

Optical trapping perpendicular to the beam propagation direction relies on the quality and power of the laser source used to manipulate objects. The drag force in an optical trap is the object's resistance to motion through the suspending medium. Q is therefore defined at the equilibrium position, where the trapped object only just stays in the trap. At this point the lateral trapping (gradient) force, shown below in equation 4.1, is equal to the Stokes drag, shown below in equation 4.2 [14].

$$F_{grad} = \frac{Qn_m P}{c} \qquad [4.1]$$

$$F_{stoke} = 3\pi\eta dv \qquad [4.2]$$

where n_m is the refractive index of the medium surrounding the trapped particle and η the viscosity of the suspending medium, c is the *in vacuo* speed of light, P is the incident tweezing power at the sample, d is the particle diameter and v the maximum lateral velocity at which the particle remains trapped. It is therefore possible to calculate Q from measuring this lateral velocity. Since Q is a measure of trap efficiency, a Q value of 2 corresponds to a complete transfer of momentum from the photons within the light beam to the particle. It must be stressed that Q values are complex entities in some respects in optical tweezers, as although dimensionless parameters, they do depend upon the degree of light focusing and aberrations (e.g. spherical) present in the optical trapping system.

The most commonly used sources in optical tweezing are red and near infra red (IR) lasers due to their excellent beam quality and technological maturity. These lasers are ideally suited to biological applications as a consequence of their low absorption in water and biological tissue. This highly beneficial property allows biological material to be manipulated, whilst minimizing the potential for damage. Laser sources at 532 nm and at argon ion wavelengths (488 nm) have also been used effectively for optical tweezing, combining negligible water absorption with a small diffraction limited spot [e.g.15]. Unfortunately, at shorter wavelengths, in the violet and blue spectral region, an increase in tissue absorption occurs, which can lead to tissue damage. It is, therefore, necessary to

weigh the disadvantages of the increased risk of tissue damage against the advantages of a reduced trapping volume in appropriate situations.

4.3 Optical trapping volume

Optical tweezers have been exploited for biological applications since being developed by Ashkin, where tobacco viruses were confined [2]. Large spot sizes are obtained from the longer IR and red wavelengths most commonly used. A large volume results, for particles to diffuse within. The particles' strong Brownian motion contributes to movement within the optical trap. Laser devices of a shorter wavelength, such as those discussed in this chapter, allow comparatively smaller trapping volumes to be formed, allowing further confinement. This further reduces the particle travel due to diffusion.

A diffraction-limited spot focuses to a minimum spot radius of $\lambda/2$. The shorter wavelength of violet laser sources therefore permits a smaller focused spot size to be obtained. The wavelength of light used for optical trapping is crucial. In the case where the particle is much smaller (factor of 20) than the wavelength, the particle is in the Rayleigh regime where it is considered as a small induced dipole that aligns itself with the light field, described above. If the particle size is larger than the wavelength of the trapping light, it is said to be in the Mie regime, where a geometrical (ray) optics approach is appropriate.

Within this regime, Mie scattering predominates over Rayleigh scattering, and the dipole of the trapped particle can be neglected. However, if the particle is much smaller than the focused spot size, then Rayleigh scattering predominates. Therefore, governing forces due to this scattering has a $1/\lambda^4$ dependency (equation 2.8). Moreover, in this limit, the depth of the trapping potential from the gradient force shrinks rapidly (with the volume of the particle), and tweezing is correspondingly weak. The short wavelength of violet lasers enables particles as small as 200 nm to be trapped but now within the intermediate regime. A significantly smaller trap volume is also a potential advantage that results from the tighter focus that is possible with the violet light. The approximate theoretical trap

volume is taken here as a cylinder centred on the beam waist along the propagation axis, with a height of two beam waists above and below this position, figure 4.1.

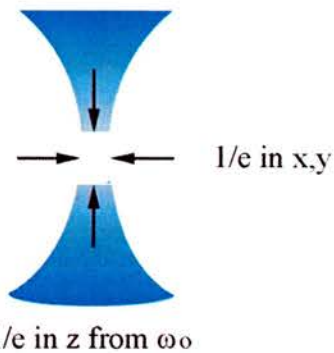

Figure 4.1. The trap volume of the focussed spot is defined by the region around the waist, a diameter across and a diameter above and below the focal plane.

The trap volume (based on [17]) for a 410 nm laser, assumes a diffraction limit spot, $\lambda/2$, is $1.1\text{x}10^{-19}$ m^3, whereas an IR laser at 1064 nm gives a trapping volume of $1.9\text{x}10^{-18}$ m^3 (over 17 times larger) The smaller volume of the violet laser trap enables higher degree of localization of the trapped particle. Importantly, this gives the possibility of singly populating the trap with far smaller particles than would be possible within a larger trap volume. Sub-micron particles and nano-particles have instigated renewed interest to encompass potential biophysics and imaging applications, but relatively little attention has been focused on them from optical trapping research, where the majority of studies focus on micron sized (or greater) particles. In a violet laser trap, sub-micron sized particles can therefore be individually confined, constrained within a space comparable with its own size, and manipulated in a violet laser diode trap. This may not be possible with a red or near infrared source.

4.4 Experimental design

4.4.1 Trapping particles with optical tweezers

Three commercially available laser systems in the blue-violet spectral region are assessed in this work. The first system considered was an external cavity laser diode (ECDL) from Toptica GmbH (DL100) running in the violet (although for this application an external

cavity is not a necessity) providing 14 mW of output power at 410 nm. The second laser system was a free running microlensed violet laser diode from Blue Sky Research, which provided a circular output beam of 25 mW at 413 nm. The third source was a frequency doubled vertical extended cavity surface emitting laser (VECSEL) from Novalux Inc. that provided a maximum output power of 5 mW at 488 nm. These lasers are compared with a frequency doubled Nd:YVO_4 532 nm solid state laser (SSL) [15] and a Nd:YVO_4 1064 nm SSL [14] data from literature.

Both the VECSEL and the microlensed laser diode had circular beam profiles with good beam quality M^2, and thus required no beam-shaping. The method for measuring M^2 is described in section 5.5. These laser sources provide M^2 values of less than 1.2 in both planes for the VECSEL and M_x^2 of 1.5 and M_y^2 of 1.3, for the microlensed laser diode. The diode laser used for our ECDL system exhibited poorer beam quality characteristics with measured M^2 values of 2.3 and 1.7 in the two planes. The elliptical output was beam shaped through the use of two cylindrical lenses (f_x = 10 mm and f_x = 40 mm). Each laser was used as an optical tweezing source in the basic design, shown in figure 4.2, and the efficiency of trapping determined.

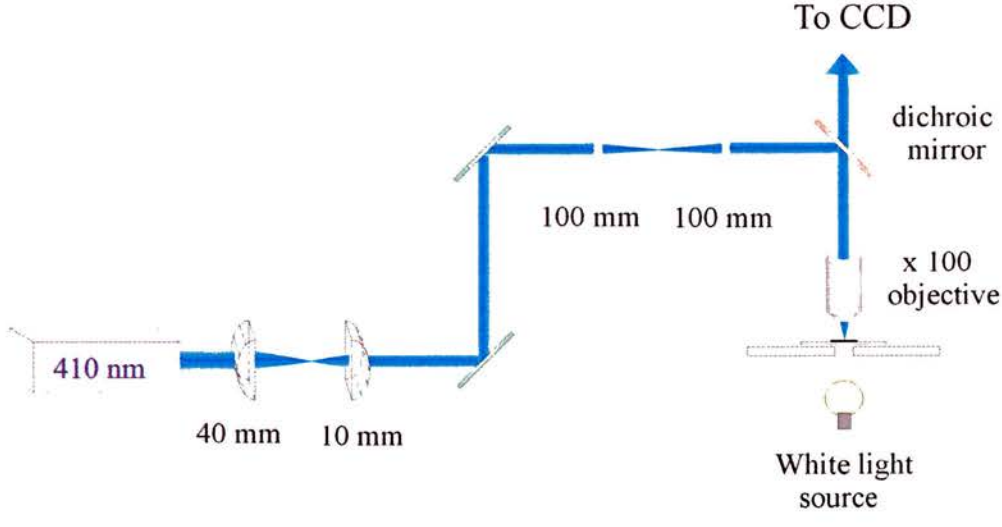

Figure 4.2. Experimental optical tweezers set up using a violet external cavity diode laser source. The beam is initially shaped using two cylindrical lenses and focused through a microscope objective in the sample plane.

The beam was expanded and collimated using the first telescope. A lens relay imaged the beam onto the back of the microscope objective (Newport, x100, NA 1.25) creating a conjugate plane for beam steering. The sample was illuminated from below using a white light source and scattering from the sample allowed observation via the CCD camera. The sample cell was created from a microscope slide and cover-slip separated by an 80 μm thick spacer. Colloidal particles (0.2–10 μm in diameter, refractive index of the silica spheres = 1.43 (at 589 nm, Bangs Laboratories), refractive index of the polymer spheres = 1.59 (at 589 nm, Duke Scientific Corporation)) were deposited within the resulting 20 μl well, which led to a controlled sample volume.

The microscope objective was designed for longer wavelength visible light, and therefore, exhibited a low transmission of violet and blue wavelengths. The ECDL beam provided an available trapping power of 1.3 mW at the sample plane with an approximate radius beam waist of 250 nm. The VECSEL provided 0.6 mW of power with an approximate radius beam waist of 600 nm, due to it having a smaller beam size on the back surface of the objective. The microlensed laser diode provided a power of 3.5 mW focused to an approximate radius of 200 nm. The poor system efficiency caused huge power loss, due to lossy optics through the tweezer system. For this reason, the 488 nm source was not optimally expanded to fill the objective, to avoid further reduction in the tweezing power.

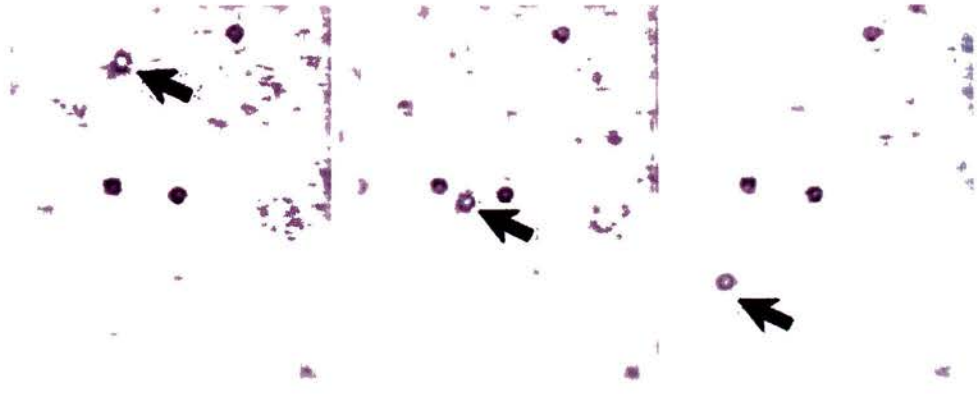

Figure 4.3. CCD camera images show the manipulation of a 0.4 μm silica sphere using the violet external cavity diode laser at 410 nm with 1.3 mW of tweezing power.

Optical tweezing with silica spheres ranging from 0.4 μm to 10 μm in diameter was achieved. Particles of 0.4 μm in size are shown being manipulated, using the 410 nm ECDL in figure 4.3. Tweezing forces for this sphere size were reduced, due to the strong Brownian motion of the polymer spheres and poor beam quality of the ECDL. The low available tweezing power of the 488 nm VECSEL, combined with its larger beam waist, led to its inability to tweeze spheres of this size. By contrast, the violet microlensed laser diode allowed tweezing of 400 nm silica particles and 300 nm green fluorescent polymer particles. The optical tweezer also visibly affected fluorescent polymer particles with a 200 nm diameter. However, the strong thermal Brownian motion made it arduous to move these particles further than approximately 5 μm.

4.4.2 Trapping efficiency

The lateral trapping efficiencies of the 488 nm VECSEL, 410 nm ECDL and 413 nm microlensed laser diode were measured. One arm on the sample stage was fitted with a micron-step actuator operated by a motion controller (Newport, ESP300). This allowed the sample to be accurately and smoothly moved a known distance, at a constant controlled velocity. The light focus position of the optical tweezers was kept constant, and the sample stage moved with respect to it. For each measurement a single particle was tweezed and lifted in the z-axis, above the plane of the freely moving particles, close to the top of the sample. The distance over which particles were moved was kept constant. The sample stage velocity was gradually increased until the particle could not stay within the optical tweezer. At this point, the stage velocity was gradually increased and decreased using different particles within the sample. This allowed the average velocity of a particle to be determined over 10 readings. The process was repeated for each laser source, using a range of laser powers for each particle size between 0.4 μm and 5 μm in diameter.

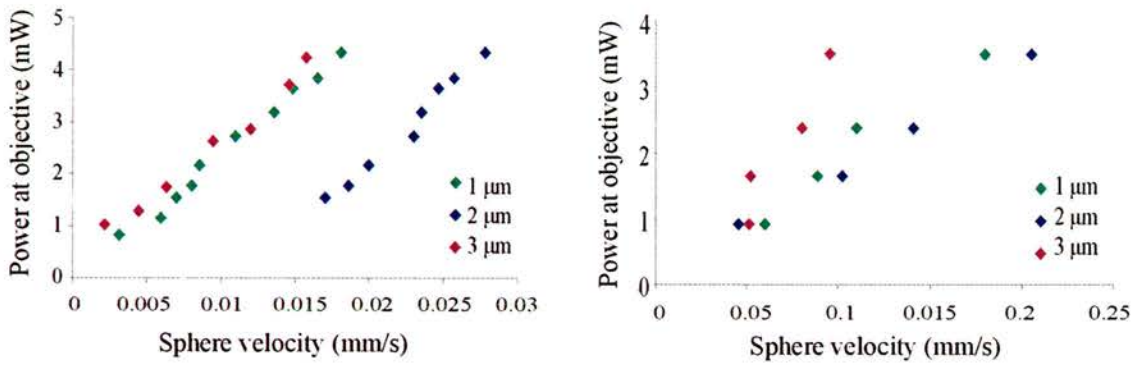

Figure 4.4. Sphere velocities, for particles of 1 μm, 2 μm and 3 μm in diameter, at different powers using a (a) standard violet diode laser and (b) violet microlensed diode laser.

Figures 4.4(a) and 4.4(b) show sphere velocities results for a range of different silica sphere diameters for the standard and microlensed violet diode lasers. The tweezing power of the 488 nm VECSEL was not varied due to its low transmission through the optical setup. These sphere velocity results are directly related to the optical trapping efficiencies through equating equations 4.1 and 4.2, shown in table 4.1. All Q values were obtained with the tweezed particle raised above the sample plane of diffusing particles, z-trapping close to the top of the sample surface. For 0.4 micron spheres this z-trapping was weak. These trapping efficiencies are compared to similar results obtained by O'Neill and Padgett, using a 50 mW 532 nm frequency doubled Nd:YVO_4 SSL with a 100x objective [15] and Felgner et al. using a 95 mW 1064 nm Nd:YVO_4 SSL [14] with a 1.3 NA 100x objective.

Sphere ϕ (μm)	Q values				
	ECDL	VECSEL	Microlensed laser diode	Frequency-doubled SSL[a]	SSL[b]
0. 4	-	-	0.012 ± 0.001	-	-
1	0.034 ± 0.003	0.039 ± 0.004	0.25 ± 0.03	0.035 ± 0.001	0.085
2	0.12 ± 0.01	0.12 ± 0.01	0.29 ± 0.03	0.068 ± 0.002	0.14
3	0.09 ± 0.01	0.11 ± 0.01	0.29 ± 0.03	-	0.21
5	0.024 ± 0.002	0.16 ± 0.01	0.09 ± 0.01	0.121 ± 0.006	0.33
10	-	0.22 ± 0.02	-	-	-

[a] From Opt. Comm 193, 45-50 (2001)

[b] From Appl. Opt. 34, 977-982 (1995)

Table 4.1. The trapping efficiencies (Q values) of the tweezer set-up for different sphere diameters ϕ, were taken at different power with the three laser systems, and are compared to two sets of published data presented by other groups.

This data, table 4.1, compares the short wavelength optical tweezing presented here with that reported in the literature. The demonstrated lateral Q values are very comparable with longer wavelength laser sources. Such tweezing efficiencies using longer wavelengths are as shown in table 4.1 with a solid-state laser 1064 nm and frequency-doubled solid-state laser 532 nm. Trapping, using the microlensed laser diode source, provided far more efficient and stronger trapping than the other two systems due to its circularity, as expected. The Q values, shown for this laser, are favourable compared with those found in the literature for trapping 1–3 μm spheres. However, the 10 μm spheres do not compare favourably, as tweezing could not be achieved. The 5 μm spheres also compare poorly, which at 25 times larger than the focal spot are reaching the size limit of particles which the system is able to manipulate. This laser had a circular focal spot, as opposed to the elliptical one exhibited by the ECDL and M^2 values much closer to one. Hence, it is likely that beam asymmetry issues are causing the reduced trapping efficiency of the ECDL system. The VECSEL is much closer to the microlensed laser

diode in terms of beam quality. It is also shown to provide a greater trapping efficiency than the ECDL. However, it is still lower in efficiency than the microlensed diode system. All of the systems compared well to the frequency doubled SSL system. However, only the microlensed diode tweezer system compared favourably with the fundamental SSL.

In measuring the lateral trapping efficiency, it is reasonable to assume that the gravitational forces are negligible. Since gravity is working perpendicular to the trapping, only the Stokes drag needs to be considered. However, in order to achieve strong axial, or z-trapping, it is necessary for the trapping force to overcome the gravitational force. The low tweezing power available at the focal region, particularly for the VECSEL and ECDL sources, meant that this was not possible for several of the sphere sizes. Thus the results must be weighted appropriately (table 4.2). This accounts for line deviation for some sphere sizes, particularly for the VECSEL source. It can also be seen from table 4.2 that in some cases gravitational force is greater or comparable with the tweezing force.

Sphere ϕ (μm)	$F_{gravity}$ (pN)	F_{stokes} 488 nm (pN)	F_{stokes} 410 nm (pN)	F_{stokes} 413 nm (pN)
0.4	0.004	-	-	0.179
1	0.010	0.103	0.170	1.693
2	0.123	0.301	0.602	4.460
3	0.272	0.278	0.447	2.711
5	1.259	0.426	0.117	0.688
10	10.070	0.570	-	-

Table 4.2. Optical trapping forces using 488 nm VECSEL, 410 nm standard diode laser and 413 nm microlensed diode laser are shown compared to the gravitational force.

For all the lasers, the gravitational force on 1 μm spheres was lower than the trapping force. At 2 μm, the ECDL trapping force was comparable to the gravitational force on the particle, which with larger particles exceeded the trapping force. The gravitational force

exerted on 3 μm spheres was an order of magnitude larger than the trapping force of the VECSEL. Again for larger particle sizes, the gravitational force increased, while the trapping force decreased. The trapping force induced by the microlensed laser is shown to exceed the gravitational force for particles up to 3 μm in diameter. For larger particles, the gravitational force is also increases. This was observed experimentally, being difficult to lift larger particles above the sample plane. The microlensed laser system readily exhibited z-trapping, while the other source exhibited weak z-trapping. The microlensed diode lasers ability to localise particles more effectively than a standard diode device is due to its good beam quality. Circularised output beams therefore provide improved trapping efficiencies. The lower wavelength of the violet devices also provides a smaller trapping volume allowing small particles to be more easily manipulated than using IR lasers. As an aside, it is likely that more stable z-trapping could be obtained from a tweezer set-up with an inverted trap beam. In the inverted geometry, gravity assists the axial tweezing forces to help confine the particle, as it is moved in the z-direction.

4.5 Manipulation and fluorescence of biological structures

4.5.1 Introduction

Biological dyes allow the differentiation and identification of particular matter in a group of biological species. In addition, they provide contrast between areas of tissue. In this section, two biological tags are discussed. Many different dyes, which fluoresce in different areas of the spectrum are available. However, DAPI [18], a non-specific dye, is used here to indiscriminately attach to the matter with which it comes into contact, with a wide absorption in the violet. In addition, a gene-specific dye, GFP [19] that has a wide absorption in the blue, is also used, allowing the tagging of a chosen protein.

It is therefore possible to use the lasers discussed in the previous section to excite fluorescence in these biological markers. The ECDL was employed to excite fluorescence in both GFP, which was fused with amyloid β-peptide binding alcohol dehydrogenase (ABAD), and DAPI stained Chinese hamster ovarian (CHO) chromosomes. This laser

was also utilized to induce fluorescence in, and simultaneously tweeze, blue fluorescent polymer spheres. L. Patterson prepared the biological samples used in this section.

4.5.2 Biological marking

DAPI (4'-6-Diamidino-2-phenylindole) is a non-specific fluorescent dye widely used for staining biological matter. It is particularly useful as a general stain, here, for chromosomes in a non-discriminate manner. The dye molecules insert into the major axes of the DNA, causing the matter to absorb and fluoresce in the blue/violet spectral region. However, it may be necessary to study nanoscopic particles, cell internal structure or protein-protein interactions and in these cases a different type of biological tag is required.

Every function in the living cell depends on proteins. The specific function comes from the way the protein folds into its 3D structure. Proteins can control cell structure, transportation motion and locomotion, signalling, receptors, protection and be catalysts to biological reactions. It is therefore of huge advantage to our understanding of cells to monitor intercellular protein interactions and processes, to gain insight into its function. To do this effectively, it is important to be able to track and monitor individual proteins without a risk of cross contamination between protein species from a non-specific biological stain.

Wild type GFP is a naturally found protein extracted from a jellyfish, Aequoria Victoria, absorbing at 395 nm and emitting at 508 nm [19]. Genetic modification of this protein has allowed different fluorescent protein to be produced, figure 4.5(a) and 4.5(b). In the experiment described here, enhanced-GFP absorbing at 488 nm and emitting at 509 nm is used. The beauty of this protein-specific tagging is its ability to target the protein of choice allowing identification, tracking and ultimately providing selective manipulation of matter. The protein of study is isolated before being joined with the fluorescent protein. The modified matter is then re-introduced to its cell environment to regenerate, expressing this FP gene containing the selected protein.

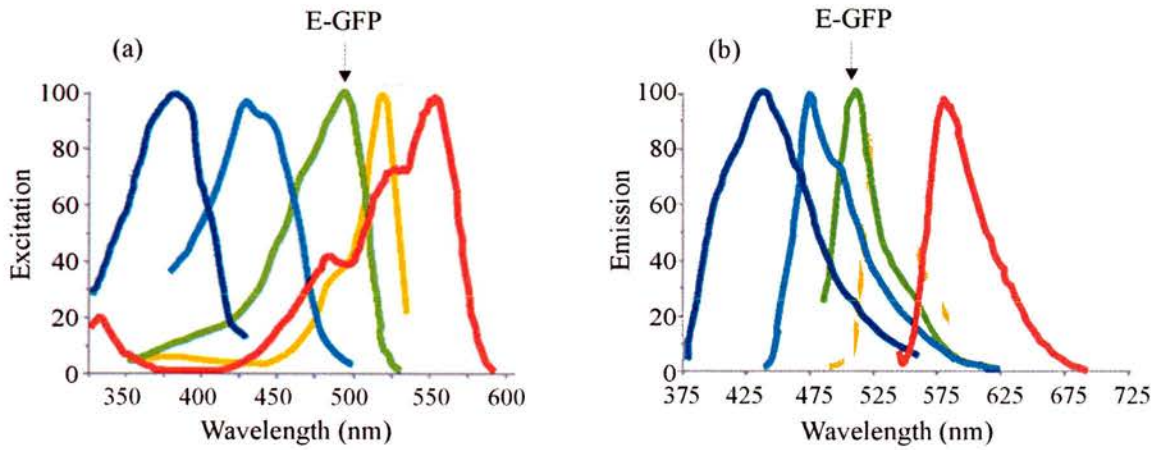

Figure 4.5. Different fluorescent protein mutants are shown. (a) The protein is excited in a narrow band of wavelengths and (b) emits at a slightly higher wavelength.

4.5.3 Chromosome manipulation

In order to stain and prepare the chromosomes for tweezing, CHO cells were treated with a chemical, which prevented the cell from dividing. This enables the chromosomes to be harvested. The cells were burst open by passing them through a needle and the debris was removed by washing. This left the chromosomes behind, which can then be stored in a fixative solution containing one part acetic acid and three parts methanol. This solution is added at the stage of the cell cycle chosen to observe, freezing the cells at that point in time, thus acting as a cell preservative.

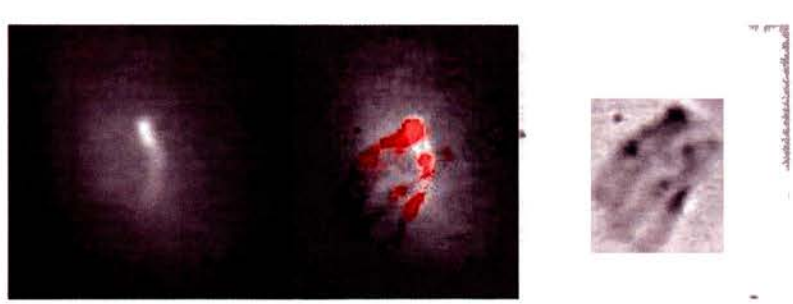

Figure 4.6. Comparison between two chromosomes under violet laser illumination, first picture and under chromosome under white light illumination, last picture. The central picture shows the first picture overlaid by a red version of the last picture to show that the fluorescence is coming in part from one chromosome and in part from the other.

For tweezing, the chromosomes were re-suspended in phosphate buffered saline (PBS), a salt solution in which the chromosomes are at equilibrium. DAPI was then added, one part DAPI for twenty parts PBS. Chromosomes are shown in figure 4.6 being illuminated by both violet and white light sources.

The set up was modified from figure 4.2 to include an inverted tweezer from beneath the sample cell using a 50 mW 1064 nm SSL laser. Incident illumination from the violet ECDL from above, previously used as a tweezer, excited fluorescence in the DAPI stained chromosomes. Thus, the violet ECDL could be used for illumination of a particle optically trapped by the infrared SSL. In this geometry, we retain the attributes of tight focusing of the violet light that allow a selective excitation within the biological specimen of interest. A chromosome is shown in figure 4.7 being guided in the z-axis along the beam propagation direction. This can be seen with respect to the group of chromosomes to the right of the trapped chromosome. In this instance, the violet laser was used for fluorescence and not for tweezing, using 1.3 mW of 410 nm light. Very low powers could be used, reducing the risk of damage to the tissue.

Figure 4.7. Guiding of one chromosome compared to a group of chromosomes.

4.5.4 Biological spectroscopy with GFP

A gene of interest can be linked to a reporter gene, such as GFP, which provides important information about the location of protein expression within the cell. ABAD is a protein involved in Alzheimer's disease [20]. The amyloid β-peptide is a precursor protein, connected with the disease, that binds itself to the enzyme alcohol dehydrogenase

for introduction into the cell. Using DNA manipulation, ABAD was ligated with GFP to produce an ABAD-GFP DNA construct.

This DNA construct was then used to transfect human neuroblastoma cells, brain cells, which were subsequently illuminated and fluoresced using the violet ECDL. The ABAD-GFP fusion protein was expressed in the cell's mitochondria. With conventional fluorescence microscopy, fluorescence occurs wherever the ABAD-GFP is expressed, as shown in figure 4.8.

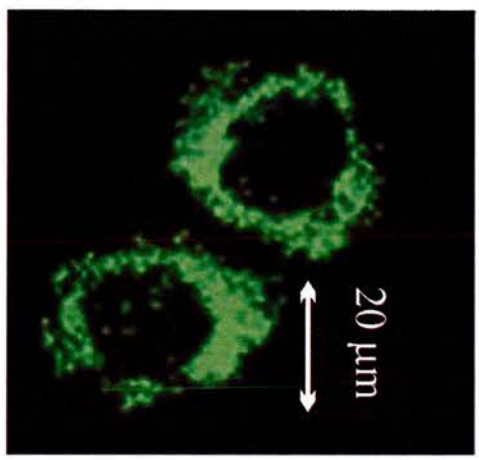

Figure 4.8. A human neuron (neuroblastoma) cell viewed under a conventional fluorescence microscope, exhibiting fluorescence across the entire cell.

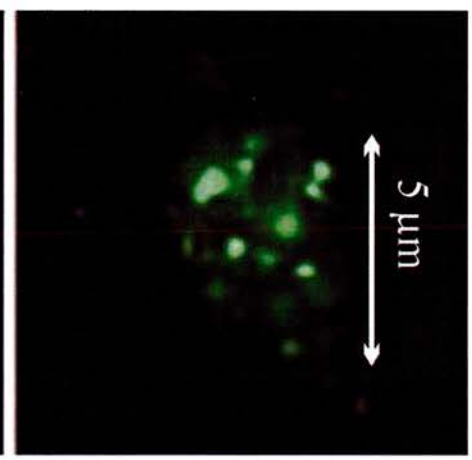

Figure 4.9. A section of a human neuron (neuroblastoma) cell containing GFP viewed with a violet diode laser fluorescence illuminator and a x100 microscope objective, exhibiting fluorescence of only a section of the cell.

The use of the violet laser, as opposed to excitation with an incoherent light source, allows a very specific area, within the cell, to be examined without risk of bleaching the surrounding areas. This is shown in figure 4.9. However, the violet laser wavelength at 410 nm is significantly far from the peak of the absorption of the GFP at 488 nm. The VECSEL laser is a more suitable alternative in this instance. Blue diode lasers may be used with either cyan fluorescent protein or blue fluorescent protein, with absorption peaks at 440 and 405 nm respectively. This would potentially enable individual proteins to be identified and possibly manipulated within the cell itself, using the increased functionality of this set-up.

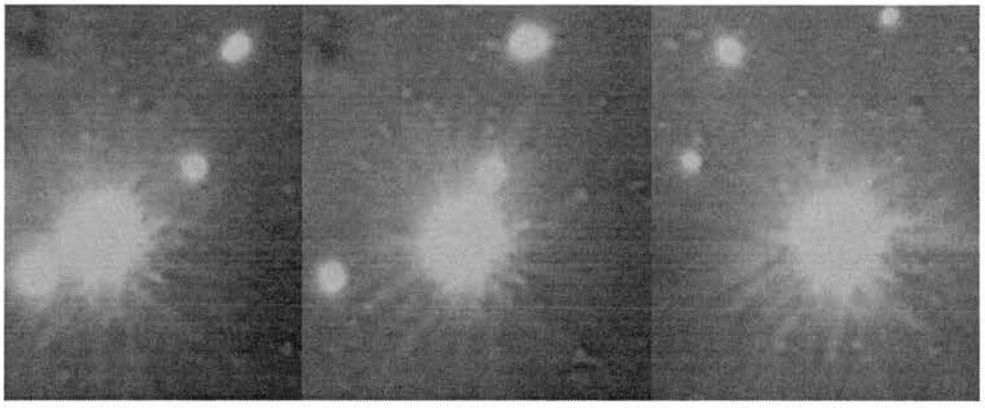

Figure 4.10. Simultaneous fluorescence and manipulation of blue fluorescent 1 μm polymer spheres sample stage is being moved with respect to the optical tweezer.

In this next experiment, blue fluorescent, 1 μm diameter polymer spheres were manipulated by the violet ECDL tweezer system. Figure 4.10 demonstrates this simultaneous tweezing and fluorescence of particles. Here, the sample stage is moved with respect to the laser. The tweezed object is therefore the bright central particle in each frame of the trapping sequence. Although this experiment worked well with fluorescent spheres, it is possible that the increase in power necessary to manipulate, rather than merely excite fluorescence, within the trapped particle, will lead to this technique being unsuitable for biological samples, due to the increased risk of tissue damage.

4.6 Conclusion and discussion

In this chapter, violet diode lasers have been used for optical tweezing and imaging. Optical trapping has been shown with the shortest wavelengths yet used with new violet laser technology. Trap efficiencies for a range of sources in the blue and violet region were investigated. For each source, Q values were obtained using silica particles ranging in diameter from 0.4 μm to 10 μm, at a range of powers. Each Q value was determined using results from an average of over 10 particles. Very strong lateral trapping and high Q values were obtained for the microlensed violet diode laser for particles in the 1–3 μm range. The blue VCSEL offered an excellent beam quality, however, produced poor trapping efficiencies due to the low available tweezing power. In contract, the violet

standard diode provided sufficient tweezing power with a poor beam quality. This device therefore produced weak trapping efficiencies. The microlensed device due to the combination of power and good beam quality improved upon the trapping efficiencies obtained from commonly used infrared wavelengths. Particles down to 300 nm were also readily manipulated using this system. The shorter wavelength allows a reduced optical trap volume allowing particle localisation within a considerably smaller region of space. This can potentially assist with particle tracking experiments to reduce the diffusion area within an optical trap.

A multi-functional system, used to manipulate and image particles and biological matter in a single set-up, has been demonstrated. The set-up combines a violet diode with an IR SSL optical tweezer. Within this set-up, laser-induced fluorescence and guiding of DAPI stained chromosomes has been observed, demonstrating a compact cytometry system. The fluorescence of GFP bound proteins within a human neuroblastoma cell has also been demonstrated, using a violet ECDL source. This opens up the possibility of observing protein and gene motion through living cells in a compact diode laser based apparatus. The development of multifunctional systems, such as the system demonstrated here, has major biological implications in progressing the development of cytometry systems, along with our fundamental understanding of cell and molecular biology.

4.7 References

[1] A. Ashkin et al., "Observation of a single-beam gradient force optical trap for dielectric particles", Opt. Lett. **11** 288 (1986)

[2] A. Ashkin, J. M. Dziedzic, "Optical trapping and manipulation of viruses and bacteria", Science **235** 1517 (1987)

[3] X. Lui et al., "Preparation of single rice chromosome for construction of a DNA library using a laser microbeam trap", J. Biotech. **109** 217 (2004)

[4] J. Lippincott-Schwartz and G. H. Patterson, "Development and use of fluorescent protein markers in living cells", Science **300** 87 (2003)

[5] G. H. Patterson and J. Lippincott-Schwartz, "A photoactivatable GFP for selective photolabeling of proteins and cells", Science **297** 1873 (2002)

[6] H. A. Jones-Bey, "Vertical cavity lasers", Laser Focus World **37** 60 (2001)

[7] http://www.blueskyresearch.com/pdfs/chromalase/ChromaLase405-081203.pdf, Blue Sky Research

[8] H. Leinen et al., "GaN blue diode lasers: a spectroscopist's view", Appl. Phys. B-Lasers O. **70** 567 (2000)
[9] H. M. Shapiro and N. G. Perlmutter, "Violet diodes as light sources for cytometry", Cytometry **44** 133 (2001).

[10] J. M. Girkin et al., "Confocal microscopy using an InGaN violet laser diode at 406 nm", Opt. Express **7** 336 (2000)

[11] R. S. Conroy et al., "Characterisation of an extended cavity violet diode laser", Opt. Comm. **175** 185 (2000).

[12] R. R. Huruta et al., "Mechanical properties of stored red blood cells using optical tweezers", Blood 2975 (2003)

[13] H. Guo et al., "Mechanical properties of breast cancer cell membrane studied with optical tweezers", Chin. Phys. Lett. **21** 2543 (2004)

[14] M. Felgner, O. Muller and M. Schliwa, "Calibration of light forces in optical tweezers", Appl. Opt. **34** 977 (1995)

[15] A. T. O'Neil and M. J. Padgett, "Axial and lateral trapping efficiency of Laguerre-Gaussian modes in inverted optical tweezers", Opt. Comm. **193** 45 (2001)

[16] A. Rohrbach and E. H. K. Stelzer, "Trapping forces, force constants, and potential depths for dielectric spheres in the presence of spherical aberrations", Appl. Opt. **41** 2494 (2002)

[17] A. Rohrbach and E. H. K. Stelzer, "Three-dimensional position detection of optically trapped dielectric particles", J. Appl. Phys. **91** 5474 (2002)

[18] E. Trotta and M. Paci, "Solution structure of DAPI selectively bound in the minor groove of a DNA T-T mismatch-containing site: NMR and molecular dynamics studies", Nucleic Acids Res. **26** 4706 (1998)

[19] F. Yang, L. G. Moss, G. N. Phillips, "The molecular structure of green fluorescent protein", http://www-bioc.rice.edu/Bioch/Phillips/Papers/gfpbio.html

[20] J. W. Lustbader et al., "ABAD directly links Abeta to mitochondrial toxicity in Alzheimer's disease", Science **304** 448 (2004)

Chapter 5

Violet and red microlensed diode lasers for spectroscopy

5.1 Introduction

A critical requirement for atomic and molecular laser spectroscopy is a tunable narrow linewidth laser source, used to probe and distinguish the atomic transitions of interest. Narrow linewidths place stringent constraints on the laser systems used, and this has led to significant activity to achieve this. Diode lasers have emerged as excellent tools in atomic and spectroscopic applications [1] although typically their off-the-shelf features need to be carefully altered to allow them to be used as spectroscopic tools.

Since the mid 1980's, red and IR diode devices have undergone dramatic changes. The constant evolution and fabrication of these devices has considerably improved both spectral and spatial beam characteristics. Importantly, for spectroscopic applications, red and IR devices have been developed. Therefore, a stable output can be provided, with a narrow linewidth, utilising an extended cavity. The compact design of an extended cavity exploits the diode laser's susceptibility to optical feedback. This allows a wavelength selective output with the incorporation of a diffraction grating.

Diode lasers normally emit an elliptical output beam with notoriously poor spectral and spatial quality. However, good beam quality is essential for many experiments in atomic and laser spectroscopy, for example, laser cooling and trapping [2,3,4]. Additionally, high quality outputs from external cavity diode lasers are required for pumping optical parametric oscillators or for tapered amplifier systems. Achieving such beam quality adds a degree of complexity and loss to the optical setup. Ideally, that might be obviated. Extended cavity diode lasers are typically beam shaped, using either anamorphic prisms, single mode fibre coupling or cylindrical lenses. Therefore, it would be advantageous, in many instances, to have a diode laser in external cavity that directly emits a high quality circular beam. That especially applies to wavelength regions, where the base laser diode power itself is not particularly high [5]. The integration of a cylindrical lens has developed these devices significantly, improving the diode output. The micron-sized lens is placed tens of microns away from the output facet thus circularising the beam. Due to the feedback from the lens, the diode is made to run single mode. Current tuning of the diode laser can additionally produce a long tuning range.

The continual renovation of diode devices has enabled major advances in galium nitride GaN materials over a considerably shorter time scale. This allows access to, and fast development of, the blue and violet spectral region. In 1995, Nakamura successfully produced a working reproducible GaN device. Force of demand and enthusiasm has propelled these devices forward, allowing the creation of extremely sophisticated blue and violet devices. The violet microlensed diode laser discussed is one of the newest additions to the diode family.

In this chapter, free-running microlensed diode lasers in the violet and red region of the spectrum are characterised. The goal is to show that high quality output beams are obtainable at these wavelengths, whilst retaining both good tuning and spectral characteristics of the diode laser systems. This is particularly relevant for the violet region, where poor beam quality is readily evident. In a separate experiment, the microlensed devices are characterised coupled to extended cavity geometries, by means of a diffraction grating.

5.2 Optical feedback

Employing some form of feedback into a diode laser can effectively modify an otherwise multimode diode into running on a single longitudinal mode. This can be achieved by incorporating a diffraction grating into an extended cavity geometry. Dispersion from a grating can both dramatically reduce the laser linewidth and allow for wavelength selectivity across the gain bandwidth of the diode material. On interacting with the diffraction grating, a narrow band of light is returned to the diode. This wavelength selective light is dependent on the angle of the diffraction grating. It can often be a slightly different wavelength to that of the free-running diode output. The central laser wavelength is therefore forced to around that of the feedback signal, making the laser cavity slave to the external master cavity. The feedback from the diffraction grating, in addition to influencing the diode wavelength, narrows the linewidth of the diode laser output due to the extended cavity restrictions.

Two common extended cavity configurations are the Littrow and Littman geometries. In the Littrow geometry, a grating is placed external to the diode, whereby the first order diffraction returns to the diode and the zeroth-order forms the usable output of the system [6]. A high output power can be obtained from this extended cavity system. A pseudo cavity is created between the grating and the back facet of the diode. Changes to the position of the grating can also finely tune the diode by incorporating a piezoelectric element (PZT). This smoothly changes the cavity length. The system described is known as an extended cavity diode laser. In comparison, the Littman geometry [7] incorporates a tunable feedback mirror to double pass the diffraction grating. This allows a narrower linewidth and a larger tuning range to be obtained, compared to the single-pass geometry of the Littrow configuration. Additionally, the Littman system allows the diode wavelength to be tuned without moving the output beam direction. In contrast, the simplicity of the Littrow configuration makes the output beam dependent on the diffraction grating angle. In the double pass configuration of the diffraction grating, the Littman geometry allows a narrower linewidth to be obtained at the expense of power. For spectroscopic applications, such as are considered later, the simplicity of the Littrow

configured extended cavity coupled with the higher output power is preferable in this instance.

Optical elements such as a diffraction grating can be used to disperse light. The diffraction gratings discussed here consist of closely spaced grooves ruled onto a reflective surface, which spread light out into its component parts. Obtained from a diffraction grating, this type of optical feedback crucially differs to that obtained from a microlens. The microlens acts to improve the diode lasers' spatial profile. This in turn leaves the spectral properties relatively unchanged. A microlens operates as a simple reflector, light is indiscriminately reflected at an angle similar to that incident upon it. A lens, which has been positioned to allow incident light normal to its surface, will also reflect a percentage of light, thus allowing feedback to return directly into the diode laser. This feedback imposes restrictions on the diode, forcing it to run on a single longitudinal mode. The key difference, in this method of optical feedback, is the lack of wavelength selectivity, compared to that obtained from a diffraction grating. A diffraction grating through the reflection of a narrow band of light improves both the diode lasers' spatial and spectral characteristics. Both of these optical feedback schemes are investigated in this chapter.

5.3 Microlensing a diode laser

Microlensed diode lasers have an incorporated cylindrical glass (schott F2 ~ 250 μm thick) microlens. This is placed approximately 50 microns from the laser facet, which dramatically improves the quality of the output beam. The lens's high numerical aperture (~ 0.7) maximises beam captive area influencing the entire output beam, effectively ensuring maximum power efficiency in the beam shaping conversion. This microlens compresses the fast axis of the beam emergent from the diode output facet down to that of the divergence angle of the slow axis [8], figure 5.1. Neither diode laser's microlens were anti-reflection coated, nor the devices themselves.

The microlens, along with dramatically improving beam spatial characteristics, also largely controls beam astigmatism. In standard diode devices, astigmatism originates from the emergent beam divergence. This is due to the diode output facet being greater in one axis than in the other. Essentially, this has the effect of causing two foci for the beam x and y planes. Coupling a beam into fibre optics is a simple, but lossy, method of circularising a beam, which can rid the system of this type of perturbation. This effect is demonstrated later. However, in applications where power is of paramount importance, this is not a viable option.

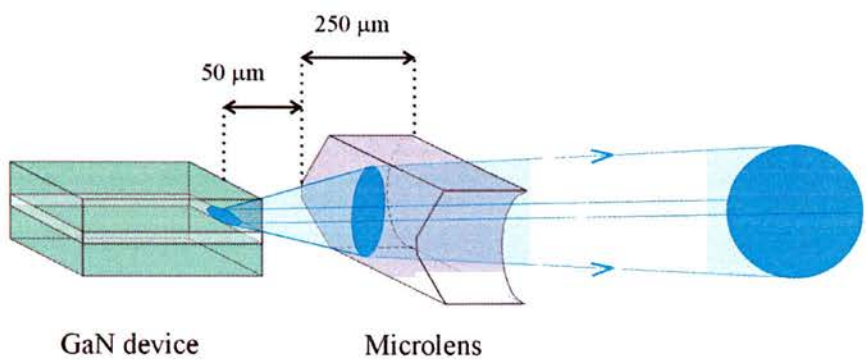

Figure 5.1. A microlens was placed 50 μm away from the gallium nitride (GaN) diode laser output facet. The 250 μm thick cylindrical lens allows beam shaping to circularise the laser output beam.

The microlensing process may typically be applied to any commercial semiconductor diode. In free-running mode, red microlensed diodes at 635 nm have previously demonstrated tuning over 30 GHz, by current variation. This allows spectroscopy of iodine [9]. A publication discussing a 780 nm microlensed diode laser has also recently been presented, placed in an extended cavity to yield a narrow linewidth tunable source, which is suitable for atom trapping [10]. Placing such a circularised device in an extended cavity requires consideration of competition between the cavity formed between the laser and the microlens, and the external cavity formed with the grating [9].

In addition to providing excellent beam quality, microlensing can also influence the spectral behaviour of the diode laser. Reflections from the surface of the lens can provide

weak feedback into the device, creating a very short extended cavity. This feedback places a constraint on the cavity and a wavelength dependent loss. These in turn cause a free-running microlensed diode laser to run single longitudinal mode. When running such laser diodes in an extended cavity, the additional microlens means the laser can exhibit a shorter continuous fine tuning range than a standard (non-microlensed) device in extended cavity [10]. It is possible that such a free-running microlensed laser can be locked to a cavity or an atomic transition line with feedback to the diode current.

It is proven that such cavity competition is not detrimental at near infra red wavelengths. But, notably, no studies exist of other, more challenging, diodes for example in the red and, particularly, the violet region of the spectrum. Importantly, violet diode lasers [11,12] have already proved themselves viable in an extended cavity geometry [6,13]. These sources are now making a significant impact in high-resolution spectroscopy, already utilised for spectroscopy of indium [14], calcium [15] and gallium [16], for example. These offer particularly attractive sources for regions of the spectrum that have previously been difficult to access.

5.4 Microlensed diode laser mounting

The microlensed (circularised) diode was placed inside a collimation tube [Thorlabs (Herts,UK) LT230P-A]. It was then set in a mirror mount supported on a home built aluminium mount, temperature stabilised to 10 mK, using a thermoelectric cooler (TEC). The TEC forms a bridge between the mirror mount plate and the aluminium base. The base acted as a heat sink to dissipate the heat away from the diode laser. This scheme is referred to throughout as the free-running laser system, the sole feedback contribution being obtained from the microlens. The diode laser head was rotated, due to the circularised beam shape, to determine polarisation. This was done by maximising output power through a $\lambda/2$ plate and a polariser. The respective diode systems were isolated to keep vibration and draughts to a minimum, reducing instabilities in characterisation measurements.

In a separate experiment, the circularised laser system was coupled to a Littrow configured extended cavity. A variety of diffraction gratings were placed less than two centimetres away from the collimated beam output facet. This design has been used in previous studies [10,17,18], seen in figure 5.2.

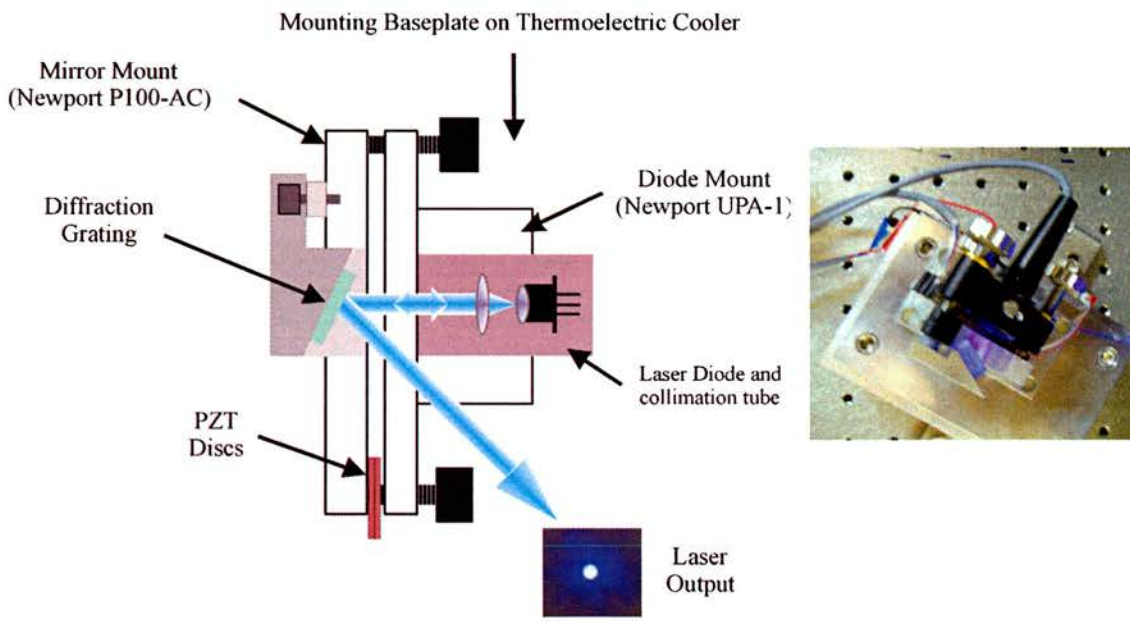

Figure 5.2. Schematic diagram of a microlensed diode laser mounted in the Littrow configuration shown with a photo of the circularised output beam. A photo of the violet (GaN) laser system is also shown on the right. For scale, the optical bench holes shown are set 25 mm apart.

The diffraction grating holders were machined at specific angles to allow feedback into the diode laser in the Littrow configuration. The chosen grating angle θ, was determined using equation 5.1 [19].

$$m\lambda = 2d\sin\theta \qquad [5.1]$$

where m is the diffraction order, λ is the incident wavelength and d the groove spacing on the diffraction grating. The violet diode laser was coupled with diffraction gratings with 2400 lines/mm and 1800 lines/mm corresponding to grating angles of 29.7 ° and 21.8 °, respectively. The 1200 lines/mm diffraction gratings coupled with the red diode laser were set at 23.4 °.

5.5 Microlensed diode beam shape

The intensity distribution of the laser, orthogonal to the propagation direction, forms the laser's transverse mode. By observing this mode the output beam emitted from the laser facet can be monitored. This provides insight into the quality, shape and astigmatism present in the beam. The effect of a microlens on a diode laser becomes apparent when observing this transverse mode emission, such as that shown in figure 5.2.

The microlensed diodes used in this work were a violet diode operating at 413 nm with a maximum free-running continuous wave output of 25 mW [Blue Sky Research (California, USA) VPSL-0450-N5B], and a red 661 nm continuous wave device at 50 mW (Blue Sky Research PS110). Diode laser devices in the violet spectrum can be wavelength selected from 395 nm to 440 nm. The output facet of the diode was not anti-reflection coated. The laser beam quality M^2, of both microlensed devices, was established by measuring beam radius at various distances from the beam waist. The beam divergence angle was found from these measurements and used to obtain M^2 values using equation 5.2 [20]. These values describe the deviation of the beam from an ideal diffraction-limited Gaussian beam where $M^2 = 1$.

$$M^2 = \frac{\pi w_o}{\lambda} \tan\theta \qquad [5.2]$$

where light of wavelength λ is focussed to a beam waist of w_o at a divergence angle of θ. Using a beam profiler (Thorlabs WM100), the 661 nm circulaser demonstrated a M^2 of 1.1 in the horizontal M_x^2, and 1.6 in the vertical M_y^2, plane. The 413 nm circulaser displayed M_x^2 and M_y^2 values of 1.3 and 1.5 respectively. In figures 5.3, the output beam profiles of two violet devices are shown, the 413 nm microlensed device and a standard 404 nm diode device. The 661 nm microlensed device is also shown with a fibre coupled 1064 nm Nd:YVO_4 laser, for comparison.

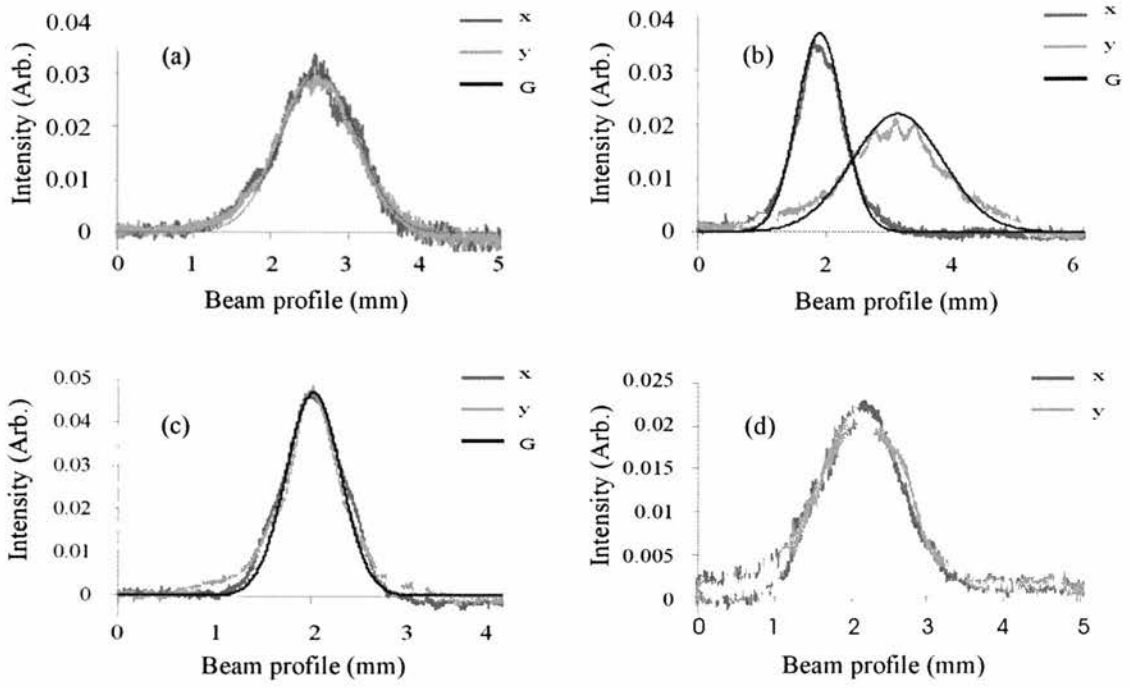

Figure 5.3. Beam profiles of (a) 413 nm microlensed diode, beam ratio 1:1.06, (b) standard diode laser at 410 nm, with a beam ratio of 1:2.02 and (c) 662 nm microlensed diode laser, beam ratio 1:1.09, where x and *y* are vertical and horizontal beam profiles fitted against a Gaussian profile *G*. and (d) 1064 nm SSL is observed for comparison.

5.6 Microlensed diode beam astigmatism

Diode lasers are notorious for having an elliptical output beam shape (figures 5.3). This ellipticity denotes that when focussed, the horizontal and vertical axes focus in different planes along the propagation direction, leading to an astigmatic beam. A standard method of measuring beam astigmatism is to focus a beam directly through an objective [21]. For simplicity, the optical tweezer system already constructed (previously discussed in chapter 4) was used to observe this effect.

A standard non-beam shaped 410 nm diode laser was observed, figure 5.3(b), and compared to two beam shaped lasers. A 780 nm microlensed diode laser similar to that shown in figure 5.3(c), and 1064 nm fibre coupled solid state laser, shown in figure 5.3(d), were used. (Both violet and red microlensed devices were in use at the time of

measurement, therefore, a 780 nm microlensed device was used as a compare.). All diode lasers are formed slightly differently and will suffer different degrees of astigmatism. The 780 nm microlensed device therefore only shows an example of the perturbation expected from the violet and red diodes.

The beam foci of each laser were observed in the plane of the tweezer sample stage, brought into focus using the z-axis actuator. The stage was moved to minimise the respective beam waists in both x and y axes along the beam propagation direction. Due to slight misalignment of the beam through the imaging relay of the optical tweezer, extra perturbation was introduced into the system. For that reason, measuring beam astigmatism in this manner only allows results obtained through this system, to be compared with each other. The circulaser at 780 nm showed an astigmatism of < 1 μm between foci. This is a considerable improvement over the 410 nm standard diode laser showing a 10 μm astigmatism. The fibre-coupled solid-state laser showed negligible astigmatism, easily inferred from beam profiles previously observed in horizontal and vertical directions, figure 5.3(d). The microlensed diode laser shows improvement over the standard elliptical beam shape significantly reducing laser astigmatism by a factor of 10. This is in agreement with the beam profiles shown in figures 5.3, where the standard diode exhibits a considerable difference in x and y beam profiles.

5.7 Diffraction gratings

Both diodes were placed in an external cavity system based on a previous design [10], figure 5.2. A diffraction grating in the Littrow configuration allowed the first order to feedback into the diode laser, reflecting off the zeroth order beam as the useable output power. Eight separate diffraction gratings were used with the diodes, four with each device. All eight gratings were obtained from Optometrics and are summarised in table 5.1. Each diffraction grating was placed 13 mm from the red laser output facet and 9 mm from the violet output facet, set by the mounting design for the respective laser. Variation of these diffraction gratings can influence the linewidth and tuning range of the laser systems and ultimately the maximum useable output power. A grating blaze closest to the

laser wavelength provides a broad coarse tuning range at the expense of output power. Grating position is also of great importance, longer cavities narrowing linewidth whilst reducing continuous tuning ranges. A PZT element was attached to the horizontal adjustment of the mirror mount upon which the diffraction grating was situated. Dithering the voltage applied to the PZT allowed a continuous (fine) tuning range to be obtained. By coarsely adjusting this mirror mount control in steps of approximately 1/8 of a turn the discontinuous (coarse) tuning range for each external cavity was determined.

Grating	Part no. (The Optometrics Group)	Blaze (nm)	Lines /mm
661 nm			
Red A	3-4175	750	1200
Red B	3-4121	HoloUV	1200
Red C	3-4130	300	1200
Red D	3-4140	400	1200
413 nm			
Blue A	3-4241	HoloUV	2400
Blue B	3-4185	500	1800
Blue C	3-4182	HoloVis	1800
Blue D	3-4181	HoloUV	1800

Table 5.1. A range of optometric diffraction gratings were used with the red and violet microlensed diode lasers of blaze and ruled line separation as shown.

5.8 Output power

The power characteristics of both 413 nm and 661 nm circularised diode lasers in both free-running and external cavity geometries were investigated. The output power was controlled and varied with injection current and the thresholds compared for red and violet diode lasers. In free-running geometry the 661 nm diode emits 50 mW of output

power, and the 413 nm diode 24 mW. For all power measurements, the red diode was kept at constant temperature of 21.6 ± 0.1 °C, and the violet diode at 21.8 ± 0.1 °C.

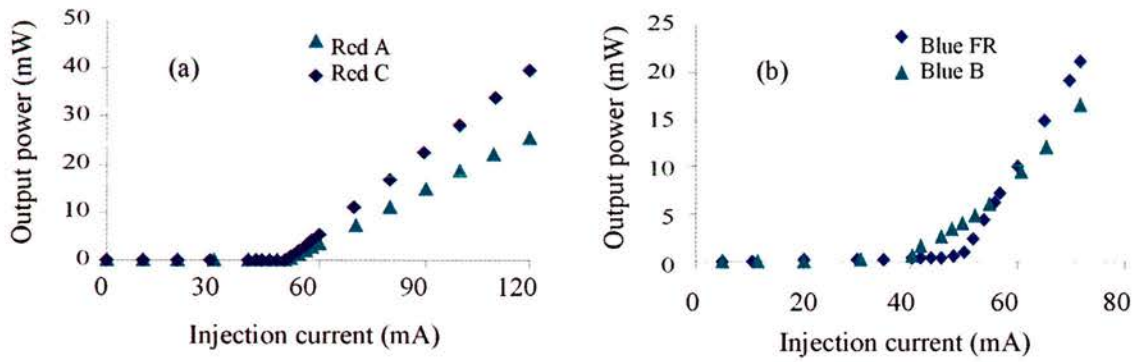

Figure 5.4. Power output against injection current of the (a) red (Gratings A and C) microlensed diode lasers and (b) violet (Free running, FR, and grating B).

Figure 5.4(a) compares the red microlensed diode coupled with two different diffraction gratings. Grating *Red-C* shows the greatest power output, 40 mW, due to the blaze wavelength of the grating being the furthest from the operational wavelength of the diode laser. Less feedback into the diode laser allows more power to be utilised into the lasing output. This is also demonstrated with grating *Red-A* as the grating blaze is closer to the laser wavelength, diminishing the available output power to 26 mW, (grating *Red-D* was slightly damaged accounting for its unusually low power output). Data for all eight diffraction gratings is summarised in table 5.2. A similar power diminishing effect can be seen for the violet microlensed diode laser. Figure 5.4(b) compares the power output obtained from the violet free-running system with that of the extended cavity with grating *Blue-B*. The available diffraction gratings were reasonably close in wavelength to the diode emission thus considerably reducing the maximum output power produced in extended cavity to 13 mW. Figure 5.4(b) also shows a reduced current threshold due to the presence of a diffraction grating, allowing lasing to occur at a lower injection current. This lowering of laser threshold holds true for all gratings tested.

661 nm	Power Output (mW)	Threshold I (mA)	*413 nm*	Power Output (mW)	Threshold I (mA)
FR	50	50.8	FR	24	49.1
Red-A	26	50.0	Blue-A	13	45.4
Red-B	32	45.3	Blue-B	1	42.9
Red-C	40	50.6	Blue-C	5	46.4
Red-D	6	42.3	Blue-D	6	42.9

Table 5.2. The power output and threshold currents for free-running (FR) and extended cavity (EC) red and violet microlensed lasers are shown.

5.9 Laser linewidth and tuning

The cavity imposes restrictions on the laser, only permitting certain operating wavelengths to propagate. Longitudinal modes of particular wavelengths are encouraged to thrive whilst others are suppressed. Exclusive selection of these modes is possible with weak feedback from a microlens creating an extended cavity. Coupling to a diffraction grating external cavity introduces additional constraints, further reducing the linewidth of the diode. This linewidth is simply the spread of allowed frequencies satisfying all defined cavities.

To determine the laser linewidth and continuous tuning range, the output was directly observed using a Fabry-perot etalon on a spectrum analyser. For the red diode a spectrum analyser with a 300 MHz free spectral range, FSR, and finesse of 300 was used, and for the violet, an analyser with a FSR of 1 GHz and a finesse of 500.

For all linewidth and tuning measurements, the red diode was set at 21.6 ± 0.1 °C. The violet laser was kept constant at 21.8 ± 0.1 °C for all linewidth and tuning measurements, with the exception of the free-running continuous tuning range, where it was held at the higher value of 23.8 ± 0.1 °C. This corresponded to the temperature where the diode's tuning range is greatest.

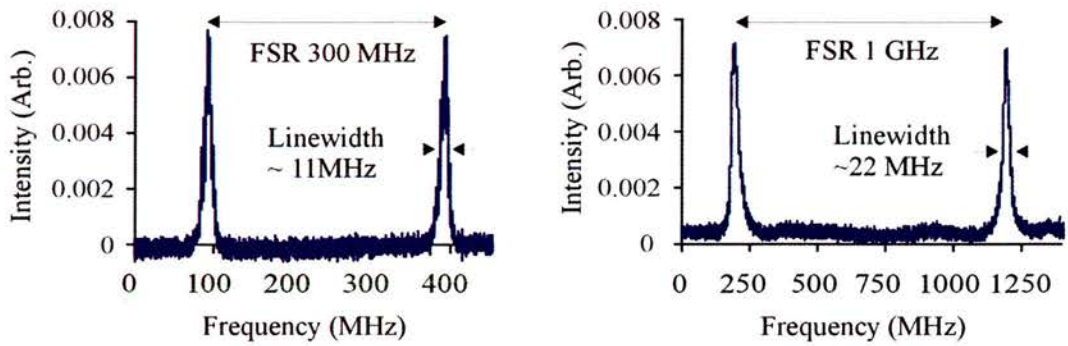

Figure 5.5. Free-running linewidth of the (a) 661 nm microlensed laser (11 MHz, taken at a scan rate of 0.4 ms), with FSR (300 MHz) and (b) 413 nm microlensed laser (22 MHz, taken at a scan rate of 2 ms), with FSR 1GHz.

The red 661 nm diode laser provided a linewidth of 11 MHz (0.4 ms Oscilloscope (OSO) scan time), shown in figure 5.5(a). This is slightly larger than other publications for microlensed systems of 4 MHz at 633 nm [9]. A continuous mode-hop free tuning range over 55 GHz was observed by varying the current, from 106.8 mA – 119.4 mA, thus showing a tuning rate of 4.38 GHz/mA. The violet diode at 413 nm gave a linewidth of less than 22 MHz (2 ms OSO scan time), figure 5.5(b). Current modulation, from 51.8 mA – 62.7 mA, at 5.06 GHz/mA provided a continuous tuning range of 40 GHz. A section of this tuning range is shown in figure 5.6.

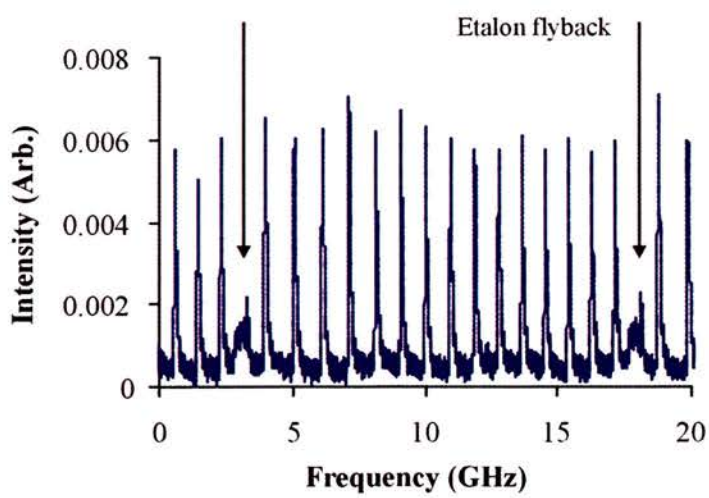

Figure 5.6. Free-running continuous tuning range of the blue circularised diode laser is given. A section of single mode operation is shown across the laser gain bandwidth.

The re-occurring feature indicated with arrows is a characteristic of the scan generator (Thor labs, miniScan 102) used to dither the scanning etalon mirror. On reaching the limit of its travel, the mirror is reset, producing this flyback signal.

The violet and red diodes also showed temperature tuning coefficients of 0.45 nm/K and 0.11 nm/K respectively. This free-running ability to run single longitudinal mode is in contrast to the standard diode lasers at these wavelengths that run multimode. Therefore, the addition of a microlens allows the simplification of the diode laser system. This data of mode-hop-free tuning and narrow linewidths shows that free-running microlensed systems offer practical spectroscopic tools with very large tuning ranges. These may prove particularly powerful in the violet region of the spectrum.

In external cavity, a diode laser's discontinuous tuning range is determined through course tuning of the diffraction grating around the diodes central wavelength. The first order beam fed back into the diode is wavelength tuned, using the grating angle to change the cavity length. If the grating, and thus the first order beam, is tuned too far the diode will jump out of external cavity. Displacing this optical feedback with respect to the output beam pulls the wavelength wide, as it is coarsely tuned across the zeroth-order.

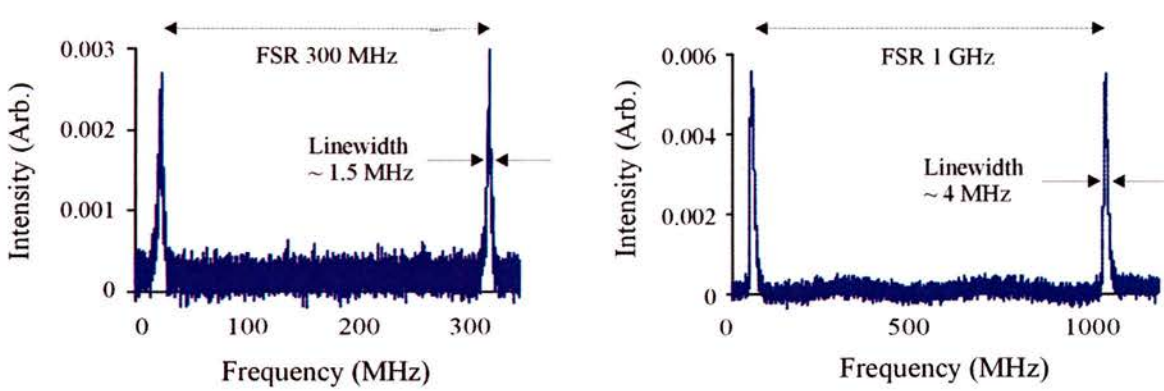

Figure 5.7. Extended cavity linewidth of the (a) 413 nm microlensed laser (4 MHz, taken at a scan rate of 10 ms) and (b) 661 nm microlensed laser (1.5 MHz, taken at a scan rate of 10 ms), with FSR (1 GHz).

Grating *Red-C* with 1200 lines/mm and a blaze of 300 nm was used in external cavity coupled to the 661 nm circulaser. This configuration provided a linewidth of 7 MHz (0.4 ms OSO scan time) with a continuous PZT tuning range over 4 GHz and a discontinuous tuning range over 7 nm. A linewidth of 1.5 MHz (0.4 ms OSO scan time) was found with the damaged grating *Red-D* which had 1200 lines/mm and a blaze of 400 nm. This is shown in figure 5.7(a).

The change in wavelength that both devices undergo as they are coarsely tuned around their central wavelengths can be seen in figure 5.8, with the red microlensed diode coarsely tuning further than the violet device. Linewidth and tuning data for the eight gratings are summed up in table 5.3.

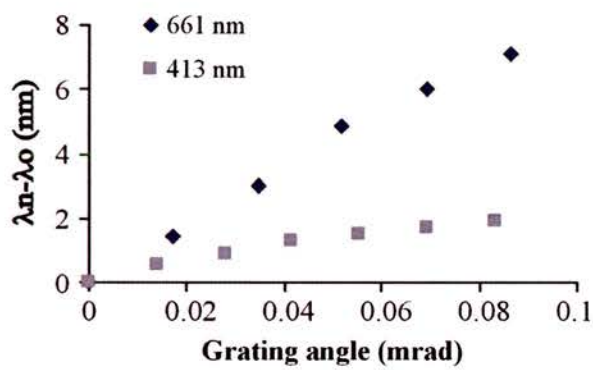

Figure 5.8. Change in wavelength with grating angle for both microlensed lasers (discontinuous Tuning), 413 nm tuning 5 nm at 24 °C and 661 nm tuning 7 nm at 22 °C.

The 413 nm circulaser was continuously tunable over 6 GHz in an external cavity using a holographic UV grating with 2400 lines/mm, grating *Blue-A*. This provided a 4 MHz linewidth (1ms OSO scan time) seen in figure 5.7(b), coarsely tunable over 2 nm.

Grating	Linewidth (MHz)	Fine tuning (GHz)	Coarse tuning (nm)
661 nm			
FR	11	55	-
Red-A	6	6	11
Red-B	11	4	6
Red-C	7	4	7
Red-D	1.5	6	8
413 nm			
FR	22	40	-
Blue-A	4	6	2
Blue-B	9	6	5
Blue-C	8	5	3
Blue-D	4	5	4

Table 5.3. A summary of the data from free-running (FR) and extended cavity (EC) geometries using different Optometrics diffraction gratings is shown. The red cavity was 13 mm in length and the violet cavity 9 mm in length, measured between laser output facet and diffraction grating.

5.10 Conclusion and discussion

In this chapter, 413 nm and 661 nm microlensed diode lasers have been characterised in both free-running and external cavity geometries. These devices exhibit narrow linewidths with large continuous tuning ranges ideal for spectroscopic studies. However, they have had relatively little use in the literature. Significantly, the violet microlensed diode laser exhibits considerable improvement to its spatial and spectral characteristics over those seen from standard diode lasers at similar wavelengths. Violet microlensed devices may therefore find important applications in high-resolution studies. Such applications are considered in the remaining chapters.

The red microlensed diode has shown a large mode-hop-free tuning range in a free-running geometry of 65 GHz, and the violet device 40 GHz. In extended cavity, the 413 nm circulaser provided single longitudinal mode of linewidth 4 MHz, with a continuous tuning range of 6 GHz and a discontinuous tuning range over 5 nm. The 661 nm circularised diode in external cavity showed continuous and discontinuous tuning ranges of 6 GHz and 11 nm, respectively. The linewidth for the 661 nm system is comparable with other publications for microlensed systems. The 413 nm diode linewidth is comparable with standard external cavity diode lasers, previous publications having shown a linewidth of less than 5 MHz at 392 nm [13].

5.11 References

[1] C. E. Weiman and L. Hollberg, "Using diode lasers for atomic physics", Rev. Sci. Instrum. **62** 1 (1991)

[2] A. Hemmerich et al., "Optically stabilized narrow linewidth semiconductor laser for high resolution spectroscopy", Opt. Comm. **75** 118 (1990)

[3] C. Y. Park and T. H. Yoon, "Frequency stabilization of injection-locked violet laser diode with Doppler-free absorption signal of ytterbium", Jpn. J. Appl. Phys. **42** L754 (2003)

[4] K. Komori et al., "Injection-locking of blue laser diodes and its applications to the laser cooling of neutral ytterbium atoms", Jpn. J. Appl. Phys. **42** 5059 (2003)

[5] L. Ricci et al., "A compact grating-stabilized diode laser system for atomic physics", Opt. Comm. **117** 541 (1995)

[6] D. J. Lonsdale et al., "Extended tuning and single-mode operation of an anti-reflection-coated InGaN violet laser diode in a Littrow cavity", Meas. Sci. Technol. **13** 488 (2002)

[7] K. Lui and M. G. Littman, "Novel geometry for single-mode scanning of tunable lasers", Opt. Lett. **6** 117 (1981); R. Merrill et al., "Increasing the output of a Littman-type laser by use of an intracavity Faraday rotator", Appl. Opt. **43** 3910 (2004)

[8] Coherent, "Beam circularisation and astigmatism-correction", Laser diode technical note 1

[9] H. Talvitie et al., "Frequency stabilization of a diode laser to Doppler-free spectrum of molecular iodine at 633 nm", Opt. Comm. **152** 182 (1998)

[10] G. P. T. Lancaster et al., "An extended-cavity diode laser with a circular output beam", Rev. Sci. Instrum. **71** 3646 (2000)

[11] S. Nakamura et al., "InGaN-based multi-quantum-well-structure laser diodes", Jpn. J. Appl. Phys. **35** L74 (1996)

[12] S. Nakamura et al., "The Blue Laser Diode", 2nd Ed. Springer 2000

[13] R. S. Conroy et al., "Characterisation of an extended cavity violet diode laser", Opt. Comm. **175** 185 (2000)

[14] H. Leinen et al., "GaN blue diode lasers: a spectroscopist's view", Appl. Phys. B **70** 567 (2000)

[15] G. P. T. Lancaster et al., "Doppler cooling a single Ca^+ ion with a violet extended-cavity diode laser", Appl. Phys. B **76**, 805 (2003)

[16] O. M. Maragò et al., "Atomic gallium laser spectroscopy with violet/blue diode lasers", Appl. Phys. B **77** 809 (2003)

[17] M. G. Boshier et al., "External-cavity frequency-stabilization of visible and infrared semiconductor lasers for high resolution spectroscopy", Opt. Comm. **85** 355 (1991)

[18] M. A. Clifford et al., "High-order Laguerre-Gaussian laser modes for studies of cold atoms", Opt. Comm. **156** 300 (1998)

[19] Spectra-Physics, "Determination of the blaze wavelength", Technical note 11

[20] Duncan Hand, Lecture course material M.Sc. Heriot-Watt University (2001)

[21] Melles Griot, http://lasers.mellesgriot.com/Appnotes.asp?F=corastig, Diode laser circularisation

Chapter 6

Sum frequency generation of UV light

6.1 Introduction

In recent years, the diode laser has become an invaluable source for spectroscopy, offering ever increasing output powers provided in an adaptable compact source. Previously, limitations to the diode laser output wavelength meant these devices have been overlooked in favour of more expensive systems. However, with the emergence of violet and blue devices, these sources have now found employment in non-linear frequency conversion processes [1,2,3]. Bulky dye or Argon ion lasers have traditionally been used to gain access to the ultraviolet (UV) region, using frequency doubling and sum frequency generation techniques [4,5,6]. Due to the poor efficiency of non-linear processes, the high output power obtained from such lasers is necessary. Additionally, to increase generated output power, the system can be incorporated into an enhancement cavity to multi-pass the non-linear crystal [7,8].

Argon ion and dye lasers have also found use, when coupled with diode lasers, to sum frequency generate light in the UV, due to their low emission wavelength. Recent work has used these dye or argon ion lasers, in a sum frequency and second harmonic generation multi-pass enhanced cavity configuration, to access the UV region at 194 nm

[7], 369 nm [9] and 213 nm [8], to name but a few. The high power available from such bulky sources allows a significant sum frequency generated output. However, the development of diode lasers has provided high quality devices emitting in the violet region of the spectrum. Although such devices offer comparatively low output powers and tuning characteristics, their ability to be incorporated into compact reliable systems makes them both practical and attractive sources. Diode lasers can therefore often be the source of choice when the sum-frequency generation of light is required for spectroscopic applications.

The advantage of microlensed diode lasers is their significant improvement in beam shape over earlier diode devices in both the red and violet region. The circularised nature of these diodes can allow for a good beam overlap inside the non-linear crystal. In addition, the circularised beam reduces astigmatism at beam focus and can also significantly affect the efficiency of the crystal. These devices can potentially provide a much more efficient sum frequency system, compared to previous diode laser systems, thus offering a considerably cheaper alternative to the argon ion and dye lasers. In addition, the circularised beam also avoids the use of power lossy optics, such as beam shaping prisms and cylindrical lenses. This allows maximum power utilised in the non-linear process, and thus further simplifies the optical system.

Non-linear processes can be exploited to access regions of the spectrum inherently difficult to reach through direct laser emission. The advance of violet diode laser devices has provided an exciting range of wavelengths, creating possibilities of a more compact method to reach the UV region. Laser frequencies must be phase-matched within a non-linear crystal for this to occur efficiently. Under certain conditions, a non-linear process can allow for the generation of a higher frequency, through the addition of the fundamental laser frequencies. This is known as sum frequency generation. It is the only non-linear process experimentally realised in this chapter.

In the first part of this chapter, light at 269 nm and 254 nm is produced through sum frequency generation. In both cases the two fundamental frequencies are a red and a

violet diode laser source, to gain access to ultra-violet wavelengths. The first experiment was used as a test case utilising readily available lasers, a red TUI diode laser at 780 nm and a violet diode laser at 408 nm to produce UV light at 269 nm. The second experiment involved a red microlensed diode laser specifically chosen to match a violet microlensed diode laser, both previously discussed in chapter 5. This allowed generation of UV light at 254 nm. This generated light was then employed for spectroscopy with mercury, to observe its prominent transition line at 253.7 nm. This experiment is discussed in chapter 7.

6.2 Birefringence

In some materials the orientation of a crystal can be set to allow light propagation at an angle to its optic axis, such that a double image is created through it. Such separation of light into two components is due to the crystal having two refractive indices. This is known as birefringence. In such materials, there is an asymmetry to the crystal lattice that a propagating beam sees as a difference in refractive index. This fundamental property causes the double refraction phenomenon.

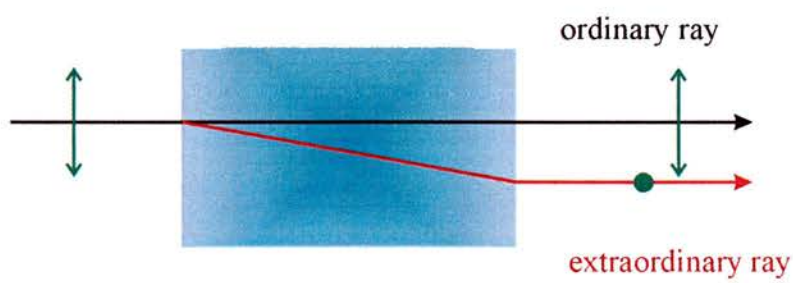

Figure 6.1. A vertically polarised ray is shown going through a type I negative uniaxial crystal. The extraordinary ray diverges off at an angle with a polarisation orthogonal to the ordinary ray.

It is the exploitation of this phenomenon that allows non-linear processes to create efficient light generation at higher frequencies. Such crystals of this kind are known as uniaxial. The crystal lattice acts as a polariser allowing one beam to pass, whilst an orthogonally polarised beam is deflected. Materials affecting light in this way can be

exploited to produce polarising beam splitters such as Wollaston and Glan-Thomson prisms.

Vertically polarised light, shown in figure 6.1, enters the crystal perpendicular to the crystal facet, with a zero angle of incidence, travelling normal to the surface. Upon entering the crystal, the beam is split into two orthogonally polarised rays. The first ray of similar polarisation predictably passes straight through the crystal in accordance with Snell's law. This ray is therefore known as the ordinary ray (o-ray). However, the second beam perpendicularly polarised to the first is deflected from this path. This ray is called the extraordinary ray (e-ray), as it violates Snell's law. Both rays are slowed to a velocity dictated by the refractive index. For a negative uniaxial crystal, such as the BBO crystals used here, the e-ray will see a lower refractive index than that of the o-ray. This causes the e-ray to travel faster through the crystal. Consequently its wave front will be ahead of the o-ray.

6.3 Non-linearity

Optical processes in a dielectric medium can be described in terms of the polarisation $\underline{P}$, in the medium and its optical electric field, $\underline{E}$. Polarisation is the net electric dipole per unit volume, expressed here as equation 6.1 [10]:

$$\underline{P}(r,t) = \varepsilon_o(\chi^{(1)}\underline{E}(r,t) + \chi^{(2)}\underline{E}^2(r,t) + \chi^{(3)}\underline{E}^3(r,t) + ...) \qquad [6.1]$$

where ε_o is the permitivity of free space and $\chi^{(t)}$ is the susceptibility of the medium. Depending on the material, the relevant terms in this equation differ. In classical optics, $\underline{P}$ and $\underline{E}$ have a linear relationship that governs light behaviour such as refraction and reflection. However, in some materials this linearity is lost in the presence of an intense electric field, such as that obtained from a focussed laser beam, the polarisation of the medium thus simplifies to include the $\chi^{(2)}$ term, equation 6.2 [10]:

$$\underline{P}^{(2)}(r,t) = \varepsilon_o\chi^{(2)}\underline{E}^2(r,t) \qquad [6.2]$$

This non-linearity results from electron displacement inside the medium, analogous to the breakdown of Hooke's law, when a large pulling force is used to warp a spring [10]. The

determination of whether a material exhibits this behaviour is due to the crystal's symmetry. Centro-symmetric crystals do not exhibit the $\chi^{(2)}$ term required for non-linearity [10]. The origin of non-linearity is therefore due to the higher order $\chi^{(2)}$ and $\chi^{(3)}$ terms expressed in equation 6.1 and can cause a change in the frequency of light. Fundamental oscillating electric fields can be written $E(t) = E\cos\omega t$, where light of amplitude E oscillates at a frequency ω over time t.

Focussed laser light incident on a non-linear crystal can cause both a higher and lower frequency of light to be produced. Two electric fields at frequencies ω_1 and ω_2 propagating in a $\chi^{(2)}$ medium can therefore yield equation 6.3.

$$P^{(2)} = \varepsilon_o \chi^{(2)} E(t) E(t) = \varepsilon_o \chi^{(2)} EE\cos^2 \omega t$$
$$= \varepsilon_o \chi^{(2)} E_1 E_2 [\cos(\omega_1 + \omega_2)t + \cos(\omega_1 - \omega_2)t] \quad [6.3]$$

This expression yields two new frequency terms at a higher sum frequency $(\omega_1 + \omega_2)$ and a lower difference frequency $(\omega_1 - \omega_2)$. In this chapter I discuss the sum frequency case only.

6.4 Photon model

Fundamental light incident on the non-linear crystal can propagate through, being unaffected. However, occasionally the crystal can induce photon interaction with a red and a violet photon. The non-linear crystal on "absorbing" the two fundamental photons causes a summing effect, generating a light component of a higher frequency, shown in figure 6.2.

Figure 6.2. The photon model represents frequency conversion of two fundamental wavelengths interacting with the non-linear crystal into a higher frequency.

In this sum frequency generation process, energy is conserved (equation 6.4) and, therefore, light attributing to the process can be expressed as:

$$\omega_{uv} = \omega_{red} + \omega_{violet} \qquad [6.4]$$

The photon model (figure 6.3) is a naïve method for describing the sum frequency generation process, due to its avoidance of key elements in non-linear processes. However, it is a useful point of view for a simplistic illustration of the frequency conversion process [11].

6.5 Phase-matching

The conservation of energy in a non-linear process allows maximisation of the generated output. This ideal (equation 6.4) can be simply rewritten using the relations $\omega = 2\pi\nu$ and $c = \nu\lambda n$ yielding equation 6.5;

$$\frac{n(\lambda_{uv})}{\lambda_{uv}} = \frac{n(\lambda_{red})}{\lambda_{red}} + \frac{n(\lambda_{violet})}{\lambda_{violet}} \qquad [6.5]$$

Here, UV light of wavelength λ_{uv} is generated using fundamental wavelengths of λ_{violet} and λ_{red}. The refractive index of the crystal is denoted n at each respective wavelength. This is known as the phase-matching condition, which can also be expressed as (equation 6.6)[10];

$$\Delta k = k(\omega_{UV}) - k(\omega_{red}) - k(\omega_{violet}) \qquad [6.6]$$

where Δk is the phase mismatch and k is the wavevector at a fundamental or generated wavelength. Light generated at the higher frequency of ω_{UV}, as previously mentioned, travels through the crystal at a different speed to the fundamental beam, due to dispersion. When $\Delta k = 0$ there is no dispersion in the crystal and energy is conserved. The phase-matching condition is satisfied, by maximising the generated UV output. However, typically, due to the presence of dispersion $\Delta k \neq 0$.

6.5.1 Type I and type II phase-matching

Light polarisation is key in non-linear processes. There are two types of fundamental beam orientation. Type I (described here) allows for both beams to interact with the non-linear crystal with similar polarisations. The case where the fundamental beams are orthogonally polarised with respect to each other is known as type II. The angle at which the Beta-Barium-Borate (BBO) crystal (the type of non-linear crystal used here) was cut was considered, knowing the wavelengths of the fundamental beams and the type of beam coupling preferred inside the crystal.

In a type I uniaxial crystal, the linearly polarised fundamental light not contributing to the non-linear process passes through the crystal in the form of an o-ray (similar to figure 6.2). The sum frequency generated light is orthogonally polarised to these fundamental beams and is deflected from the propagation axis in the form of the e-ray [12]. If the two fundamental beams do not have similar polarisations for type I phase-matching, they will be unable to produce sum frequency generated light.

For a negative uniaxial crystal, both fundamental rays are ordinary, combining to generate an extraordinary ray at a higher frequency ($o+o \rightarrow e$). The phase matching condition, where $\Delta k = 0$, can therefore be satisfied in sum frequency mixing by exploiting the e-ray's dependence on phase velocity [11], which changes with the crystal propagation direction. This allows the phase-matching condition to be satisfied by manipulating the wavevector angles, with respect to the optic axis, of the fundamental beams through the crystal. The wavevector is therefore orientated such that the refractive index of the fundamental waves equals that of the generated wave, $n_o^{red} = n_o^{violet} = n_e^{UV}(\theta)$. The phase-matching angle can be calculated using equation 6.7 [11]:

$$\frac{1}{n_e^2(\theta)} = \frac{\cos^2\theta}{n_o^2} + \frac{\sin^2\theta}{n_e^2} \qquad [6.7]$$

where θ is the angle made between the crystal's optic axis and the propagation direction.

6.5.2 Sellmeier equations

The refractive index seen by the light incident on the crystal is highly dependent on the wavelength of that light. For the ideal angle at which phase-matching occurs to be found, the refractive index each ray sees must be known. The o- and e-ray indices for any particular non-linear crystal are described by the Sellmeier equations seen below for BBO, plotted in figure 6.3 [13]. The wavelength here is measured in microns. The constants in these equations change, dependent on the crystal.

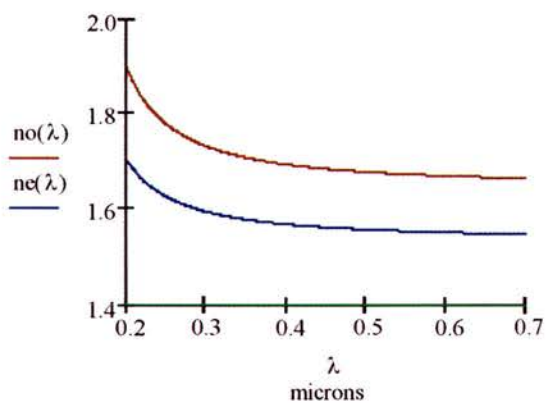

$$n_o^2(\lambda) = 2.7359 + \frac{0.01878}{\lambda^2 - 0.01822} - 0.01354\lambda^2$$

$$n_e^2(\lambda) = 2.3753 + \frac{0.01224}{\lambda^2 - 0.01667} - 0.01516\lambda^2$$

Figure 6.3. The Sellmeier equations for a BBO crystal describe the refractive index dependence on wavelength.

6.6 Sum frequency generated power

6.6.1 Theoretical UV power

The theoretical sum frequency generated power obtained through the crystal is directly proportional to the product of the fundamental beam powers, expressed as equation 6.8 [14,27].

$$P_3 = \frac{16 d_{eff}^2 m^2 l^2 \omega_1 \omega_2 P_1 P_2}{\pi \varepsilon_o c^3 n_1 n_2 n_3} \qquad [6.8]$$

Here P_1, P_2 and P_3 are the fundamental red and violet, and sum frequency UV output powers, at frequencies of ω_1, ω_2 and ω_3, respectively. The crystal of length l, has a

refractive index n_3 (of the generated UV beam), where d_{eff} is the effective non-linear coefficient, and c and ε_0 have their usual meanings of the speed of light and the permittivity of free space. The mean wave vector can be expressed as $k_0 = (k_1 + k_2)/2$, where each fundamental beam wave vectors denoted i, can be represented by equation 6.9 [15].

$$k_i = \frac{2\pi n_i}{\lambda i} \qquad [6.9]$$

A factor m, is included to take into account the difference of each beam focussing within the crystal, equation 6.10.

$$m = \frac{w_1 w_2 w_3}{w_1^2 w_2^2 + w_1^2 w_3^2 + w_1^2 w_3^2} \qquad [6.10]$$

$$\frac{1}{w_3^2} = \frac{1}{w_1^2} + \frac{1}{w_2^2} \qquad [6.11]$$

Expression 6.10 can be reduced using equation 6.11, which can be further simplified to $w_3 = w_{1,2}/\sqrt{2}$ when both fundamental beams have equal waists. This yields equation 6.12, rewritten in terms of a conversion efficiency η, for the sum frequency process, as described in [14,27].

$$\eta = \frac{P_3}{\sqrt{P_1 P_2}} = \frac{2 d_{eff}^2 l^2 \omega_1 \omega_2 \sqrt{P_1 P_2}}{\pi \varepsilon_o c^3 n_1 n_2 n_3 w_{1,2}^2} \qquad [6.12]$$

Equation 6.12 can also be expressed for optimum phase-matching as equation 6.13 [27]. A reduction factor $h(B,\xi)$, is introduced due to focussing and walk-off effects. This equation is only applicable for confocal focussing, such as in a second harmonic generation system. Where this is not the case, and the fundamental beams have unequal confocal parameters the more generalised version, shown in 6.8, must be used.

$$P_3 = \frac{2 d_{eff}^2 \omega_1 \omega_2 P_1 P_2 l k_o h(B,\xi)}{n_1 n_2 n_3 c^3 \varepsilon_o \pi} \qquad [6.13]$$

The focussing factor $h(B,\xi)$, is a dimensionless number introduced by Boyd and Kleinman [14] acquired from figure 6.4, shown below. From this figure it can be seen that $h(B,\xi)$ is a function dependent on the walk-off parameter B, and focussing parameter ξ, which can be expressed as equations 6.14 and 6.15 respectively [14].

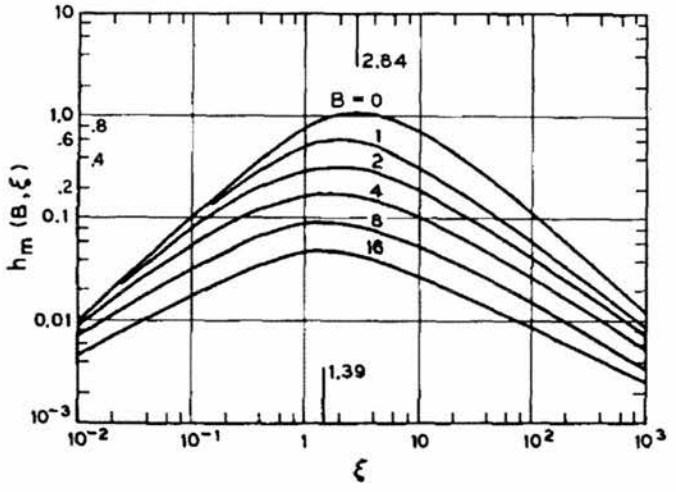

Figure 6.4. Boyd and Kleinman graph showing their calculation of focussing factor $h(B,\xi)$, [14]. From this it is possible to get a numerical value of $h(B,\xi)$ for sum frequency mixing.

$$B = \frac{\rho}{2}\sqrt{lk_o} \qquad [6.14]$$

$$\xi = l / b_{eff} \qquad [6.15]$$

Here ρ is the birefringent walk-off angle (expressed in radians), and b the confocal parameter is shown here in equation 6.16 [15].

$$b_i = \frac{2\pi\omega_{oi}^2 n_i}{\lambda_i} \qquad [6.16]$$

As can be seen, this confocal parameter is dependent on wavelength and the focussed beam waist. For this reason, for a sum frequency process, an effective confocal parameter b_{eff}, allows the respective beam properties to be considered. This equation is shown in 6.17 [14].

$$b_{eff} = \frac{k_1 b_2 b_3 + k_2 b_1 b_3 + k_3 b_1 b_2}{k_1 b_1 + k_2 b_2 + k_3 b_3} \qquad [6.17]$$

The power obtained through equation 6.8 assumes the ideal case of a crystal with complete absorption. A factor of $\exp(-\alpha l)$ can be used to take into account the absorption of the crystal, where α is the averaged absorption coefficient of the fundamental and sum frequencies [8]. A factor $(1-\gamma^2)$ can also be used to describe the deviation of sum frequency from the second harmonic, where $\gamma = (1 - w_{1/2}/w_o)$ [2].

6.6.2 Confocal parameters

There seems to be little compelling evidence that fundamental beam confocal parameters be equal to maximise sum frequency mixing [9,16]. In fact, it is accepted that it is not always convenient to have them so, and that beam waist matching can provide higher efficiencies. Although matching the beam waists of the two fundamental beams allows a good overlap in the focal region, the overlap throughout the crystal is not as good. To increase the beam overlap, it can be more efficient to alter the beam foci to maximise the overall overlap throughout the crystal. This can occur matching beam confocal parameters. Ruffling et al. [17] compares these two cases to maximise generated UV power. This is discussed further, later in this chapter, comparing the beam overlap obtained from a range of beam waists and confocal parameters.

In the literature, some papers on sum-frequency generation equate confocal parameters to simplify the theoretical power analysis [8,14]. Additionally, some papers simplify the power equation by effectively averaging the fundamental frequencies [1,2]. Here, for simplicity, the average of the confocal parameters of both fundamental beams was taken.

6.7 Sum frequency mixing

In this experimental section two separate regions of UV light are generated using sum frequency mixing. Initially, a test case producing light around 269 nm was carried out using two readily available lasers already in the research group, a TUI red diode laser at 780 nm, and a 408 nm diode laser. Subsequently, an experiment was designed using the diodes previously discussed in chapter 5. The 413 nm microlensed diode laser was a bought-in device and the red crudely matched to allow absorption spectroscopy of the 254 nm intercombination line of mercury. Once this wavelength was generated, the UV was maximised through the system by manipulating and alternatively matching beam waists and confocal parameters. Thus the overlap of the fundamental beams was experimentally optimised.

6.7.1 Generation of 269 nm light

A 100 mW 780 nm diode laser (TUI TA100) and a 8 mW 408 nm diode laser (Nichia NDHV310ACA) were chosen to access the UV region, using sum frequency generation. The diode lasers were both vertically polarised. Half wave plates were used in both beams to optimise this polarisation angle. The 408 nm free-running diode was placed in external cavity to force it to run single mode. The 780 nm diode was a bought-in system already in an external cavity. The violet diode laser was beam shaped using cylindrical lenses, with focal lengths of 25 mm and 50 mm. The two diode system beams were overlapped with a dichroic beam splitter ($R < 530nm < T$) and aligned through two pinholes, to ensure good beam overlap.

A $3\times3\times8$ mm^3 BBO crystal, supplied by Photox optical systems Ltd., was cut at $\theta = 44.2^{\circ}$ and $\phi = 0^{\circ}$ for phase-matching, using a sum frequency generation process. The front surface had been AR-coated at 410 nm and 780 nm, and the back facet high-transmission coated at 270 nm to maximise beam throughput. Manipulating the crystal angle and rotation allowed the UV produced in the system to be maximised. The alignment angle and rotation of the crystal was critical. Two 50 mm lenses were then placed with the BBO crystal in the system. A 50 mm uncoated lens was used to couple the beam into the crystal and a quartz lens AR-coated for the blue and UV was used to optimise UV transmission, re-collimating the beam.

The crystal was mounted on a stage to allow rotation through 360° and fine adjustment in the horizontal and vertical directions. It was then placed in the lens relay such that the back reflections of the fundamental beams from the crystal could be seen near the centre of the closed pinhole. This served as a crude alignment. The fine adjustors were used, and the beam reflections moved in a grid like fashion across the pinhole. This was also done for the crystal at 0° and 90° rotations to locate and maximise the UV. The optimum crystal orientation is dependent on the polarisation of the input beams. Only one orientation will satisfy the conditions required for sum frequency generation.

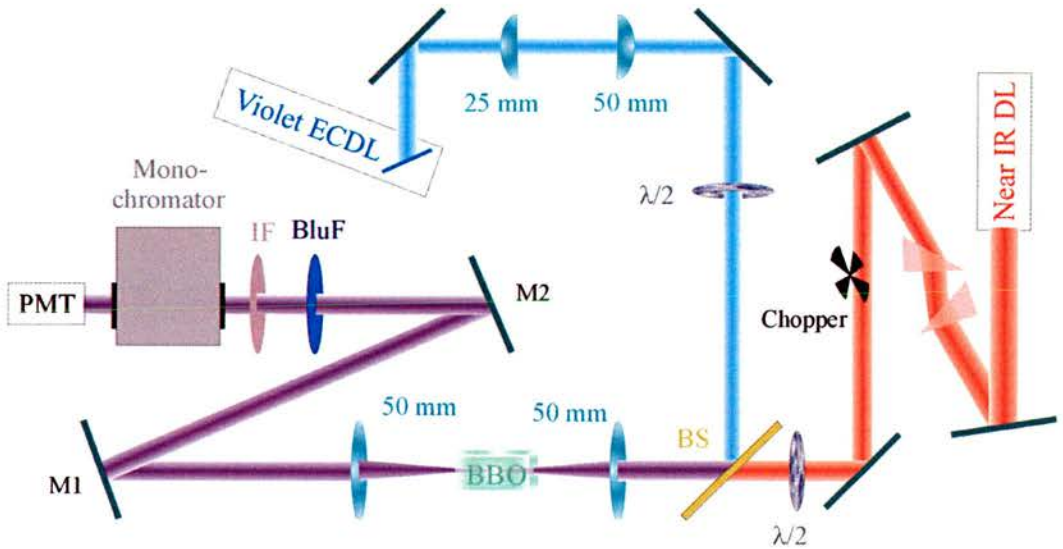

Figure 6.5. Light at 269 nm was generated using a near Infrared (near IR) diode laser and a violet diode laser in external cavity. The violet beam was beam shaped using two cylindrical lenses and the red using an anamorphic prism pair. Both beams are overlapped and coupled through a BBO crystal and directed onto a PMT.

Two UV mirrors (M1 and M2 in figure 6.5) were used for beam steering to adjust the UV height through the monochromator and onto the photo-multiplier tube, PMT (Hamamatsu Type H5784-06). The PMT was placed close to the monochromator exit to avoid scattered light, and filters were used to prevent the PMT saturation due to high sensitivity.

A power measurement can be inferred from the PMT voltage response with a conversion of 23 V/nW (figure 6.6). Since the PMT was sensitive to blue and UV light, and not red, a chopper was placed in the red beam to enable a simple and effective check, to maximise the generated light. Both red and UV signals were monitored. Any detected unchopped scattered light, caused from a background light source, contributed to a dc-offset, allowing it to be distinguished from the detected UV signal. 22.5 nW of UV light at 269 nm was generated through the crystal.

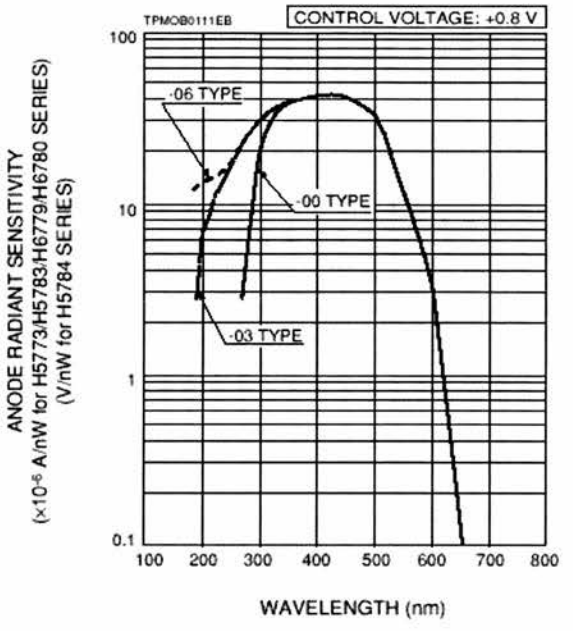

(a)

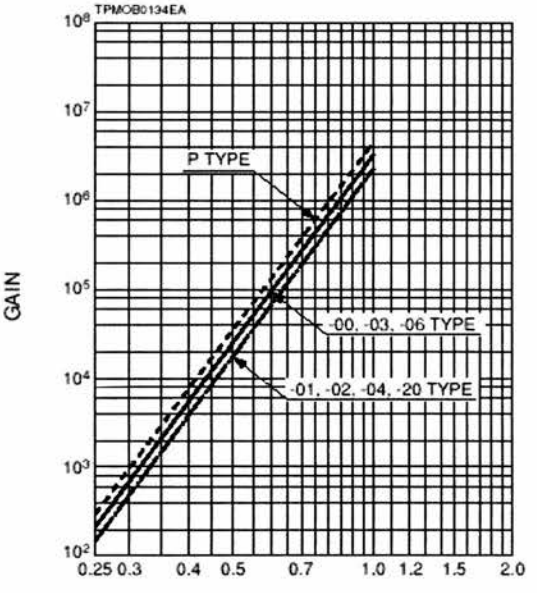

(b)

Figure 6.6. PMT (Type H5784-06) uses a control voltage of 0.8V to maximise detection of 254 nm light [19].

A power conversion efficiency of 2.04×10^{-5} % is obtained through comparison of fundamental input and sum frequency output powers. This is a relatively high efficiency compared to that found in the literature. The calculation method is discussed later.

6.7.2 Generation of 254 nm light

A microlensed diode laser with its free-running wavelength at 413 nm was obtained and wavelength matched with a microlensed diode laser at 662 nm, to allow the combined sum frequency generated light to reach the UV region. The external cavity violet diode laser was placed in the Littrow configuration with a holographic UV diffraction grating (2400 lines/mm) forcing the diode to 411 nm. This reduced the useable maximum output power of the diode from its free-running output power of 25 mW to 14 mW. This violet diode laser provided a 4 MHz linewidth with a continuous tuning range of 6 GHz, coarsely tunable over 2 nm. The 50 mW 662 nm diode had a current tuning range over 70 GHz with a linewidth of 11 MHz. The diode laser heads of both respective lasers were oriented to allow the major axis of the beams to be horizontal. In this orientation, both laser beams were linearly polarised in the vertical direction and therefore set to the same polarisation. Half-wave plates were used in each beam to optimise this polarisation.

The diode systems were combined with a dichroic beam splitter ($R < 530nm < T$), as shown in figure 6.7, and aligned through two pinholes to ensure good beam overlap. The red beam was aligned and kept at a constant height whilst the violet beam, due to the diode mount's tendency to relax out of external cavity, was corrected and re-aligned with the red beam. Two 50 mm lenses were then placed in the system. To minimise back reflections to the 662 nm diode laser the first lens was anti-reflection (AR) coated in the red. Initially this lens was uncoated to maximise violet and red wavelengths through the crystal. However, back reflections from the lens and crystal facet had a tendency to disturb the red diode. This was therefore replaced with an AR-coated lens. The free-running red microlensed laser was extremely susceptible to feedback and this solution did not eradicate the problem, but provided a significant improvement. A quartz lens AR-coated for the violet and UV was used to optimise UV transmission out of the lens relay and re-collimate the beam.

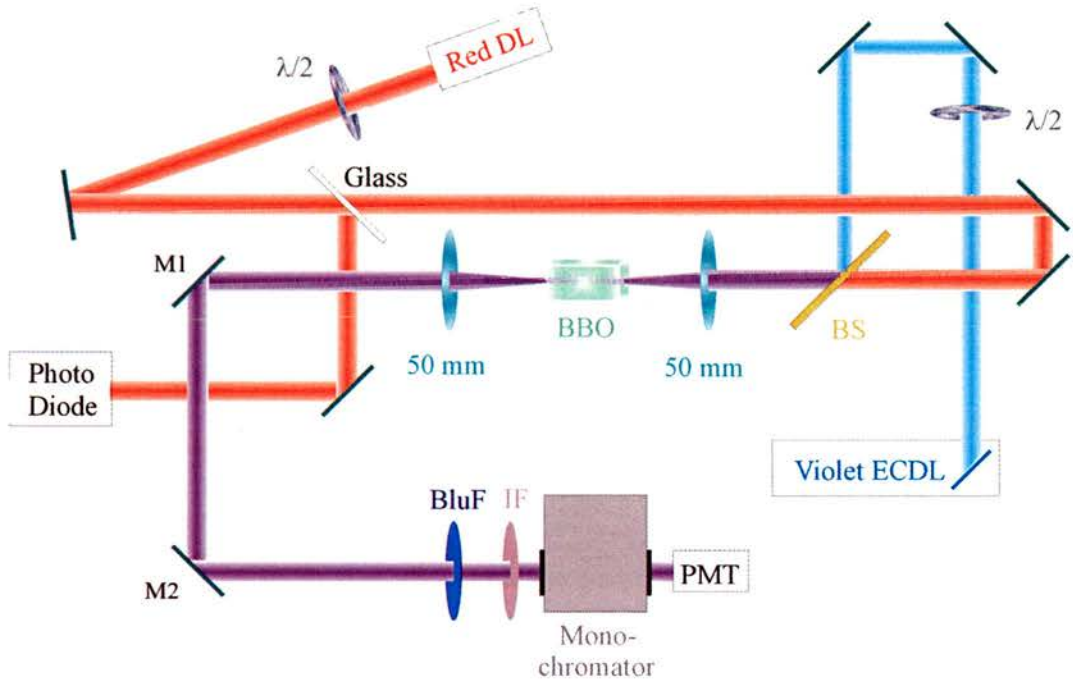

Figure 6.7. The experimental set-up for generating UV at 253.7 nm is shown. The violet external cavity microlensed diode laser is combined with the free-running red microlensed diode laser in a BBO crystal. The generated UV light is directed through a monochromator and onto a PMT.

A BBO crystal, supplied by Photox optical systems Ltd., was cut at $\theta = 49.3^{\circ}$ and $\phi = 0^{\circ}$ for phase-matching, with dimensions of $3\times3\times8$ mm^3. The front surface had been AR-coated at 410 nm and 665 nm, and the back facet high-transmission coated at 254 nm to maximise beam throughput. The two beams were combined and aligned through the crystal to generate UV in a similar manner to the 269 nm case previously discussed. Two UV mirrors (M1 and M2 in figure 6.7) were used as beam steers to adjust the UV height through the monochromator and onto the photo-multiplier tube (PMT). The PMT was placed close to the monochromator exit to avoid scattered light. An interference filter (IF) and blue filter (BluF) were used at its entrance to prevent the PMT saturating due to its high sensitivity. The UV power, generated at the crystal, suffered huge loss through the optical system. The UV coated lens was 99 % transmissive (0.99T), two UV mirrors each 0.98T, interference filter 0.4T, blue filter 0.33T and monochromator 0.6T.

	Red beam		Violet beam	
Equal parameters	Re-sizing ratio	Lens system (mm)	Re-sizing ratio	Lens system (mm)
b = 8 mm	1.31	100 + 80	0.86	40 + 50
b = 32 mm	1.81	100 + 50 80 + 50	1.23	50 + 40
w_o = 20 μm	1.16	None	0.98	None
w_o = 40 μm	2.32	100 + 50 160 + 63	1.96	100 + 50

Table 6.1. Lens design systems showing ratio used to reduce beam diameter and the lens used to resize the beams. Beam parameters are shown for equal confocal parameters b, and beam waists w_o.

Initially, both fundamental beams were used without a lens relay; the beam waists were therefore 17.2 μm and 20.4 μm for violet and red diodes, respectively. This provided a UV output power of 6.5 nW with a theoretical output power of 85.0 nW. This calculation is discussed in the next section. It was therefore decided to design a lens system to optimise beam overlap, producing higher sum frequency conversion efficiency. A Mathcad model was used to design different lens relays to manipulate beam parameters, shown in table 6.1. The emergent red and violet diode beams were 3.2 mm and 1.7 mm in diameter respectively. Beam re-sizing ratios express the amount each beam needs to be reduced by, in an ideal case. Lens systems were realised experimentally using the best fitting telescope with the lenses available.

The UV power at the PMT was detected, with an interference filter and two blue filters, in the presence of a chopper. The chopper was estimated to exclude 80 % of the incident light, through calculation of its area. Figure 6.8 shows the UV power being directly proportional to the fundamental red beam. Here the fundamental beams have been manipulated such that confocal parameters matched the length of the crystal (using a lens relay system that was later improved to generate greater UV power). The higher plotted

points correspond to saturation of the PMT. After compensating for the system losses, the UV power was calculated to be 22.1 nW of UV light generated through the crystal.

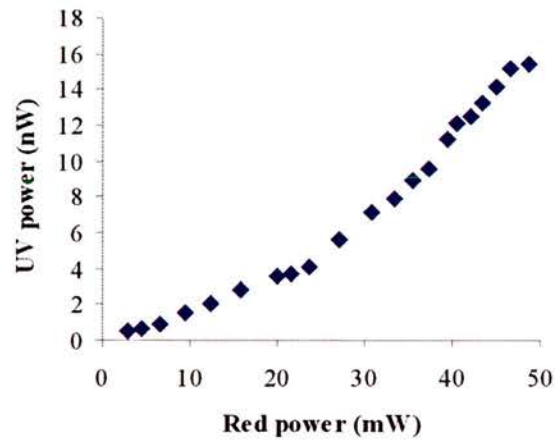

Figure 6.8. The generated UV power shows a linear dependence on the fundamental red diode laser power.

A more direct measurement was also taken, placing a Newport power meter after the monochromator and two UV mirrors. The power meter, although a more direct measurement, does not have the response speed of the PMT, and can therefore not be reliably used to maximise the generated light in this system. A glass slide, used to direct a fraction of light onto a photodiode, also allowed differentiation between UV light and any background noise (the cut off wavelength of glass being 300 nm). The typical noise on the PMT signal was between 0.1 and 0.4 of the UV detected signal depending on oscilloscope settings and optical filters in place.

6.7.3 Optimising beam overlap and power efficiency

High power efficiency demands good beam overlap. Confocal parameter and beam waist sizes must therefore be manipulated. A Mathcad model was used as a method to determine beam overlap, comparing the difference in beam areas, figure 6.9.

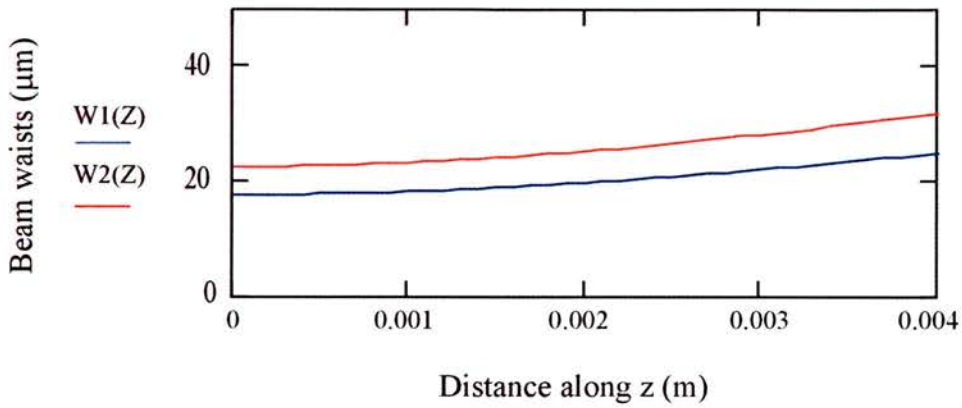

Figure 6.9. Graph of beam overlap is shown for equal confocal parameters (b = 8 mm) of both beams. The area overlap of the two beam profiles is 78.2 %, where w1 represents the violet fundamental beam (of beam waist 17.6 μm) and w2 the red (of beam waist 22.5 μm).

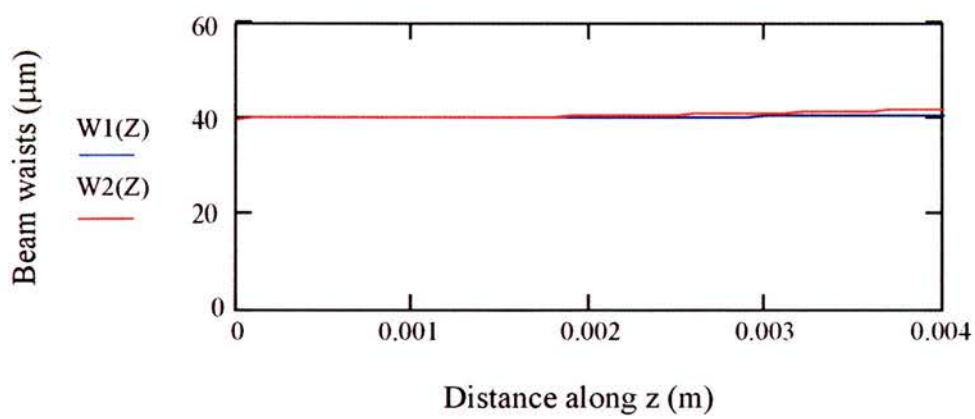

Figure 6.10. Graph shows beam overlap when both beam waists equal 40 μm. The area overlap of the two beam profiles is 96.4 %, where *w1* represents the violet and *w2* the red fundamental beam.

The beams of radius w_1 and w_2 for violet and red beams, respectively, diverge from a specified waist along a distance of 4 mm, assuming the focal plane is central to the crystal (of length 8 mm). Figure 6.9 shows results for the case discussed above, where both beam confocal parameters equal the crystal length. The case where both beams focus to a waist of 40 μm is shown in figure 6.10.

It can clearly be seen by eye using the model results shown in figures 6.9 and 6.10, and numerically through a simple area calculation, that the case where both beams have the same waist size has by far the best overlap. Table 6.2 shows the different values used in experiment for beam waist and confocal parameters. The beam overlap, shown in table 6.2, describes the difference in the fundamental beam areas diverging from their beam waists. Figures 6.9 and 6.10 visually demonstrate the significant difference in both violet and red diode laser beams with equal confocal parameters and beam waists. Table 6.2 shows that best overlap occurs when both beams have a large waist and are of equal size.

Violet diode laser		**Red diode laser**		**Beam area overlap**	
Beam waist w_1 (μm)	b (mm)	Beam waist w_2 (μm)	b (mm)	Beam overlap (%)	Crystal overlap (%)
17.2	8	20.4	7	77.5	0.868
17.6	8	22.5	8	78.2	0.867
35.2	32	45.0	32	78.2	1.220
20	10	20	6	77.9	0.877
30	23	30	14	90.8	1.074
40	41	40	25	96.4	1.366
50	65	50	40	98.4	1.684

Table 6.2. The beam parameters of the red and violet beams are given with the theoretical area difference in overlap of the two beams and the beam-crystal overlap.

However, a large beam waist focussed into the crystal reduces the intensity. This can also negatively affect UV generation. A trade-off is therefore required here, between intensity at focus and good beam overlap.

For comparison, experimentally, both fundamental beam waists were matched to 20 μm and 40 μm, and with matched confocal parameters of 32 mm and 8 mm. The correct lens relay system was found to be crucial for telescoping fundamental beams to optimise UV output power. For beam waists of 40 μm, a UV power of 24.6 nW was generated.

Improvement to the lens relay system, through a more appropriate lens choice, allowed 43.6 nW of UV light and subsequently 50.3 nW to be obtained.

The theoretical power generated through the crystal was obtained from equation 6.9, for which the effective non-linear coefficient d_{eff}, was calculated using a Mathcad model to be 1.56 pm/V [20]. The focussing factor $h(B,\xi)$, was determined using figure 6.4 dependent on walk off parameter B, and focussing parameter ξ. B was calculated to be 17.5 (equation 6.14) using a crystal walk off angle of 86 mrad. A numerical value of ξ (equation 6.15) was evaluated for each set of experimental beam parameters, due to its dependence on the effective confocal parameter b_{eff} (equation 6.17). The theoretical sum frequency generation was evaluated for each set of beam parameters.

Equal parameters	Experimental power (nW)	Theoretical power (nW)	SFG Efficiency (%)
b = 8 mm	20.1	83.7	3.17×10^{-4}
b = 32 mm	26.1	41.8	1.58×10^{-4}
w_0 = 40 μm	50.3	64.7	2.45×10^{-4}

Table 6.3. Theoretical and experimental power values are shown for a range of beam parameters with the sum frequency generation power efficiencies.

Poor sum frequency generation conversion efficiency between theoretical and experimental UV power (table 6.3) is most likely due to a combination of poor or imperfect phase-matching, beam overlap, crystal quality, crystal cut or crystal losses. The findings shown here are, however, comparable with that in the literature. For example, Alnis et al. [3] and Franzke [1] have experimentally produced up to half their expected theoretical power. The efficiency η, described by equation 6.12, is shown for the different beam parameters used in this study. These are of the same magnitude as J. Sakuma et al. (~ 6.84×10^{-3} %) [8], and compare well elsewhere [6,21].

Author [Reference]	Generated wavelength (nm)	Power conversion (%)
Our data	254	7.9×10^{-5}
Alnis [3]	254	2.6×10^{-6}
Corner et al. [22]	309	2.3×10^{-6}
Hanna et al. [23]	227	32.0×10^{-6}
Franzke [1]	365	31.3×10^{-6}

Table 6.4. The experimental wavelength obtained here is shown with published data from other research groups, for comparison the output/input power conversion is also given.

A more simplistic determination of efficiency is a direct comparison of experimental values, which can be compared to other published efficiencies for sum frequency mixing in a single pass geometry. This method of power comparison is a useful way to avoid the different methods to calculate theoretical power used between author publications. A comparison of published data on generating ultraviolet wavelengths is considered in table 6.4 where power conversion R, (equation 6.18) is a percentage obtained through the direct ratio of the generated output power P_{UV}, with the fundamental input powers, P_{red} and P_{violet}.

$$R = \frac{P_{UV}}{P_{red} + P_{violet}} \times 100 \qquad [6.18]$$

This is a favourable comparison showing the relatively large UV power generated here, at least twice the power generated by similar experiments. However, greater output power has been achieved through the inclusion of an enhanced cavity to either the non-linear crystal or the individual fundamental beams. For example, Berkeland et al. [6] show a power conversion of 0.031 % and Hemmati et al. [7] 0.816 %, both producing light at 194 nm.

6.8 Conclusion and discussion

Sum frequency mixing has been demonstrated in a single pass geometry with diode lasers, to access the UV region of the spectrum. Light at 269 nm has been produced using two readily available standard diode lasers at 408 nm and 780 nm, producing 22 nW of UV light. Two microlensed diodes at 413 nm and 662 nm were also used to produce 50.3 nW of UV light through the manipulation of beam parameters. The 662 nm microlensed diode laser was used in a free-running geometry with the 413 nm diode in external cavity. Achieving good beam overlap matching fundamental beam waists rather than confocal parameters allows a relatively high efficiency of 2.45×10^{-4} % to be obtained. In addition, significantly higher power conversion efficiencies were obtained over those seen in the literature.

The red and violet microlensed diode lasers have proved useful and efficient devices used to reach ultraviolet wavelengths. Their beam quality permits good beam overlap within the non-linear crystal from compact sources. Generating UV light in this way has produced a source that can be employed with wavelength modulation techniques for detailed spectroscopy, as discussed by Alnis [3]. Improvement to the generated output power of this system could also potentially be achieved through coupling to an enhancement cavity allowing a multi-pass system [25]. Such systems have also previously been shown by Kumagai et al. [26] utilising a Ti:Sapphire laser and a diode laser for laser cooling of silicon atoms. They show a multipass system achieving 50 mW of UV at 252.4 nm, estimated to be 59 μW on single pass. The flexibility of this UV generation system allows such wavelengths to be generated, although powers of this magnitude may be difficult to reach in a single pass system. For practical laser cooling applications, powers of more than 10 mW are required.

6.9 References

[1] J. Franzke, "Sum frequency generation at 365 nm by two diode lasers applied to the detection of mercury", Spectro. Acta Part B, Technical note 1595 (1998)

[2] J. Franzke et al., "Tunable UV generation at 283 nm by frequency doubling and sum frequency mixing of two semiconductor lasers for the detection of Pb", Spectro. Acta Part B **53** 1951 (1998)

[3] J. Alnis et al., "Sum-frequency with a blue diode laser for mercury spectroscopy at 254 nm", Appl. Phys. Lett. **76** 1234 (2000)

[4] C. E. Wagstaff and M. H. Dunn, "Saturated absorption spectroscopy in the ultra-violet with a continuous-wave, frequency-doubled, ring dye laser; Even isotope shifts on the $6d_3D_1$-$6p^3P_0$ transition of HgI", Opt. Comm. **35** 353 (1980)

[5] C. H. Kwon et al., "Development of a coherent vacuum ultraviolet source at 104-108 nm generated by four-wave sum frequency mixing in Hg vapour", Rev. Sci. Instrum. **74** 2939 (2003)

[6] D. J. Berkeland et al., "Sum-frequency generation of continuous-wave light at 194 nm", Appl. Opt. **36** 4159 (1997)

[7] H. Hemmati et al., "Generation of continuous-wave 194-nm radiation by sum-frequency mixing in an external ring cavity", Opt. Lett. **8** 73 (1983)

[8] J. Sakuma et al., "Generation of all-solid-state, high-power continuous-wave 213-nm light based on sum-frequency mixing in $CsLiB_6O_{10}$", Opt. Lett. **29** 1096 (2004)

[9] K. Sugiyama et al., "Generation of continuous-wave ultraviolet light by sum-frequency mixing of diode-laser and argon-ion-laser radiation in β-BaB_2O_4", Opt. Lett. **16** 449 (1991)

[10] P. N. Butcher and D. Cotter, "The elements of nonlinear optics", Cambridge university press (1990)

[11] A. Yariv, "Optical electronics", Fourth edition, Saunders College Publishing (1991)
[12] M. Ebrahimzadeh, Nonlinear optics II, Lecture course notes, University of St Andrews (2001)

[13] http://www.cohr.com/downloads/BBO_DS.pdf, Coherent, "BBO: Beta Barium Borate β-BaB_2O_4"

[14] G. D. Boyd and D. A. Kleinman, "Parameteric interaction of focussed Gaussian light beams", J. Appl. Phys. **39** 3597 (1968)
[15] A. E. Seigman, "Lasers", University science books, California (1986)

[16] S. Guha, F. J. Wu and J. Falk, "The effects of focussing on parametric oscillation", IEEE J. Q. Electron. **QE18** 907 (1982)

[17] B. Ruffling et al., "High-power picosecond LiB3O5 optical parameteric oscillators tunable in the blue spectral range", Appl. Phys. B **72** 137 (2001)

[19] Hamamatsu, "Photosensor modules 5784 series", www.hamamatsu.com

[20] D. N. Nikogosyan, "Properties of optical and laser-related materials: A handbook", Wiley (1997)

[21] H. Kumgai et al., "Efficient sum-frequency generation of continuous-wave single-frequency coherent light at 252 nm with dual wavelength enhancement", Opt. Lett. **28** 1969 (2003)

[22] L. Corner et al., "Sum frequency generation at 309 nm using a violet and a near-IR DFB diode laser for detection of OH", Appl. Phys. B **74** 441 (2002)

[23] S. F. Hanna et al., "Diode-laser-based ultraviolet absorption sensor for nitric oxide", Appl. Phys. B, published online (2002)

[24] F. B. Dunning and R. E. Stickel Jr., "Sum frequency mixing in potassium pentaborate as a source of tunable coherent radiation at wavelengths below 217 nm", Appl. Opt. **15** 3131 (1976)

[25] I. Courtillot et al., "Efficient cooling and trapping of strontium atoms", Opt. Lett. **28** 468 (2003)

[26] H. Kumagai et al., " High-power deep-UV cw coherent light source for laser cooling of silicon atoms", RIKEN review: Focussed on coherent science **33** 3 (2001)

[27] I. D. Lindsay, "High spatial and spectral quality diode-laser-based pump sources for solid-state lasers and optical parametric oscillators", Ph.D. thesis, University of St Andrews (1999)

Chapter 7

Absorption spectroscopy of mercury with UV light

7.1 Introduction

Historically, mercury is an extensively studied element in the field of spectroscopy and atomic physics. This element provides many spectral features of interest, most notably the atomic absorption line at 253.7 nm. The spectral line in natural mercury vapour combines isotope transitions with hyperfine structure, making it one of the most interesting and influential spectral features of study. Traditionally, the mercury intercombination line is one of the most extensively studied spectral lines, providing a distinct fingerprint for the detection of mercury. Wood in 1912 [1] pioneered isolation of atomic spectral lines through studying the mercury resonance line 253.7 nm from atomic vapour. Following these observations, experimental understanding of this intercombination line is historically closely linked with progression of early atomic theory.

The ultraviolet (UV) spectral region is a notoriously difficult wavelength region to reach. Previous studies have involved large powerful Ti:Sapphire or dye lasers, employing frequency doubling of the emission light, to access the shorter UV wavelengths. However, more recently, spectroscopic work has incorporated the more compact,

inexpensive diode lasers as spectroscopic sources. These allow access to the UV region through sum frequency and second harmonic generation [2,3]. However, the relatively low tuning capabilities of diode lasers [3,4] have, in the past, limited their use.

A large mode-hop-free tuning range is required to observe the 253.7 nm absorption line in its entirety. Recent work employing these devices has relied on combining more than one spectrally adjacent scan over 80 GHz, to observe the total spectroscopic absorption signal. Alnis et al. [4] were able to generate 0.9 nW of UV light using sum frequency mixing in a single pass geometry with a 5 mW 404 nm extended cavity diode laser with a 30 mW single mode 688 nm diode laser. Three overlapping scans were combined to observe the entire spectral line. Jacobs et al. [2] produced 150 μW of 254 nm light in an enhanced system, by frequency quadrupling a 1016 nm semiconductor laser in a two-stage process, providing a scan width of 40 GHz.

This chapter shows the intercombination line of mercury at 253.7 nm in a single scan of 70 GHz using two microlensed diode lasers, previously discussed in chapter 4. Chapter 6 describes an experimental set-up providing access to the UV spectral region to allow detection of this mercury line. This experiment was the last carried out in a small laboratory affectionately known as the broom cupboard, before refurbishment to the department basement got underway. It is somehow poignant to note that the first experiment in this laboratory, almost 25 years previously, was also spectroscopy of mercury, using a frequency doubled Rhodamine 6G dye laser to reach the 296.7 nm transition line [5].

7.2 Absorption spectroscopy

The 253.7 nm mercury spectral line is a direct excitation from the ground state, to an excited state between $6^1S_0 - 6^3P_1$. Figure 7.1 shows this energy transition in a Grotian diagram. An atom can absorb light if it interacts with photons of a particular energy. For this to occur, the photon must have an energy near to the corresponding atomic energy level transition.

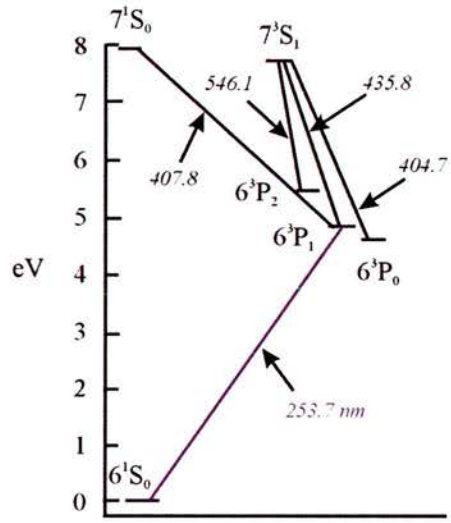

Figure 7.1. An energy diagram of mercury is shown. The 253.7 nm transition between the ground state 6^1S_0 and an excited state 6^3P_0 [6] can be seen.

In this study, the resonance line of mercury vapour is observed at 253.7 nm through a quartz cell. Absorption spectroscopy is commonly carried out using a hollow cathode lamp or a flame [7,8]. Here we use a metal vapour cell. Directly exciting from a ground state simplifies the optical experiment, negating the need for optical excitation to gain access to the required line by sources such as a discharge lamp.

7.3 Isotope and hyperfine transitions

Each atom has preferred combinations of neutrons and protons within the nucleus, where the forces holding the nuclei together balance. This puts a limit on the stable isotopes found in nature for a particular element. Mercury has seven naturally occurring isotopes, Hg^{196}, Hg^{198}, Hg^{199}, Hg^{200}, Hg^{201}, Hg^{202} and Hg^{204}, of varying abundance. In this natural composition, only Hg^{196} is an unstable radioactive isotope ordinarily appearing in trace concentrations [9].

The five even isotopes create individual isotopic shifts in the spectral line, due to the motion of the nucleus, exhibiting distinguishable features in the absorption line. The nuclei of even isotopes contain an even number of protons and neutrons; the nucleus will

therefore have an integer spin, and can be expected to have a nuclear spin of zero [10, 11]. This indicates a single transition line will occur for these nuclides. In addition, the two odd isotopes produce a shift due to hyperfine splitting. Hyperfine transitions are a fine structure formed from the splitting of the energy levels of an atom. The nucleus possesses an angular momentum, also known as nuclear spin I, which varies according to how heavy the nuclear mass is (neutron plus proton number). The hyperfine splitting is caused by the interaction of the associated nuclear spin with the angular momentum of orbiting electrons, electron spin [11]. This nuclear-electron spin interaction allows for slight variations in the fine structure creating a shift in the energy transition. The isotope and hyperfine transitions that the five even and two odd isotopes undergo can be seen in figure 7.2. The hyperfine quantum number is the sum of the nuclear and electron spin quantum numbers ($F = I + J$).

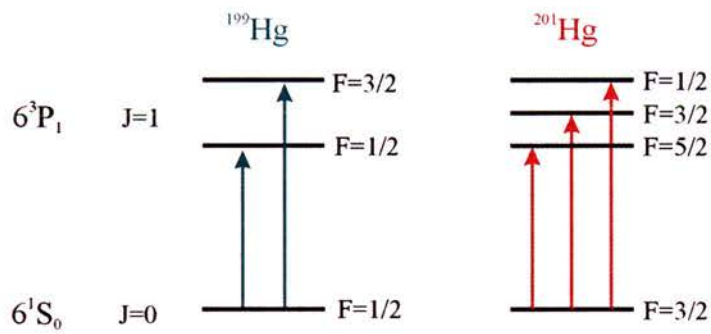

Figure 7.2. The hyperfine splitting of ^{199}Hg and ^{201}Hg isotopes are shown. The nuclear spin quantum number (I) for ^{199}Hg is 1/2 and for ^{201}Hg is 3/2. The hyperfine quantum number (F) is also shown.

The two odd isotopes Hg^{199} and Hg^{201} contribute a hyperfine structure to this absorption feature. Odd isotopes with an even number of protons and an odd number of neutrons produce hyperfine transitions due to a half-integer nuclear spin. For mercury, isotope Hg^{199} has a nuclear spin of $I = ½$ and isotope Hg^{201} a spin of $I = ⅜$ [12]. This splitting causes a shift in transition energies, which coincides with the Hg^{204} and Hg^{198} isotopic absorption features. The shifts of the respective mercury isotopic spectral features around 253.7 nm can be seen in figure 7.3. Both the isotope shifts and hyperfine energy transitions arise due to nucleic effects.

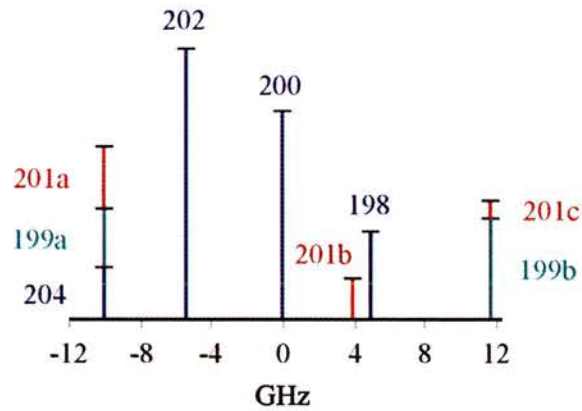

Figure 7.3. The naturally occurring mercury isotopes are shown making different peak contributions within the absorption line structure. The even isotopes making a single contribution compared to two ^{199}Hg and three ^{201}Hg hyperfine transitions.

7.4 Experimental spectroscopy of mercury

To reach the mercury line, light at 253.7 nm was produced using the sum frequency generation experiment described in chapter 6. The free-running 662 nm microlensed diode was used to exploit its large mode-hop-free tuning range and coupled to the 413 nm extended cavity microlensed diode laser for wavelength flexibility. In order to detect the absorption line, the previous set-up needed to be adapted to that shown in figure 7.4.

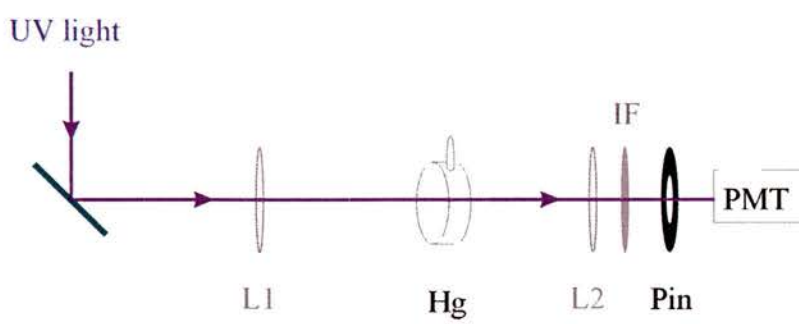

Figure 7.4. The experimental set-up for obtaining 253.7 nm UV light (figure 6.7) was altered to incorporate a mercury vapour cell to allow absorption spectroscopy.

A lens relay imaging system was placed after the final UV mirror. A 100 mm quartz lens, AR-coated for the blue and UV, focussed the generated beam and allowed it to expand up

to collect in a 32 mm quartz lens. The two lenses, of focal lengths L_1 and L_2, were placed between a distance of $L_1 + L_2$ and $L_1 + 2L_2$ apart. UV light was detected by carefully moving the second lens between these distances to control the focal plane of the UV, imaging light onto the photo-multiplier tube, PMT. A pinhole was placed at the UV focus and an interference filter placed immediately before the PMT. The pinhole acted to minimise background noise, and the filter prevented excess violet light saturating the detector. Two blue filters were also placed before the pinhole, used when required to reduce violet light.

The mercury vapour cell was made from quartz due to this material's transparency at ultraviolet wavelengths (the window of transparency for BK7 glass only extends down to 300 nm). The 8 mm thick cylindrical cell had a diameter of 30 mm, with a finger in which the mercury vapour was distilled. This cell was obtained [Laser 2000 (Northants,UK)], specified to be filled with a natural isotope mixture of mercury at atmospheric pressure.

As an aside, the National Institute of Standards and technology quotes the mercury absorption transition line at 253.652 nm [13] and a majority of literature written on mercury absorption agrees with this [9,14,15] or simplifies to 253.7 nm [10,16]. Conflicting reports on the resonance line location meant time was spent scanning these unsuccessful wavelength regions. However, closer inspection of Edner et al. [17], quoting the spectral line to reside at ~39412 cm^{-1} which corresponds to a wavelength of 253.73 nm, eventually allowed the absorption peak to be located.

The diffraction grating angle of the violet diode was adjusted to coarsely tune the wavelength close to 411.3 nm. In addition, to allow a greater degree of freedom for wavelength matching, the violet diode was current and temperature finely tuned. The 662 nm diode was current scanned between (107.0 - 121.0) mA corresponding to a wide mode-hop-free scan. The temperature of the red diode laser was then finely tuned and stabilised to 21.7 ± 0.1 °C corresponding to a wavelength shift from (662.227 - 662.234) nm. Manipulating both lasers in this way allowed coarse tuning with the violet diode and

fine-tuning with the red diode, to match the mercury transition line. The 70 GHz mode-hop-free tuning range obtained from the red diode allowed the entire mercury transition line to be observed in one scan, figure 7.5. The absorption line has been normalised using the transmission of the system in the absence of the mercury cell and the level obtained blocking the beam with a piece of glass.

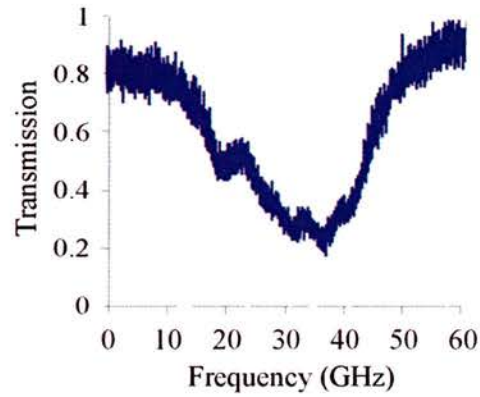

Figure 7.5. Mercury absorption signal from an atmospheric pressure cell with a natural isotope mixture, taken at room temperature.

The violet diode wavelength was fixed at a particular current and temperature and the red diode laser current tuned 63 GHz across the central frequency line shown in figure 7.5. Initially, the violet diode temperature was finely controlled with the red diode tuning over the same wavelength range. This allowed the central frequency to move from 253.719 nm in the first absorption picture, 253.716 nm in the second, and 253.715 in the third. With the violet diode set at the temperature used in the third scan, the red current scan was tuned using the diode temperature control. This allowed a scan centred on 253.714 nm, shown in the fourth scan. The fifth scan where the Hg absorption line appears central to the scan tunes around 253.713 nm. In each absorption peak profile a broadened absorption peak can be seen outlining the isotope and hyperfine structure. To observe the individual isotope and hyperfine transitions of the resonance line a different approach is needed.

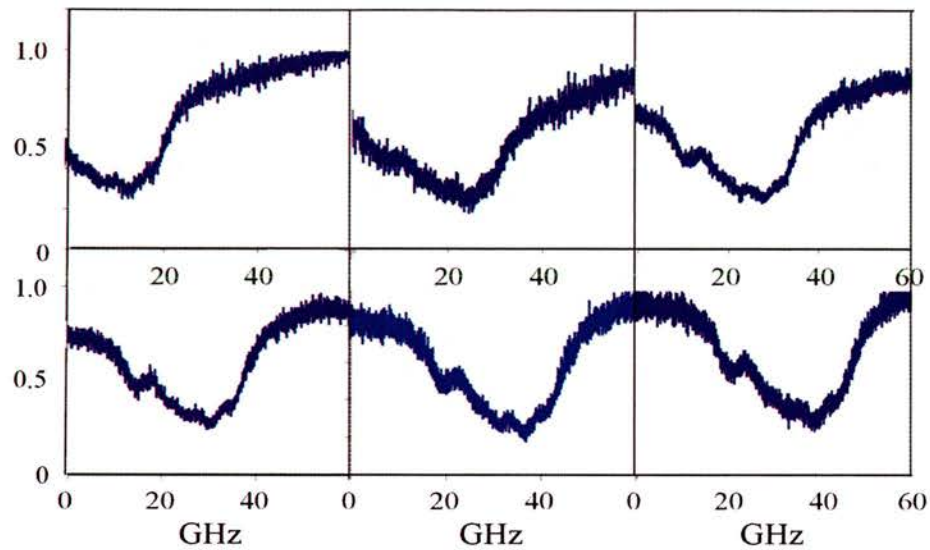

Figure 7.6. Series of mercury scans as the red diode is tuned across the central wavelength of 253.72 nm. The fifth scan shown corresponds to the central scan range of the absorption line, previously shown in figure 7.5.

The PMT was moved to obtain a fluorescence signal from the re-emission of light from the absorption of the incident UV by the mercury atoms. This experiment was set-up in a similar manner to that used in the detection of the absorption signal. The light was focussed through a lens to a PMT positioned above the vapour cell. As before, a pinhole was placed in the focal plane to reduce background light. No signal was detected, most probably due to the weak UV signal through the cell (6.5 nW). This was not investigated further due to a time constraint. However, the significant increase in UV light, obtained through the sum-frequency generation system, would be interesting to observe.

7.5 Pressure broadening

Interactions between atoms, whether from collisions or close encounters with neighbouring atoms, affect the atomic energy. Atomic interaction causes broadening to occur on the absorption peak, making the fine structure of the resonance line irresolvable. This broadening due to cell pressure makes it difficult to differentiate between individual hyperfine and isotope transition lines. The initial vapour cell discussed so far, having

been constructed at atmospheric pressure, shows such pressure broadening. This finding is in agreement with Alnis et al. [4] where two different cell types were used. The first cell, as with the atmospheric pressure cell used here, produced a broadened mercury absorption signal. The second cell, crucially, constructed at a lower pressure of an unknown quantity shows the nucleic fine structure within the absorption peak. This low pressure is key to the observation of fine structure in the intercombination line.

To reduce the effect of this absorption line broadening, a cell of low pressure is required. To achieve this it was initially decided to lower the temperature of the cell to subsequently affect the pressure inside the cell (Boyle's law).

7.6 Atmospheric pressure mercury cell

An aluminium mount to hold the cell was designed, figure 7.7. The upper section secured the cell while allowing light to transmit through.

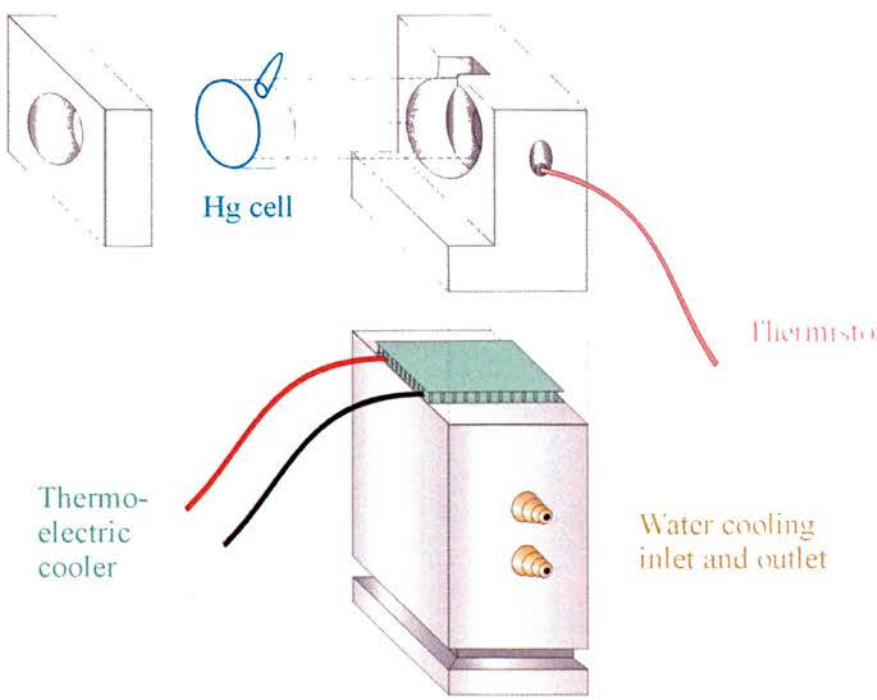

Figure 7.7. Aluminium mount for temperature controlling the Hg cell using both thermoelectric and water cooling.

A thermoelectric cooler (TEC) bridged the gap between upper and lower sections, the upper section allowing cooling to the cell while the lower section acted as a heat sink. The cell temperature was monitored with a thermistor placed close to the cell through the side of the mount. The thermoelectric cooler is capable of a 60 °C difference between its hot and cold sides. Therefore, water cooling was used to assist heat dissipation over the aluminium heat sink.

Two holes were drilled through the length of the base, then fitted with brass nozzles to allow water piper connections, two on either side. The first side was connected together with piping to provide a loop, whilst the other side provided a water pipe inlet and outlet. Silica sealant and rubber o-rings were used to ensure pipes were water tight (particularly important due to the fact that the BBO crystal generating UV light was hydrophobic). This combination of TEC and water cooling allowed the cell temperature to be lowered to approximately -10 °C. However, lowering the cell temperature in this way produced condensation, from the surrounding air, which formed on the cell windows. The temperature was therefore only reduced to 5 °C, producing a similar trace to those seen in figures 7.6.

To allow cooling below 5 °C, a Perspex box was designed with quartz windows to allow UV transmission, providing an isolation chamber for the mercury vapour cell, figure 7.8. The quartz windows were held in place with silicate, which also acted as a gas-tight seal. Two holes were drilled in the Perspex near the base. The first hole allowed a nitrogen flow to be introduced to the chamber with a rubber ring to ensure a gas-tight seal. The second hole allowed access for TEC wires and a thermistor, also serving as an escape route for air, as the container was filled with nitrogen gas. The lighter nitrogen gas flow was introduced into the chamber from a gas cylinder, forcing the heavier air mixture out through the escape holes at the base. This provided a nitrogen atmosphere sufficient enough to allow a reduction in temperature, without the risk of condensation forming. A central stage held the mercury mount stationary ensuring good alignment with the incident UV light. Side holes were drilled to allow water cooling access with gas-tight rubber seals.

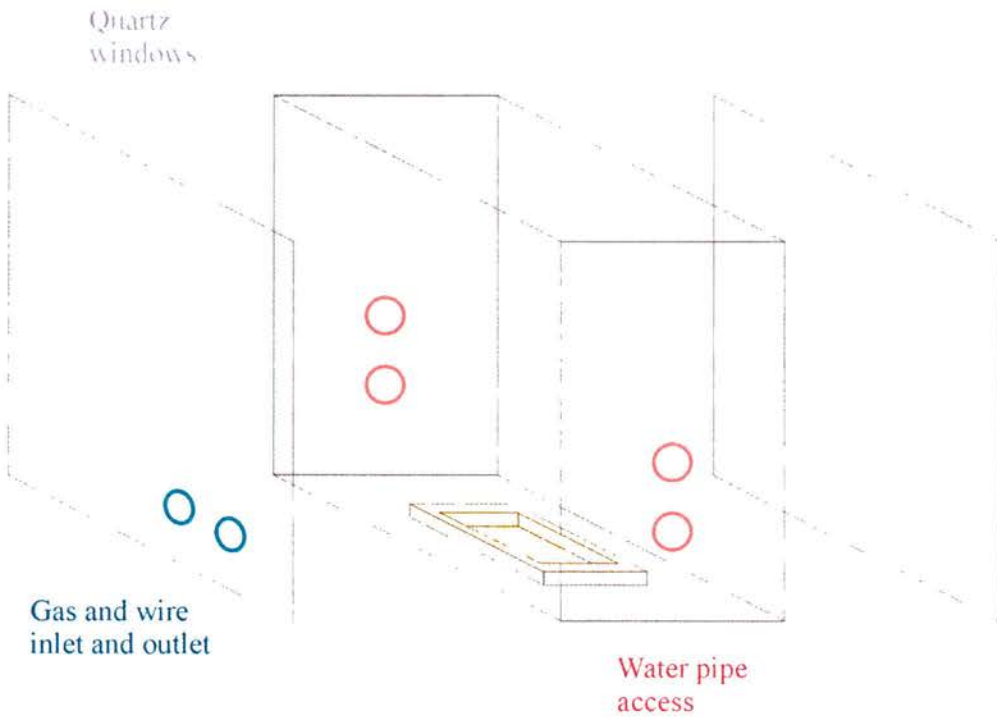

Figure 7.8. Perspex box with quartz windows (purple) to isolate Hg cell in a nitrogen atmosphere. Front escape holes allow an air escape route and access for TEC and thermistor wires (blue), side holes allow water pipe access (red). A central stand holds the Hg mount stationary (yellow).

The strength of the absorption signal was significantly weakened along with the expected higher resolution to the signal. It is possible that this was due to the fact that the Perspex chamber did not completely isolate the cell, thus condensation could still form on the vapour cell surface, resulting in the poor signal. To achieve a drop in pressure low enough to resolve finer features, the temperature would need to go much lower. Alnis et al. [4] allowed for a reduction in temperature to –20 °C. In this experimental design, this may reduce the signal to an undetectable level. The capabilities of the TEC controller did not allow for this, so this theory could not be checked. The cell configuration was therefore abandoned.

Liquid nitrogen was briefly tested allowing cooling to the cell through the finger. This predictably created a large amount of condensation on the cell windows, no absorption signal could therefore be seen. Due to time restrictions before lab refurbishment, a

suitable container to compensate for this was not constructed. The experiment was moved to a new location to allow further investigation. It was deemed simpler to construct a cell of lower vapour pressure, to obtain fine structure of the intercombination line.

7.7 Low pressure mercury cell

Fritz Akerboom, the retired departmental glassblower, assisted with the construction of a low pressure cell of similar dimensions, using an existing mercury vapour cell. The cell was evacuated and mercury vapour distilled into the quartz cell using liquid nitrogen for cooling, providing low pressure of unknown magnitude [18].

At this stage of research the experiment was handed over to a continuing PhD student and although assisting with its detection I was sadly not present when the fine structure scan was produced. Figure 7.9 shows the fine structure of the 253.7 nm resonance line eventually found. The isotope and hyperfine transitions of the intercombination line can clearly be seen, shown here with the previous atmospheric pressure scan illustrating how the fine structure aligns with the pressure broadened scan.

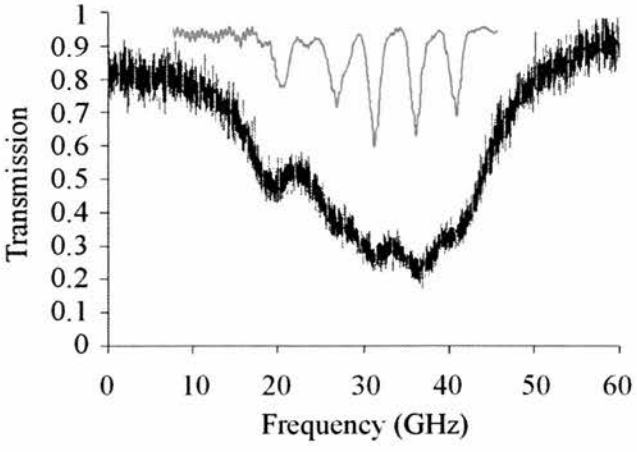

Figure 7.9. The broadened atmospheric scan of the mercury intercombination line is shown with a scan showing the fine structure of the mercury lines obtained with a low pressure cell (fine structure scan obtained by A. Shah).

7.8 Absorption spectroscopy of mercury

This research allowed investigation of the broad mercury intercombination line at 253.7 nm in a single scan. The generation of UV light was achieved by sum frequency generation of two microlensed diode lasers inside a BBO crystal. The 413 nm diode was used in external cavity for coarse tuning of the generated wavelength and the 662 nm diode as a free-running source. The large mode-hop-free tuning range of the red diode laser provided a scan of 70 GHz to observe the entire mercury resonance line in one scan. The narrow linewidth of these devices allow high-resolution spectroscopy to be performed. A cell at atmospheric pressure was used to obtain a pressure-broadened scan. Subsequently, a cell of a lower pressure, of unknown quantity, was used to enable the isotope and hyperfine structure of the intercombination transition to be observed.

This experiment allows spectroscopy of mercury detected in a single scan in a relatively compact system. The UV power level generated is sufficiently high to allow wavelength modulation on the Hg absorption line [19]. This could be achieved by applying a modulation over the red diode laser drive current as it is scanned over the relevant UV wavelength region. The advantage of this technique is the reduced noise in the detected signal, due to the lower 1/f noise at the higher modulation frequency. In addition, the direct absorption technique used here requires a comparison in detection signals on and off the resonance line. The application of such wavelength modulation signal would obviate the need for such a comparison. However, the detected signal would no longer be the traditional absorption signal as observed here.

It is also worth noting that a wealth of spectral absorption lines appear close to the generated 254 nm wavelength. These lines are potentially accessible through coarse tuning of the 413 nm violet diode laser grating. Examples of such spectral lines are Iridium (254.397 nm), Cobalt (253.596 nm) and Tungsten (255.135 nm), as recorded on the NIST website [13].

7.9 References

[1] R. W. Wood, "Selective reflexion, scattering and absorption by resonating gas molecules", Phil. Mag. **23** 689 (1912)

[2] J. P. Jacobs and R. B. Warrington, "Pressure shift and broadening of the 254-nm intercombination line of mercury by N_2", Phys. Rev. A, **68** 032722 (2003)

[3] T. Nishimura et al., "A compact 209-nm deep UV cw light source for spectroscopy using frequency doubling of a diode laser", Jpn. Appl. Phys., **42** 5079 (2003)

[4] J. Alnis et al., "Sum-frequency with a blue diode laser for mercury spectroscopy at 254 nm", Appl. Phys. Lett., **76** 1235 (2000)

[5] C. E. Wagsaff and M. H. Dunn, "Saturated absorption spectroscopy in the ultra-violet with a continuous-wave, frequency-doubled, ring dye laser; Even isotope shifts on the $6d_3D_1$-$6p^3P_0$ transition of HgI", Opt. Comm. **35** 353 (1980)

[6] Haken and Wolf, "The physics of atoms and quanta: Introduction to experiments and theory", Fifth edition, Springer (1996)

[7] H. Scheiber et al., "Laser absorption spectroscopy with a blue diode laser in an aluminium hollow cathode discharge", Rev. Sci. Instrum. **73** 378 (2002)

[8] R. L. Cavasso-Filho et al., "Laser spectroscopy of calcium in hollow-cathode discharges", J. Opt. Soc. Am. B **18** 1922 (2001)
[9] F. Bitter, "Magnetic resonance in radiating or absorbing atoms", Appl. Opt. **1** 1 (1962)

[10] F. Bitter et al., "Optical studies of radioactive mercury", Phys. Rev. **96** 1531 (1954)

[11] G. Herzberg, "Atomic spectra and atomic structure", New York Dover Publications (1945)

[12] Y. Nishimura and T. Fujimoto, "λ = 2537 Å line from a low-pressure mercury discharge lamp emission profile and line absorption by a gas containing a mercury vapour", Appl. Phys. B: Lasers and Opt. **38** 91 (1985)

[13] http://physics.nist.gov/cgi-bin/ASD/lines1.pl

[14] M. Sjoholm et al., "Atomic mercury flux monitoring using an optical parametric oscillator based lidar system", Opt. Express **12** 551 (2004)

[15] e.g. P. Bisling et al., "Abundance ratios of mercury isotopes by 6s6p3P1-intermediate state excitation with resonance ionisation mass spectrometry", Fresenius J.

Anal. Chem. **364** 79 (1999); A. R. Thomas, "Absorption of resonance radiation in mercury vapour", Phys. Rev. **35** 1253 (1930);

[16] e.g. P. H. Garrett, "Mean lives of mercury lines λ2537 and λ849", Phys. Rev. **40** 779 (1932); S. Hattori et al., "Stabilized monochromatic radiation source using the mercury resonance line (2537Å)", J. Phys. D: Appl. Phys. **3** 607 (1970)

[17] H. Edner et al., "Differential optical absorption spectroscopy system used for atmospheric mercury monitoring", Appl. Opt. **25** 403 (1986)

[18] K. G. Libbrecht et al., "Teaching physics with 670 nm diode lasers- construction of stabilized lasers and lithium cells", Am. J. Phys. **63** 729 (1995)

[19] K. Song and E. C. Jung, "Recent developments in modulation spectroscopy for trace gas detection using tunable diode lasers", Appl. Spec. Rev. **38** 395 (2003)

Chapter 8

Conclusions and future work

In this thesis, two distinct but inter-related areas of study have been investigated. Firstly, the use of novel optical techniques was discussed to manipulate micron-sized particles and to perform biological spectroscopy. Secondly, non-linear sum frequency mixing of two microlensed diode lasers in the violet and red allowed the generation of ultraviolet light for spectroscopy on atomic mercury. Experiments were conducted using laser sources spanning the spectrum, ranging 410 nm to 1064 nm. Here, general conclusions to these experiments will be given with relevant future work.

The first section discussed optical tweezing techniques for the manipulation of microscopic particles. A detailed comparison between Gaussian and Bessel beams was given, for their use as an optical guide. A zeroth order Bessel beam was selected as suitable for comparison with a Gaussian beam due to its on-axis intensity. A theoretical model constructed by K. Sepulveda was based on a ray optics approach and compared the radial and transverse forces of two beams. In agreement with experiment, the model showed the localisation of particles within the Gaussian beam and central maximum of the Bessel beam. In addition, the respective beams axial intensity distribution was

modelled along the propagation direction. This theory was in agreement with experimental findings. A Gaussian beam was shown to provide fast delivery of particles occurring over a relatively short distance (~ 0.96 mm). Due to the Bessel beams "non-diffracting" central core, particles can be localised radially within the beam throughout its propagation distance. In contrast to the Gaussian guiding, the Bessel beam described here offers extended guiding distances of over 9 mm, ten times that of the Gaussian beam. However, experimentally this was limited to 3 mm due to the size of the cuvette. The Bessel beam guiding velocity is significantly reduced with respect to the Gaussian beam, due to the lower power available in the central maximum of the beam. The sphere velocities show a linear dependency with power for all sphere diameters for both Gaussian and Bessel beams. An important application for both beams is the guiding of cells and chromosome fragments for applications in tissue and bio-engineering, and lab-on-a-chip research. In such applications, the Bessel beam makes an ideal choice for the transportation of particles offering substantially longer guiding distances.

Optical binding has been realised through the use of two counter-propagating beams. Chains of multiple particles, equally spaced from each other, were created by the construction of particle arrays. The arrays formed through optically induced particle-particle interactions arranging the spheres in an ordered fashion. This coupling of trapped particles through the use of light presented here is a distinct and novel study. Through the investigation of excitation modes, it was found that arrays respond in unison to oscillate in a centre-of-mass and breathing mode motion. Due to the extreme over-damping present in the system, the appearance of such oscillations is of interest. In addition, the arrays were investigated experimentally and theoretically at infrared wavelengths (780 nm and 1064 nm) by changing beam and particle parameters. It was shown that the particle chains could be used to infer a natural trap frequency for each set of experimental parameters. This allowed particle-particle interaction energies to be obtained. It was also observed that more than one stable equilibrium trap position could be found for a particle array. This is the subject of further study here at St Andrews using a dual-fibre optic trap to provide the counter-propagating beams. A theoretical model designed by E. Wright was also developed to describe the array configurations of two and three particles

residing within such arrays, allowing comparison with experimental data. The model can also be used to determine equilibrium positions and to predict the particle separations for a given set of parameters. Here, the gradient and scattering forces are treated as two separately defined forces. However, as both forces contribute to the optical binding, they cannot strictly speaking, be separated. Due to the relatively low impact of uncertainties in experimental parameters, such as particle refractive index and beam waist size, the model provides a good prediction of the beam waist separation in good agreement with experimental results. However, for small particles (1.28 μm in diameter), where the wavelength and particle size are similar, no correlation was found. This limitation of the model is due to the initial paraxial approximations used. Further work by E. wright and here at St Andrews to refine the model is currently in progress. This includes quantifying the scattering and gradient forces into a single force measurement. Thus removing the ambiguity as to the size of the arbitrary scattering force, with respect to the gradient force. Further investigation into experimental parameters, for example particle refractive index and beam waist sizes, which are not known to great accuracy, can also improve model predictions. The use of Bessel beams is also of interest to create extended arrays of regularly spaced particles due to the propagation distance of such beams. This one-dimensional array can also be extended into two and three dimensions to create orthogonally placed traps, potentially providing an optical landscape of particle trapping sites. However, the theoretical modelling of such systems is non-trivial. This extension of optically bound matter into two-dimensional and three-dimensional arrays can potentially allow insight into crystallisation processes and the sorting of biological matter, for example. Opportunities also arise using this optical binding to study colloid and crystal behaviour. A more realistic study of such arrangements is possible when compared to optically unbound arrays such as those produced by holographic techniques.

The use of violet diode lasers for optical tweezers, to provide reduced trapping volumes, has been discussed. Optical tweezers are already well-established workhorse tools in biophotonics and in the creation of micromachines. The smaller trap volume obtained at these shorter wavelengths is of benefit allowing yet smaller particles to be confined. This is an important consideration for the study of inter-cellular processes and proteomics. The

use of violet diodes as a fluorescent excitation source of biological tags and dyes has also been shown. L. Patterson prepared the biological samples experimentally used and discussed in this thesis. The fluorescent dyes allow biological spectroscopy to be performed coupled with the ability to manipulate matter. In addition, the damage caused to biological matter by violet wavelengths can be exploited. For example, a small focussed spot can localise cell damage allowing the introduction of foreign protein into the cell environment.

Microlensed diode lasers are demonstrated here as viable instruments for high-resolution spectroscopy. These are a new generation of diode laser that incorporate a cylindrical lens, placed a few microns from the diode output facet. This lens acts to create a circularised diode source whilst obviating the need for lossy beam shaping optics. A newly available device with wavelength at 413 nm and 25 mW of output power was studied, along with a red device at 662 nm, emitting 50 mW of output power. Both diodes were characterised in free-running and extended cavity geometries. In a free-running geometry, both violet and red microlensed diode lasers run on a single longitudinal mode, due to weak feedback from the microlens. Additionally, a large continuous tuning range has been demonstrated, through current tuning of the red diode, of over 70 GHz. Both diodes were place in a Littrow-configured geometry for extended cavity operation, with a selection of diffraction gratings. The extended cavity reduced the linewidth of the diodes, an improvement of a factor of at least 2 for the red, and 5 for the violet. In addition, this configuration allowed wavelength selectivity by angle tuning of the grating. These microlensed diode lasers have the potential to replace larger laser sources and to provide a compact alternative for spectroscopic studies as well as atom guiding and trapping studies. Further comparative studies with these devices could include coupling the diode into a Littman configured extended cavity.

The new development of violet devices has enabled a compact non-linear system to be constructed, using violet and red microlensed diode lasers to produce ultraviolet sources. Sum frequency generation allows access to hard-to-reach wavelength regions, in this case an ultraviolet output of 253.7 nm is generated. The red diode laser was used in a free-

running geometry while the violet was used in extended cavity. The two devices were overlapped and then coupled into a non-linear crystal. To obtain a good beam overlap inside the crystal, both beam confocal parameters and beam waists were independently matched. It was found that greater sum frequency conversion efficiency was obtained by matching beam waists inside the non-linear crystal. An output of 50 nW of ultraviolet power was achieved by matching beam waists, a significant improvement over the 22 nW obtained through matching both beam confocal parameters to the length of the crystal. Further studies into a higher generation efficiency from this single non-linear crystal pass system could be done through further investigation into beam waist matching inside the crystal. However, this system could yield a significantly higher sum frequency generated output through coupling to an enhancement cavity, offering a multi-pass system.

The ultraviolet radiation, obtained by the sum-frequency mixing discussed above, allowed generation of 253.7 nm light with which to access the inter-combination line for spectroscopy on atomic mercury. The free-running tuning range of the red diode laser allowed 70 GHz of continuous mode-hop-free tuning to observe the entire absorption transition ($6^1S_0 - 6^3P_1$) in one scan. A broadened absorption peak was shown using an atmospheric pressure cell at room temperature. In addition, a low pressure mercury cell allowed the fine structure of the mercury absorption line to be distinguished. The current system power is sufficiently high enough to further this study and allow wavelength modulation techniques. These techniques can potentially reduce the noise in the system significantly, and make the absorption peaks more identifiable, thus allowing more detailed spectroscopy of the mercury line. Locking techniques incorporated into the system can also provide stabilisation of the diode lasers and providing greater control of the ultraviolet wavelength. This can be achieved through a current/ piezo-electric transducer locking technique of the violet diode laser in extended cavity. Thus allowing the ultraviolet to be locked to a hyperfine transition.